Earth Embedding Products for Geospatial Analysis: Foundations, Applications, and Open Challenges

Yongchuan Cui, Keli Shi, and Shunlin Liang, *Fellow, IEEE*

***Abstract*—Earth observation satellites generate petabytes of imagery each year, but extracting useful information remains constrained by limited labels, heterogeneous sensors, and the cost of processing large archives. Foundation models reduce part of this burden by learning transferable representations from multi-source observations. More recently, these representations have been precomputed over continental and global extents and released as embedding layers or datasets. Existing reviews primarily examine model architectures, pretraining, and transfer learning; released embedding products also require attention to spatial and temporal support, storage, access, versioning, and evaluation as fixed geospatial features. This survey reviews the development of Earth embeddings from foundation model pretraining and reusable encoders to global and near-global embedding products. We organize the literature around data and representation learning, model and product design, distribution and access, evaluation benchmarks, and downstream applications. Experimentally, we compare representative embeddings through their geometry, downstream performance, and sensitivity to dimension across discrete and continuous land-surface tasks. Finally, we summarize the technical and scientific challenges surrounding global embedding products and discuss priorities for their evaluation, maintenance, and future development.**

***Index Terms*—Earth observation, foundation models, global embeddings, self-supervised learning, remote sensing.**

I. Introduction

The volume of Earth observation (EO) data acquired each day has grown by orders of magnitude over the past decade. The Copernicus programme distributes large volumes of Sentinel data through open-access platforms [1]. The Landsat archive extends back to 1972, although its spatial resolution, spectral bands, and radiometric characteristics differ across missions. NASA's Harmonized Landsat–Sentinel-2 (HLS) product combines Landsat 8/9 observations from 2013 onward with Sentinel-2 observations from 2015 onward [2], [3]. These archives record changes in land surfaces, oceans, and the atmosphere across space and time, yet extracting useful information from them remains difficult. Supervised learning, still the dominant approach for analyzing satellite images, depends on curated label sets that are expensive to collect, geographically biased toward well-studied regions, and quickly outdated in a changing world [4]. The gap between the volume of raw imagery and the limited availability of labels has become a central bottleneck in geospatial artificial intelligence.

Yongchuan Cui and Shunlin Liang are with the Jockey Club STEM Laboratory of Quantitative Remote Sensing, Department of Geography, The University of Hong Kong, Hong Kong, China. Keli Shi is with the Aerospace Information Research Institute, Chinese Academy of Sciences, Beijing 100094, China.

Corresponding author: Shunlin Liang (e-mail: shunlin@hku.hk).

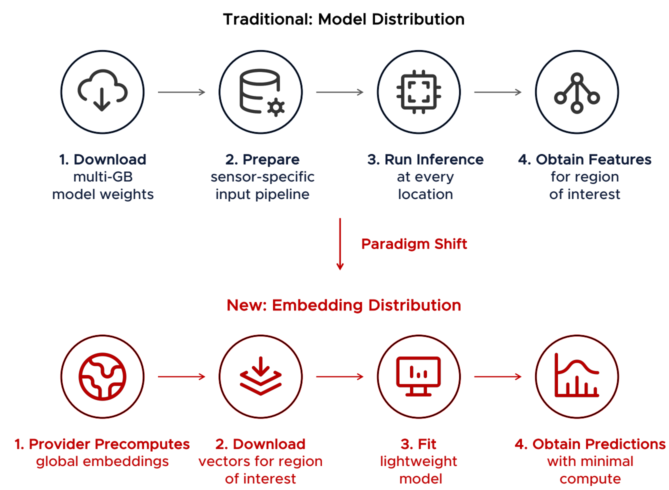

Fig. 1. Model-based and embedding-based approaches to geospatial analysis.

Pretraining without manual labels offers a way around this bottleneck. By designing pretext tasks that extract supervisory signals from the data itself, methods such as contrastive learning [5], [6], masked image modeling [7], and self-distillation [8], [9] have produced geospatial foundation models (GFMs), including image-based, location-based, and multimodal encoders pretrained on satellite and related Earth observation archives [10]–[13]. Most of these models, however, have been used primarily as backbones for downstream fine-tuning on tasks such as object detection, semantic segmentation, and land-cover classification, rather than released as directly reusable global representations. They have achieved state-of-the-art results on particular remote sensing tasks and benchmarks, but using them still requires downloading large model weights, preparing sensor-specific input pipelines, and running computationally intensive inference at every location of interest. Continental and global analysis therefore remains computationally expensive. During the past two years, products such as the Google Satellite Embedding dataset, generated with AlphaEarth Foundations, have begun to provide learned representations as precomputed, openly distributed geospatial data [14], [15].

A. From Models to Embeddings

Instead of distributing only model weights, recent work precomputes dense vector representations over large geographic extents and publishes them as geospatial layers. Downstream tasks can then use lightweight models, often linear regressors

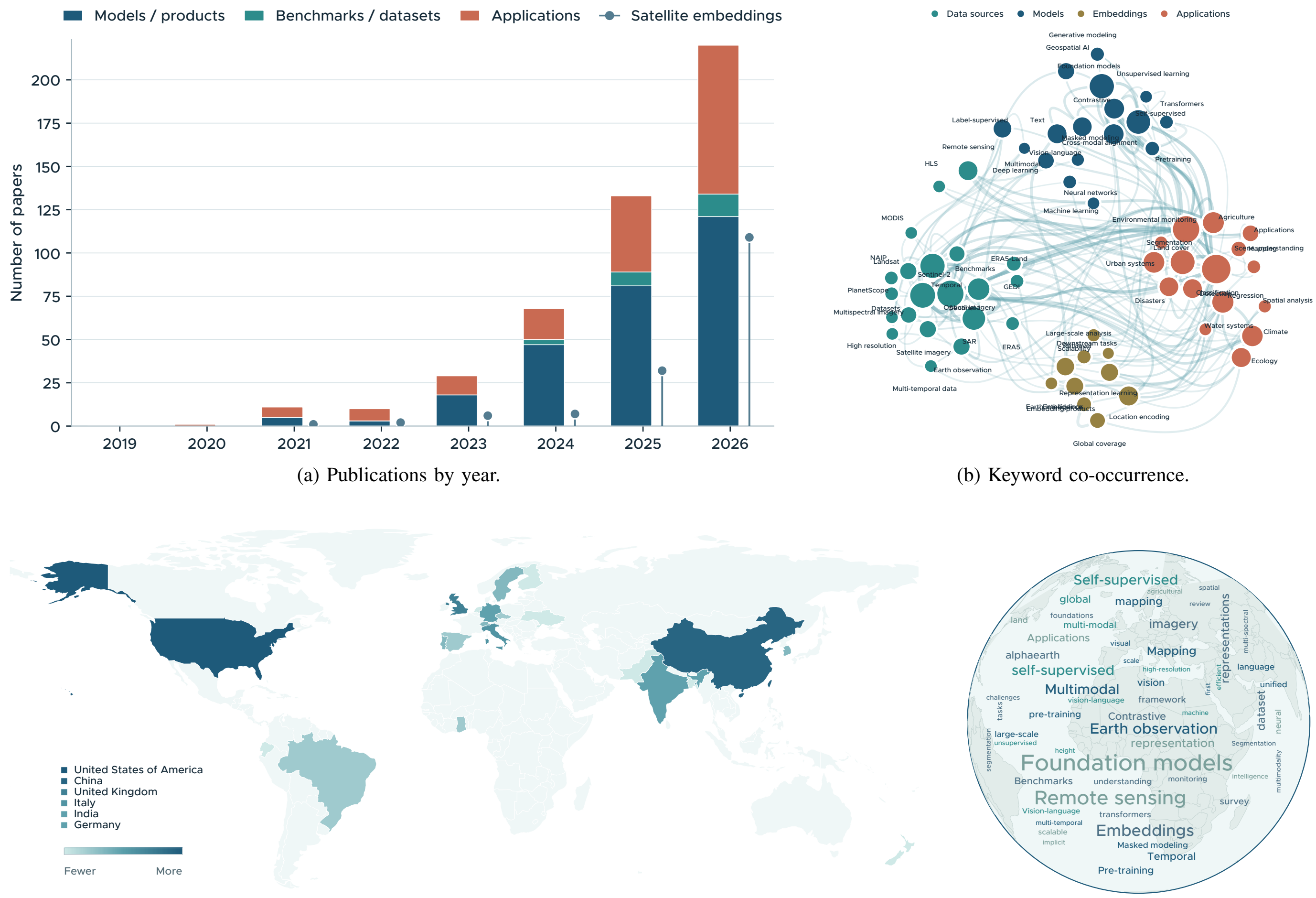

(a) Publications by year.

(b) Keyword co-occurrence.

(c) Affiliation distribution.

(d) Keyword cloud.

Fig. 2. Bibliometric overview of the literature considered in this survey.

or small classification heads, without repeating large-scale inference. MOSAIKS [16] computes random convolutional features from global Landsat imagery and uses the same features to predict forest cover, housing prices, and nighttime light intensity with accuracy competitive with deep neural networks. SatCLIP [17] and GeoCLIP [18] learn location embeddings that align satellite imagery with geographic coordinates. The Major TOM data framework [19], [20] provides open-access embeddings derived from multiple frozen foundation model encoders applied to globally sampled satellite data. The Google Satellite Embedding dataset, produced with AlphaEarth Foundations, and TESSERA provide annual embedding layers at $10\,\mathrm{m}$ resolution [14], [15], [21], whereas LGND Clay Embeddings provides near-global chip-level vectors with spatial support of 1.28 or $2.56\,\mathrm{km}$ [22], [23].

In this review, a satellite image embedding represents a pixel, patch, scene, or time series derived from EO observations; a location embedding represents a geographic coordinate and does not require imagery at query time. A reusable embedding encoder produces vectors for user-supplied inputs, whereas an Earth embedding product publishes precomputed vectors with spatial or temporal indexing. The review focuses on global or near-global Earth embedding products and discusses foundation models and reusable encoders where they explain how those products are constructed, evaluated, or used.

Distributing embeddings rather than only model weights separates large-scale representation inference from task-specific prediction (Fig. 1). Researchers with labeled observations can fit downstream models without reproducing the original inference workload, while product providers assume the cost of large-area encoding, storage, and updates. Word2Vec [24] and GloVe [25] introduced a comparable separation in natural language processing (NLP) by providing reusable semantic vectors for text analysis. Earth embeddings provide reusable features for geospatial data, while recent products increasingly encode multiple dates and sources rather than a single image. The move toward multitemporal, multisource vectors resembles the transition from static word vectors to contextualized language representations [26].

B. Related Surveys and Our Contributions

Existing surveys provide complementary accounts of geospatial representation learning. Reviews of remote sensing and geospatial foundation models organize pretraining objectives, architectures, multimodal fusion, and transfer protocols [27]–[36]. Embedding-focused reviews, perspectives, and

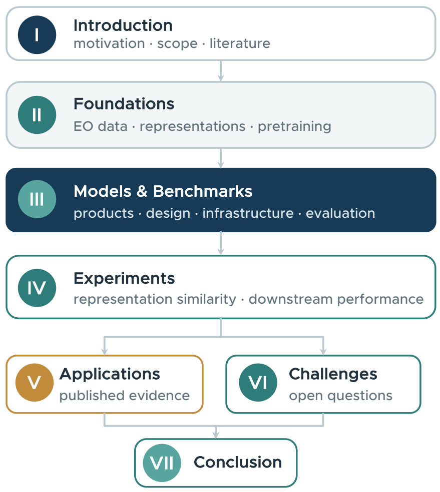

Fig. 3. Organization of the survey.

chapters clarify the distinctions among image, location, patch, and pixel embeddings and examine their compression, access, standardization, and scientific use [37]–[42]. These studies establish the methodological and conceptual background, but comparisons of released products, access infrastructure, evaluation protocols, and downstream applications remain distributed across separate lines of work.

This survey places global and near-global embedding products at the center of the review. It distinguishes precomputed embedding layers and datasets from reusable encoders, compares their input data, spatial and temporal support, dimensionality, and release formats, and examines the infrastructure through which users can obtain or query them. It also relates community benchmarks to published applications and directly compares multiple embeddings through representation geometry, land-cover classification, continuous-variable regression, and sensitivity to embedding dimension. The resulting account connects how Earth embeddings are produced and distributed with how they are evaluated and used, while identifying common requirements for updating, compatibility, and long-term access.

Fig. 2 summarizes temporal, thematic, and geographic patterns in the literature considered in this survey. Annual records retrieved through OpenAlex [43] and the satellite embedding literature both increase sharply after 2023. The keyword cloud emphasizes recurring terms such as *foundation models*, *Earth observation*, *embeddings*, *multimodal*, *self-supervised*, and *temporal*. The co-occurrence network links data sources such as *Sentinel-2*, *SAR*, and *Landsat* with learning methods, embedding concepts, and applications in land cover, agriculture, environmental monitoring, and ecology. The affiliation map shows substantial contributions from North America, Europe, and Asia. Together, the four panels show that Earth embedding research is growing rapidly across methods, applications, and regions.

C. Organization of This Survey

The organization of the survey is illustrated in Fig. 3. Section II reviews the data, feature representations, and pretraining methods behind Earth embeddings, and Section III examines models, released products, design choices, distribution infrastructure, and evaluation benchmarks. Section IV describes the evaluation data and analyzes representation geometry, downstream classification and regression, and sensitivity to embedding dimension. Section V reviews published applications, Section VI discusses unresolved technical and scientific problems, and Section VII concludes the survey.

II. Foundations

Global embedding products encode heterogeneous Earth observation measurements as compact vectors. Interpreting these vectors requires knowledge of their input data, feature representations, pretraining objectives, and embedding-space properties. Fig. 4 connects these components with models, access infrastructure, and applications; Section III examines the models, products, and evaluation protocols.

A. Earth Observation Data Sources

Earth observation sources enter representation learning in different roles: some are direct encoder inputs, some provide targets or auxiliary supervision during pretraining, and others are used only as downstream labels or covariates. Surface imagery from Sentinel-2, Landsat, HLS, and Sentinel-1 forms the main input to many of the models summarized here because these missions combine broad coverage with repeated observations [44]–[46]. ALOS-2 PALSAR-2 [47], GEDI [48], ERA5-Land [49], Copernicus GLO-30 DEM [50], VIIRS [51], Sentinel-3 [52], ICESat-2 ATL08 [53], Sentinel-5P [54], PlanetScope [55], and NAIP [56] contribute structural, environmental, atmospheric, or higher-resolution information in selected models and benchmarks. Embedded Seamless Data (ESD) [57] is generated from the Global 30 m Seamless Data Cube of Land Surface Reflectance (SDC30) [58], which harmonizes Landsat 5, 7, 8, and 9 with MODIS Terra into a gap-filled daily reflectance record.

Table I compares the listed sources and their use in geospatial representation learning. Sentinel-2 and Sentinel-1 appear most often in current GFM and embedding pipelines, while Landsat and HLS provide longer temporal coverage. GEDI and elevation products add information about vertical structure and terrain; ERA5-Land, ERA5, and Sentinel-5P supply environmental variables at coarser resolution. PlanetScope, NAIP, VIIRS, Sentinel-3, and ICESat-2 are used more selectively. Their use depends on geographic coverage, co-registration, temporal alignment, access conditions, cost, and licensing as well as information content.

Combining optical reflectance, SAR backscatter, terrain, and climate can preserve signals that are absent from any single source. AlphaEarth Foundations, for example, is trained with several observation and supervision sources, while inference uses optical, thermal, and SAR observations from Sentinel-2, Landsat 8/9, and Sentinel-1 [14]. The combination also introduces source-specific errors and missing observations. Optical acquisitions are affected by clouds, which can obscure more than 50% of observations in tropical regions [79]; SAR data contain speckle and layover artifacts; and multi-temporal

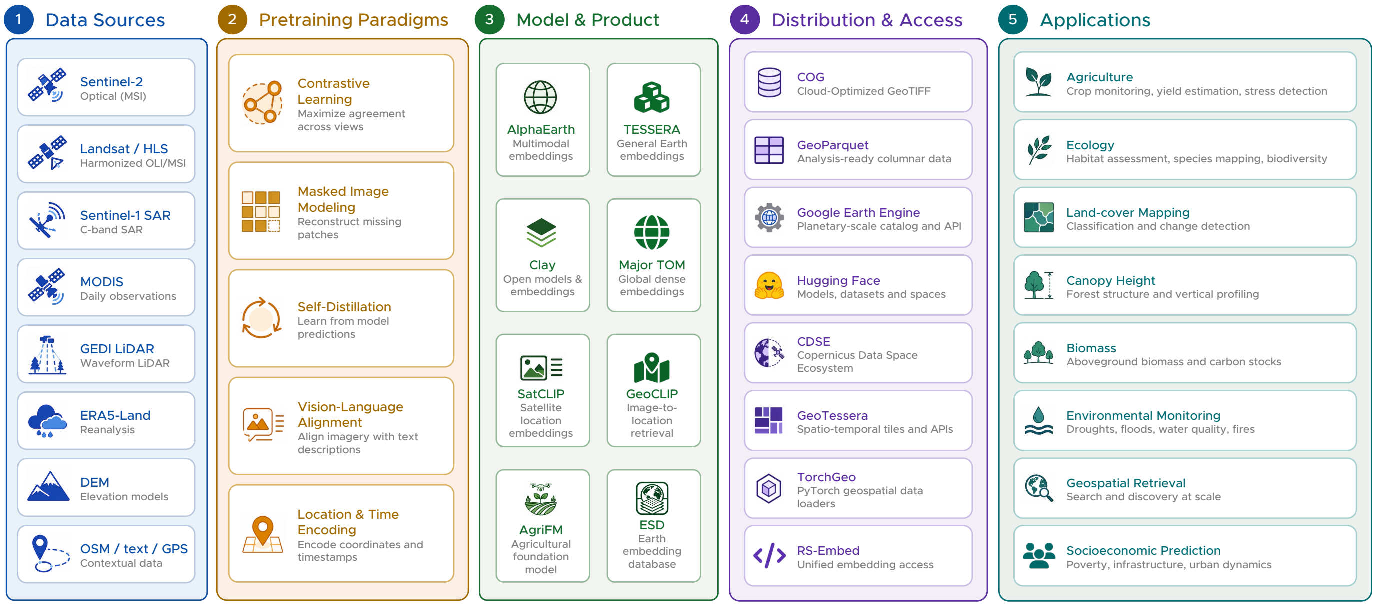

Fig. 4. Data sources, pretraining methods, models, access infrastructure, and applications covered in this survey.

TABLE I
REPRESENTATIVE EARTH OBSERVATION DATA SOURCES USED IN GEOSPATIAL REPRESENTATION LEARNING.

Source / Product	Modality	Time span	Resolution	Cadence	Representative uses
Sentinel-2 MSI [44]	Optical multispectral (13 bands)	2015–	10–60 m	5 days	High (SatMAE [59]; Copernicus-FM [60]; AlphaEarth [14])
Landsat 8/9 [61]	Optical and thermal (11 bands)	2013/2021–	15/30/100 m	8 days	High (MOSAIKS [16]; Presto [62]; AlphaEarth [14])
HLS L30/S30 [3], [45]	Optical and thermal (11/13 bands)	2013/2015–	30 m	1.4 days avg.	Medium (Prithvi-EO [10]; GEO-Bench-2 [63])
MODIS [64]	Optical and thermal (36 bands)	2000–	250 m–1 km	1–2 days	Medium (ESD [57]; SEN12MS [65])
VIIRS [51]	Visible and infrared (22 bands)	2011–	375–750 m	daily	Low (few current foundation model examples)
Sentinel-3 (OLCI, SLSTR) [52]	Optical and thermal (21 + 9 channels)	2016–	300 m–1 km	1–2 days	Low (Copernicus-FM / Copernicus-Bench [60])
Sentinel-1 SAR [46]	C-band SAR	2014–	10 m	6–12 days	High (CROMA [66]; SoftCon [67]; AlphaEarth [14])
ALOS-2 PALSAR-2 [47]	L-band SAR	2014–	10–100 m	14 days	Low (AlphaEarth [14]; RingMoE [68])
GEDI [48]	Waveform LiDAR	2019–	25 m footprints	irregular	Medium (AlphaEarth [14]; MMEarth [69])
ICESat-2 ATL08 [53]	Photon LiDAR	2018–	100 m along-track	91 days	Low (few current foundation model examples)
Copernicus GLO-30 DEM [50]	Digital elevation model	static	30 m	static	Low (AlphaEarth [14]; Copernicus-FM [60])
SRTM [70]	Digital elevation model	static	30 m	static	Low (Presto [62])
ASTER GDEM [71]	Digital elevation model	static	30 m	static	Low (few current examples)
ERA5-Land [49]	Reanalysis	1950–	∼9 km	hourly	Low (AlphaEarth [14])
ERA5 [72]	Reanalysis	1940–	∼31 km	hourly	Medium (Presto [62]; Climplicit [73]; MMEarth [69])
Sentinel-5P / TROPOMI [54]	Atmosphere	2017–	5.5–7 km	daily	Low (Copernicus-FM / Copernicus-Bench [60])
PlanetScope [55]	Commercial optical (4–8 bands)	2017–	3 m	near-daily	Medium (DynamicEarthNet [74]; SpaceNet7 [75]; GEO-Bench-2 [63])
NAIP [56]	Aerial optical (4 bands)	2003– (U.S.)	0.6–1 m	2–3 years	Medium (Tile2Vec [76]; SatlasPretrain [77]; USat [78])

stacks are sampled irregularly because of orbit geometry and revisit gaps. Models that produce spatially consistent embeddings must account for these differences in availability, noise, and geometry [36], [80].

Implementations combine these inputs differently. AlphaEarth Foundations [14] uses source-specific encoders whose outputs feed a common spatiotemporal representation; missing frames or input sources can be accommodated at inference. TESSERA [21] processes optical and SAR imagery with separate encoders and aligns their outputs through the training objective. The Clay Foundation Model [22] represents each modality as a distinct token type in a Vision Transformer and includes modality-aware positional information. TerraMind [81] and TerraFlow [82] quantize modalities into discrete tokens and predict target tokens from the available context. CROMA [66] uses cross-attention to reconstruct one modality from masked observations of another. The choice depends on source availability, temporal alignment, and missing-input handling.

B. Feature Representations

Feature representations convert Earth observation measurements into variables that downstream methods can use. Current remote sensing workflows use task-specific indices and texture descriptors, label-supervised feature maps, self-supervised encoders, and precomputed embedding layers. These representations differ in their supervisory signals, retained information, and downstream computation.

1) Hand-Crafted Descriptors: Hand-crafted indices and descriptors condense multi-band imagery into variables selected for a particular task. The normalized difference vegetation index (NDVI) [83], computed from red and near-infrared reflectance, remains a standard indicator of vegetation condition; related formulations target water bodies (NDWI [84]), built-up areas (NDBI [85]), and snow cover (NDSI [86]). Grey-level co-occurrence matrices (GLCM) [87] and local binary patterns (LBP) [88] describe texture and are commonly paired with random forest (RF) or support vector machine (SVM) classifiers [89]–[91]. Such features are interpretable and inexpensive, but their task-specific definitions retain only selected spectral and spatial information.

2) Label-Supervised Deep Representations: Label-supervised deep representations use scene labels, segmentation masks, or continuous target variables as the supervisory signal. Convolutional networks pretrained on ImageNet [92], including VGG [93] and ResNet [94], supplied hierarchical features for remote sensing scene classification and semantic segmentation [95], [96]. Recurrent networks, including long short-term memory networks [97], extended learned features to temporal sequences, and Vision Transformers introduced attention-based image representations [98]. These models capture spatial patterns that fixed descriptors do not encode, but their features depend on labeled training data. Transfer from natural imagery is also limited by differences in viewpoint, spectral channels, and spatial organization, especially for tasks that require spectral or temporal information [99], [100].

3) Self-Supervised EO Representations: Self-supervised EO methods derive supervision from the observations rather than task labels. Tile2Vec [76] uses spatial proximity, Seasonal Contrast (SeCo) [100] uses multi-date observations of the same location, and SSL4EO-S12 [101] supplies Sentinel-1/2 data for comparing contrastive, distillation, and reconstruction objectives. RingMo [102], SatMAE [59], Scale-MAE [12], SkySense [103], and DINOv3 [104] extend self-supervised learning to multispectral, multimodal, or multitemporal inputs. These methods reduce dependence on downstream labels, but users must still obtain the model weights, reproduce the required preprocessing, and run the encoder over their study regions.

4) Embedding Products: Embedding products release precomputed vectors rather than requiring every user to run the encoder. MOSAIKS [16] provided a shared global feature set for environmental and socioeconomic prediction, while Major TOM [19], [20] released vectors from multiple frozen encoders over globally sampled satellite tiles. LGND distributes near-global chip embeddings generated with Clay [22], [23]; TESSERA v1 and the Google Satellite Embedding dataset produced with AlphaEarth Foundations provide dense annual layers [14], [15], [21]; and ESD retains a temporally indexed record [57]. TESSERA v2 extends the product design with distilled temporal encoders and selectable output dimensions [105]. Downstream analysis can begin with released vectors and a task-specific prediction model, while storage, access, updating, version compatibility, and interpretation remain product concerns.

C. Pretraining Paradigms

Representation type determines both the available information and the computation required downstream, while the pretraining objective determines which differences between observations are suppressed and which information remains accessible. It therefore affects transfer performance, neighborhood structure, and compressibility. The discussion below relates each objective to these representation properties; storage and distribution are considered in Section III.

1) Contrastive Objectives: Contrastive objectives learn representations by bringing matched views closer in embedding space and pushing mismatched views apart. Given a positive pair (z_i, z_j) and a set of $2N$ augmented views within a minibatch, the InfoNCE loss [5], [106] is

$$\mathcal{L}_{\text{CL}} = -\log \frac{\exp\big(\text{sim}(z_i, z_j)/\tau\big)}{\sum_{k=1}^{2N} \mathbf{1}_{[k\neq i]} \exp\big(\text{sim}(z_i, z_k)/\tau\big)}, \qquad (1)$$

where $\text{sim}(\cdot,\cdot)$ denotes cosine similarity and τ is a temperature parameter. In EO, the definition of positive and negative pairs is as important as the loss. SeCo [100] treats observations of the same location in different seasons as positives, encouraging invariance to seasonal and atmospheric variation. CACo [107] modifies temporal pairing to distinguish short-term variation from persistent change. Tile2Vec [76] instead defines pairs through geographic proximity and uses a triplet objective adapted from distributional semantics:

$$\mathcal{L}_{\text{triplet}} = \max\left(0,\ d(f(x_a), f(x_p)) - d(f(x_a), f(x_n)) + m\right), \qquad (2)$$

where x_a, x_p, and x_n denote an anchor tile, a nearby tile, and a distant tile, respectively. SSL4EO-S12 [101] supplies Sentinel-1/2 data for comparing contrastive and alternative objectives at scale. Pairing policy determines the learned invariance: seasonal pairs reduce sensitivity to seasonal variation, spatial pairs promote local similarity, and image–location pairs in SatCLIP and GeoCLIP [17], [18] introduce geographic information. These invariances are useful only when the downstream target does not require the suppressed variation.

2) Reconstruction Objectives: Reconstruction objectives mask part of the input and train the model to recover the missing content, encouraging the encoder to preserve local structure and context. For masked autoencoders [7], the loss is

$$\mathcal{L}_{\text{MAE}} = \frac{1}{|\mathcal{M}|} \sum_{p\in\mathcal{M}} \|\mathbf{x}_p - \hat{\mathbf{x}}_p\|^2, \qquad (3)$$

where $\mathcal{M}$ is the set of masked patches, $\mathbf{x}_p$ is the original content, and $\hat{\mathbf{x}}_p$ is its reconstruction. RingMo [102], SatMAE [59], Scale-MAE [12], SpectralGPT [11], Clay [22], and Prithvi-EO-2.0 [10] apply this objective to multispectral, multiscale, or multitemporal inputs, while Presto [62] adapts reconstruction to multisensor pixel time series. Because the encoder must predict missing content, these objectives encourage retention of spatial, spectral, or temporal context. Benefits depend on the mask design, encoder output, and downstream adaptation.

3) Redundancy-Reduction Objectives: Some models aim not primarily to reconstruct the input, but to produce invariant embeddings with minimal redundancy across dimensions. The Barlow Twins criterion [108] operates on the cross-correlation matrix $\mathbf{C}$ between embeddings of two valid views:

$$\mathcal{L}_{\text{Barlow}} = \underbrace{\sum_i (1 - C_{ii})^2}_{\text{invariance}} + \lambda \underbrace{\sum_i \sum_{j\neq i} C_{ij}^2}_{\text{redundancy reduction}}, \qquad (4)$$

TABLE II
FEATURE-REPRESENTATION FAMILIES IN EARTH OBSERVATION.

Feature Representation	Supervision	Representative examples	Output form	Characteristics
Hand-crafted descriptors	Expert-designed formulas and statistics	Spectral indices (NDVI, NDWI, NDBI, NDSI) [83]–[86] Texture descriptors (GLCM, LBP) [87], [88] Classical ML (RF, SVM) [91]	Scalars or low-dimensional descriptors	Interpretable and inexpensive, but task-specific and context-limited
Label-supervised deep representations	Human annotations such as class labels, masks, or target variables	CNN-based features (VGG, ResNet) [93], [94] RNN-based temporal encoders (LSTM) [97] Transformer-based encoders (ViT) [98]	Feature maps or latent vectors	Hierarchical and task-effective, but label-dependent and domain-sensitive
Self-supervised EO representations	Pretext tasks derived from unlabeled EO archives	Contrastive models (Tile2Vec, SeCo) [76], [100] Masked autoencoders (SatMAE, Scale-MAE) [12], [59] Self-distillation (SSL4EO-S12 DINO, DINOv3) [101], [104]	Latent features extracted by inference	Scalable and domain-adapted, but still largely model-centric
Embedding products	Inherited from pretrained encoders and released in precomputed form	Global feature collections (MOSAIKS, Major TOM) [16], [19], [20] Dense embedding products (LGND, TESSERA, Google Satellite Embedding, ESD) [14], [15], [21]–[23], [57]	Precomputed vector fields or embedding layers	Directly reusable, but constrained by storage, interoperability, and update cycles

where $C_{ij} = \sum_b z^A_{b,i}\, z^B_{b,j} / \sqrt{\sum_b (z^A_{b,i})^2 \sum_b (z^B_{b,j})^2}$ is the cross-correlation between dimensions i and j computed over a batch of augmented pairs (A, B). TESSERA v1 [21] applies this criterion to annual Sentinel-1/2 time series, and TESSERA v2 [105] retains it while varying encoder capacity, training-data volume, and compute. DeCUR [109] uses a related objective to separate common and modality-specific information. Decorrelation reduces redundancy but does not measure retained task information.

4) Distillation Objectives: Distillation objectives replace explicit pixel reconstruction with consistency between a student and a teacher or target encoder. DINO [8], DINOv2 [9], and DINOv3 [104] provide frozen features learned through this strategy. Panopticon [110] adapts DINOv2 to sensor-variable EO observations through channel attention and cross-sensor views of the same footprint. I-JEPA [111] and AnySat [112] instead predict targets in representation space. TESSERA v2 [105] distills a temporal teacher into compact student encoders whose 128-dimensional output can be shortened without retraining, while Major TOM [19], [20] distributes globally sampled vectors from frozen encoders in the DINOv2 family. Fair comparisons with reconstruction objectives require matched architectures, data, and evaluation protocols.

5) Alignment and Generative Objectives: Alignment objectives learn a shared space for paired modalities. CLIP [113] optimizes a symmetric image–text contrastive loss over a batch of N matched pairs:

$$\mathcal{L}_{\text{CLIP}} = -\frac{1}{2N} \sum_{i=1}^{N} \Bigg[\log \frac{e^{\text{sim}(v_i, t_i)/\tau}}{\sum_j e^{\text{sim}(v_i, t_j)/\tau}} + \log \frac{e^{\text{sim}(t_i, v_i)/\tau}}{\sum_j e^{\text{sim}(t_i, v_j)/\tau}} \Bigg], \tag{5}$$

where v_i and t_i are the image and text embeddings, respectively. In EO, the paired input may be text, coordinates, ground imagery, or another observation of the same place. Remote-CLIP [114], GRAFT [115], GeoCLIP [18], SatCLIP [17], SoundingEarth [116], and Sat2Cap [117] use different pairings to support retrieval, geolocalization, or cross-modal queries. The structure of the shared space consequently reflects both the data modality and the definition of matched locations.

Generative and predictive objectives infer a missing modality, timestamp, or token stream from the available context. TerraMind [81] tokenizes multiple geospatial modalities and predicts selected targets, and TerraFlow [82] applies this formulation to temporal inputs. Copernicus-FM [60] and Galileo [118] combine reconstruction with cross-view discrimination. AlphaEarth Foundations [14] combines source-specific reconstruction, consistency constraints, and text alignment before releasing annual global embedding layers. Attributing a downstream property to one loss requires ablations that vary that loss while holding the other components fixed.

Each objective balances invariance against sufficiency by suppressing selected variation while retaining information needed for its training target. Contrastive and distillation methods tend to emphasize discrimination or agreement, reconstruction methods retain information needed to predict missing inputs, and multimodal objectives preserve shared structure across sources. Objective names alone do not predict downstream suitability; performance depends on whether task-specific variation remains recoverable.

D. Embedding Space Properties

Embedding geometry and dimensionality affect similarity calculations, storage, and interpretation [38]. For released embeddings, the main questions are whether vectors are constrained to a particular space, how training controls information retention, and how nominal dimension relates to the variation present in the vectors.

Many released encoders produce vectors in $\mathbb{R}^d$ without an explicit norm constraint. Examples include Clay [22], Prithvi-EO-2.0 [10], SatMAE [59], TESSERA [21], and the DINOv2-derived embeddings distributed by Major TOM [20]. Cosine similarity is commonly used to compare such vectors $\mathbf{u}$ and $\mathbf{v}$:

$$\text{sim}(\mathbf{u}, \mathbf{v}) = \frac{\mathbf{u} \cdot \mathbf{v}}{\|\mathbf{u}\| \, \|\mathbf{v}\|}. \tag{6}$$

An unconstrained output can occupy a lower-dimensional subspace of the available coordinates, a behavior described as *dimensional collapse* [119]. Cosine similarity also removes vector norm at evaluation time even when norm was unconstrained during training. Uniformity on the hypersphere has been associated with downstream performance in general representation learning [120], although the relationship has not been established across Earth embedding products. AlphaEarth Foundations [14] explicitly places its output on the unit hypersphere $\mathbb{S}^{d-1}$ through a von Mises–Fisher (vMF) variational bottleneck. For $\mathbf{z} \in \mathbb{S}^{d-1}$, the distribution is parameterized by a mean direction $\boldsymbol{\mu} \in \mathbb{S}^{d-1}$ and concentration $\kappa \geq 0$:

$$p(\mathbf{z} \mid \boldsymbol{\mu}, \kappa) = C_d(\kappa)\, \exp\!\big(\kappa\, \boldsymbol{\mu}^\top \mathbf{z}\big), \tag{7}$$

where $C_d(\kappa)$ is a normalization constant. AlphaEarth combines this distribution with a batch-uniformity penalty that discourages concentration in a limited region of $\mathbb{S}^{63}$ [14]. Unlike the embeddings above, AlphaEarth uses spherical geometry; its effect requires evaluation with the same data and tasks.

Cross-modal encoders introduce a second geometric issue. Separate encoders can occupy different regions of a nominally shared space, a phenomenon termed the *modality gap* [121]. GeoCLIP [18] aligns images and coordinates, whereas RemoteCLIP [114] aligns remote sensing imagery and text. Work on natural images links the gap to zero-shot performance and fairness differences [121], but few geospatial studies have measured it. Recent analyses use sparse concept decompositions and neuroscience-inspired probes to examine the information carried by location and Earth observation embeddings [122], [123]. Within- and cross-modal neighborhood analyses can complement downstream accuracy when these spaces are evaluated.

The information bottleneck provides a conceptual description of how an encoder can discard input variation while retaining information about a target [124]. Let X denote the input, Z the embedding, and Y a downstream target. For a stochastic encoder $p(\mathbf{z} \mid \mathbf{x})$, the objective is

$$\min_{p(\mathbf{z}|\mathbf{x})}\; I(Z;X) - \beta\, I(Z;Y), \tag{8}$$

where $\beta > 0$ controls the balance between compression and target relevance. In self-supervised pretraining, the set of future targets Y is unknown, so this equation offers an interpretation rather than a directly optimized objective for most Earth embedding models. AlphaEarth fixes the vMF concentration at $\kappa = 8 \times 10^3$ [14]; this controls distributional concentration but does not by itself provide a measured bound on $I(Z;X)$. TESSERA [21] reduces cross-dimensional correlation with Barlow Twins [108], whereas masked-autoencoder models such as Clay [22] rely primarily on architecture and output dimension to limit the code. Their relationship to mutual information has not been compared with matched EO data, architectures, and evaluation protocols [30], [36].

Reported full output dimensions range from 64 for AlphaEarth [14] to 8,192 for MOSAIKS [16], while TESSERA v2 [105] supports prefixes as short as 16 dimensions; Section III compares the associated storage costs. Nominal dimension does not reveal how many directions contain substantial variation. Participation ratio and effective rank summarize the spectrum of the embedding covariance matrix, whereas manifold estimators characterize nonlinear degrees of freedom. Rao et al. [125] estimate a manifold dimension of 2–10 for the geographic implicit neural representations studied in GeoINRID. That result applies to coordinate-based representations under the paper's data and estimator choices and should not be generalized to satellite embedding products. Effective dimension, compression loss, and downstream accuracy must be measured for each representation; principal component analysis (PCA) [126] and product quantization [127] provide possible reductions, but the attainable savings depend on the target and evaluation protocol. Product documentation should therefore report the nominal dimension, numeric precision, normalization, recommended distance measure, and any empirical estimate of effective dimension.

III. Models and Benchmarks

Earth observation representations are available as model weights, reusable encoders, and precomputed vectors. Spatially and temporally indexed vectors let users begin downstream analysis without first running the source model over the study area. Comparisons must therefore consider spatial support, temporal aggregation, compression, access, and fixed-feature evaluation in addition to architecture and pretraining.

A. Models and Products

Fig. 5 outlines four stages in the development of Earth embeddings. Early studies learned reusable features from satellite imagery; later work increased model scale and incorporated additional sensors and supervision. The most recent stage centers on large embedding collections, benchmark-based evaluation, common access tools, and data standards.

We distinguish releases by what users receive. Geospatial foundation models usually provide weights and code, reusable embedding encoders generate vectors for user-supplied inputs, and embedding products provide vectors computed over a spatial collection. Recent embedding-centered surveys similarly distinguish model access from direct access to embeddings [37], [41]. Table III compares representative models, embedding datasets, and released layers.

1) Geospatial Foundation Models: Geospatial foundation models supply the encoders used to generate many Earth embeddings, but their usual releases are checkpoints, code, and fine-tuning recipes rather than precomputed global vectors. Users must prepare the required sensor inputs, run inference, and select a feature or aggregation method. Masked and scale-aware image encoders include SatMAE [59], Scale-MAE [12], RingMo [102], Prithvi-EO [10], Presto [62], and USat [78]. CROMA [66], DOFA [13], Panopticon [110], OmniSat [128], AnySat [112], Galileo [118], and Copernicus-FM [60] support additional sensors or modalities, while SkySense [103], TerraMind [81], and TerraFlow [82] use generative or temporal objectives. msGFM, RobSense, and SkySense V2 extend cross-sensor encoding and robustness to heterogeneous or incomplete inputs [129]–[131]; SeaMo, TiMo, TerraFM, and GeoLink address seasonal sequences, satellite time series, globally sampled radar–optical imagery, and OpenStreetMap supervision, respectively [132]–[135]. GFM surveys provide more complete model inventories [29]–[34], [36]; the models listed here still require users to generate the embeddings.

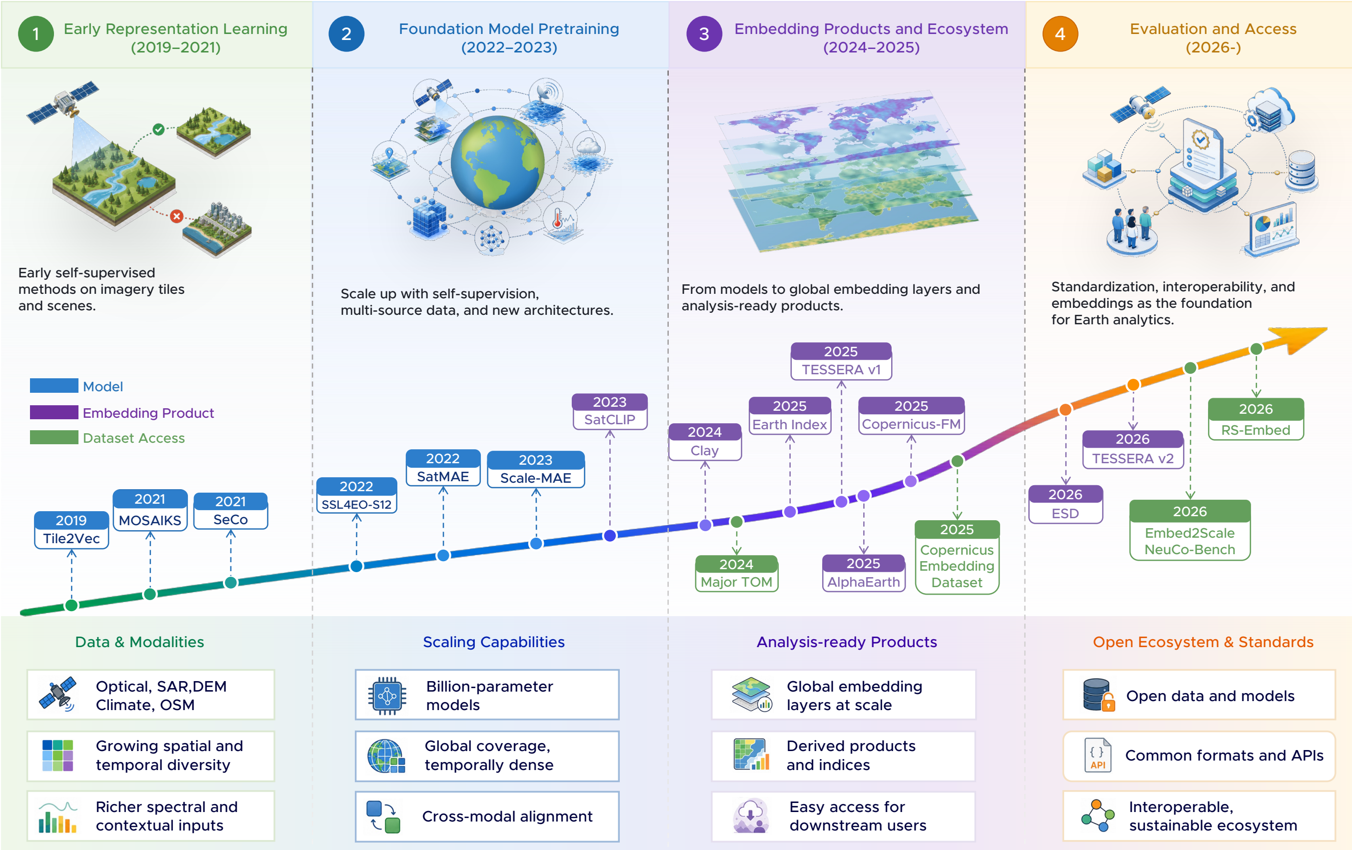

Fig. 5. Evolution of Earth embedding research from representation learning to products, evaluation, and access.

2) Released Embedding Products: Released embedding products provide precomputed vectors for a defined spatial and temporal collection. Users can download or query the vectors, join them with labels or covariates, and train downstream models without repeating the source encoder's large-area inference. Tile2Vec [76], SeCo [100], GASSL [136], SSL4EO-S12 [101], SatMAE [59], Scale-MAE [12], SatCLIP [17], and GeoCLIP [18] established reusable image or location encoders but did not release complete global embedding layers. Precomputed collections differ in spatial support and completeness: MOSAIKS provides global features [16], Major TOM Embeddings releases vectors from multiple encoders for globally sampled tiles [19], [20], and Earth Index encodes billions of overlapping patches [137]. Clay v1.5 is a model release [22], whereas LGND Clay Embeddings is a separate near-global dataset generated with that encoder [23].

Dense, temporally indexed releases include TESSERA v1 [21], the Google Satellite Embedding dataset produced with AlphaEarth Foundations [14], [15], and ESD, a record at 30 m resolution beginning in 2000 [57]. TESSERA v2 studies distilled temporal encoders and selectable dimensions within the same product family [105]. The Copernicus Data Space distributes more than 60 TB of embeddings generated by several frozen encoders [138], while Earth Embeddings as Products provides common loaders for accessing multiple releases [37].

Table III uses CL, MAE, SD, RCF, VLA, and FSQ for contrastive learning [5], masked autoencoding [7], self-distillation [8], random convolutional features [16], vision–language alignment [113], and finite scalar quantization [139], respectively. The year is the formal publication year of the cited paper or, for dataset records without a paper, the first public-release year. *Res.* denotes the ground support of one vector; checkmarks under *Time* and *Global* indicate that one vector combines multiple dates and that a global or near-global collection is publicly available. A dagger marks precomputed vectors released through Major TOM, while an asterisk marks vectors released through the Copernicus Global Embedding Dataset.

Spatial support ranges from coordinates and scenes to per-pixel grids, and training objectives distinguish models with otherwise similar architectures. Patch and tile collections include MOSAIKS [16], Earth Index [137], Major TOM [20], the Copernicus Global Embedding Dataset [138], and LGND, which is generated with the separately released Clay v1.5 model [22], [23]. Annual pixel-level products include TESSERA v1 [21] and Google Satellite Embedding [14], [15], whereas ESD provides a compressed 30-meter record covering approximately a quarter century [57]. TESSERA v2 combines a temporal teacher with compact students and allows shorter vectors when storage is constrained [105].

3) Reusable Embedding Encoders: Reusable embedding encoders provide weights for extracting vectors from new inputs but do not include complete global embedding layers. Im-

TABLE III
COMPARISON OF REPRESENTATIVE EARTH EMBEDDING MODELS AND PRODUCTS.

Model / Product	Year	Architecture	Training objective	Dim.	Res.	Modalities	Time	Global	Format
Tile2Vec [76]	2019	ResNet-18	Triplet CL	512	1.5 km	Optical			Weights
MOSAIKS [16]	2021	Random conv.	RCF	8192	1.1 km	Optical		✓	CSV / NPY
SeCo [100]	2021	ResNet-50	MoCo-v2 CL	2048	2.65 km	Optical			Weights
Prithvi-EO-2.0 [10]	2026	ViT-L / ViT-H	MAE	1024/1280	–	Multispectral	✓		HF / TerraTorch
CSP [140]	2023	MLP + ResNet-50	CL	256	Coordinate	Optical + coord.			PyTorch weights
SatCLIP [17]	2025	Spherical-harmonic MLP	Image–location CL	256	Coordinate	Optical + coord.			PyTorch weights
GeoCLIP [18]	2023	Fourier features + MLP	Image–location CL	512	Coordinate	Image + coord.			PyTorch weights
Major TOM Embeddings [19], [20]	2024	Multiple frozen encoders	Frozen inference	1024–2048	2.24–3.84 km	Optical + SAR		✓	Parquet / HF
DINOv2† [9], [20], [141]	2024	ViT-L/14	SD	1024	2.24 km	Optical		✓	Parquet / HF
SigLIP† [20], [142], [143]	2024	ViT-SO400M/14	VLA	1152	3.84 km	Optical + text		✓	Parquet / HF
SSL4EO-DINO† [20], [101]	2024	ResNet-50	DINO (SD)	2048	2.24 km	Multispectral		✓	Parquet / HF
SSL4EO-MoCo† [20], [101]	2024	ResNet-50	MoCo-v2 CL	2048	2.24 km	SAR		✓	Parquet / HF
Clay v1.5 [22]	2024	ViT	MAE	1024	–	MS + SAR + DEM			Weights
LGND Clay Embeddings [23]	2026	Clay v1.5 encoder	MAE	256/1024	1.28/2.56 km	Optical	✓	✓	GeoParquet / Source Coop.
Earth Index [137]	2025	SoftCon ViT-S/14	Soft contrastive learning	384	320 m	Optical		✓	GeoParquet / Source Coop.
TESSERA v1 [21]	2026	Transformer + GRU	Barlow Twins	128	10 m	Optical + SAR	✓	✓	NumPy / GeoTessera
TESSERA v2 [105]	2026	Dual-branch Transformer	Barlow Twins + distillation	16–128	10 m	Optical + SAR	✓		–
Google Satellite Embedding [14], [15]	2025	STP encoder	Reconstruction + CL + vMF	64	10 m	Optical + thermal + SAR	✓	✓	Earth Engine / COG
Copernicus Embeddings [138]	2025	Multiple frozen encoders	Frozen inference	Varies	Varies	Optical + SAR		✓	GeoParquet / CDSE
DeCUR* [109], [138]	2025	ResNet-50	Cross-modal CL	2048	2.24 km	Multispectral + SAR		✓	GeoParquet / CDSE
MMEarth* [69], [138]	2025	ConvNeXt-V2	MAE	Varies	2.24 km	Multimodal EO		✓	GeoParquet / CDSE
Copernicus-FM [60]	2025	ViT	MAE + SD	768	–	Multimodal EO + DEM	✓		PyTorch weights
Copernicus-Embed [60], [144]	2025	Copernicus-FM encoder	Frozen inference	768	0.25°	Multimodal EO + DEM	✓	✓	Parquet / NPZ / PT
ESD [57]	2026	Temporal CNN + FSQ	Reconstruction + supervised tasks	13	30 m	Optical + DEM	✓	✓	MGRS tiles

† Embeddings released through Major TOM; * embeddings included in the Copernicus Embedding Dataset.

age and temporal encoders include Tile2Vec [76], SeCo [100], SSL4EO-S12 [101], SatMAE [59], Scale-MAE [12], DINOv2 [9], SigLIP [142], Prithvi-EO [10], and Presto [62]. DeCUR [109], MMEarth [69], CROMA [66], DOFA [13], Panopticon [110], AnySat [112], Galileo [118], TerraMind [81], TerraFlow [82], and Copernicus-FM [60] support multiple sensors or modalities; Panopticon uses channel-level conditioning to apply one frozen encoder to optical, hyperspectral, and radar inputs. RemoteCLIP [114], GeoRSCLIP [145], GRAFT [115], SkyScript [146], Sat2Cap [117], and SoundingEarth [116] align imagery with text or other co-located observations. RS-Embed provides a common interface for generating vectors from selected checkpoints [147], [148].

4) Location Embeddings: Location embeddings map geographic coordinates directly to vectors, without requiring imagery at query time. One group of methods determines how position is represented geometrically. Space2Vec uses multiscale periodic functions in planar coordinates [149], whereas Sphere2Vec and spherical-harmonic encoders operate on the Earth's surface to reduce projection distortion and represent several spatial scales [150], [151]. Localized Slepian encodings concentrate basis functions within a region of interest [152]. Continuous or adaptive representations instead learn spatial structure from observations: SINR learns a coordinate field for global species mapping [153], while Tessellating the Earth replaces a fixed basis with learnable spherical Voronoi partitions and shared semantic tokens trained with satellite imagery [154].

The semantic content of a coordinate vector is determined by its supervision. CSP, SatCLIP, GeoCLIP, and SatCLE align coordinates with co-located imagery or image-derived semantics [17], [18], [140], [155]. S2Vec instead uses built-environment features, MoRA incorporates mobility and demographic signals, and OSMGraphCLIP uses OpenStreetMap graphs [156]–[158]. UniGeoCLIP jointly aligns coordinates, aerial and street-level imagery, elevation, and text, while GAIR learns coordinate-level representations aligned with overhead and street-level imagery [159], [160]. The resulting proximity may therefore reflect physical distance, visual similarity, environmental conditions, or human activity.

Location encoders can also incorporate task-specific context rather than act as fixed geographic priors. RANGE augments coordinate embeddings with retrieved visual features [161], whereas proxy consistency learning incorporates widely available geospatial proxy variables into a trainable location encoder for sparsely labeled prediction tasks [162]. A task-adapted location representation is not interchangeable with a frozen general-purpose encoder. TorchSpatial and LocBench compare 15 location encoders across classification and regression tasks and examine geographic bias [163]. Unlike released raster layers, these approaches can return a compact vector for an arbitrary coordinate, but its content depends on the training observations, spatial basis, and downstream adaptation protocol.

Reusable EO encoders have also been studied for multisensor transfer, sensor-variable imagery, cross-modal alignment, retrieval, and compression [17], [20], [21], [114], [115], [164]–[180]. Benchmarks, reviews, and software now compare fixed representations, compression, pooling, transfer, and access across products and encoders [37], [39], [41], [57], [122], [147], [181]–[185]. Further work evaluates released embeddings in land-cover mapping, geographic and temporal transfer, environmental and socioeconomic prediction, retrieval, uncertainty analysis, and combinations of multiple representations [186]–[214].

B. Product Design Trade-offs

A global per-pixel layer contains many more vectors than a scene-level collection, while temporal or multisensor inputs place more observations into each vector than a single-image encoder. Dimensionality, resolution, and temporal support must therefore be interpreted together.

1) Dimensionality and Compression: Embedding dimensionality affects storage and the degrees of freedom available to encode variation. MOSAIKS [16] uses 8,192 random convolutional features, and Clay [22] uses a 1,024-dimensional vector learned through masked autoencoding [7]. Smaller vectors impose different constraints. AlphaEarth Foundations [14] maps observations to a 64-dimensional unit hypersphere, and the released Google Satellite Embedding dataset stores the resulting 64-dimensional vectors [15]. TESSERA v1 [21] uses Barlow Twins [108] to limit cross-dimensional redundancy in a 128-dimensional vector. TESSERA v2 [105] orders a 128-dimensional student representation so that 64-, 32-, and 16-dimensional prefixes can be used directly; the 16-dimensional prefix retains approximately 92% of the reported full-vector aggregate performance with one eighth of the storage. The released ESD tiles provide 13 values per pixel-year [57]. These dimensions are therefore not interchangeable measures of information content, and each must be evaluated on the intended downstream tasks.

Numeric precision provides a separate compression mechanism. Google Satellite Embedding stores 64 signed 8-bit values, or 64 bytes per vector, in Cloud-Optimized GeoTIFFs [14], [215]. TESSERA v1 [21] stores 128 signed 8-bit values and provides access through GeoTessera [216]. For a fixed dimension, either representation occupies one quarter of the value storage required by 32-bit floating point. Dimension and numeric precision should therefore be reported together.

Compression ratios depend on the reference data and the spatial and temporal support of one output. The 64-byte annual vectors in Google Satellite Embedding [14], [215] and the 128-byte annual vectors in TESSERA v1 [21] summarize different input archives, so neither implies a unique reduction relative to raw observations. TESSERA v2 changes vector storage through its 16–128-dimensional prefixes [105], whereas Clay's 1,024-dimensional 32-bit class token represents a 256×256-pixel scene [22]. ESD reports approximately $340\times$ compression specifically against its global daily Landsat–MODIS archive; the released annual product provides 13 values per pixel and occupies about 2.4 TB per year [57]. NeuCo-Bench instead evaluates representation size jointly with downstream utility [182], while model slimmability studies reduce encoder computation rather than the storage of a released embedding [217]. Compression claims are comparable only when the input baseline, output support, precision, and task protocol are stated.

2) Temporal Representation: Temporal design determines whether a vector describes one acquisition, summarizes an interval, or preserves an ordered sequence. Tile2Vec [76], MOSAIKS [16], and the DINOv2 [9] features distributed by Major TOM [20] encode individual images. SeCo uses observations from different seasons during pretraining, but its released image encoder still produces one vector from one image [100]; temporal supervision during training is therefore distinct from multi-date encoding at inference. Models that combine observations explicitly include AlphaEarth's time-conditioned annual summaries [14], SatMAE's temporal positional encoding [59], and Prithvi's three-dimensional patch embeddings [10]. TESSERA v1 samples annual optical and radar observations [21], while TESSERA v2 adds day-of-year encoding, attention pooling, and adaptive use of valid observations at inference [105]. ESD preserves within-year temporal information for every annual record from 2000 onward [57]. The appropriate design depends on whether the target follows phenology or rapid change [189], [218], or is sufficiently stable to be represented by a single-date or annual summary.

3) Multimodal Integration: Multimodal models differ in which sources they accept and where those sources interact. AlphaEarth is trained with optical, radar, LiDAR, environmental, topographic, and text observations; source-specific encoders feed a common spatiotemporal representation [14]. TESSERA v1 processes Sentinel-1 and Sentinel-2 time series in separate Transformer–GRU branches before concatenation and multilayer-perceptron fusion [21]. TESSERA v2 replaces this stage with modality-specific temporal Transformers followed by a fusion Transformer [105]. Clay supports several image modalities but processes an input according to its modality and conditions the encoder on location and time metadata [22]; support for several modalities does not necessarily mean that they are fused in one vector. Fusion can encode complementary measurements, but it also introduces requirements for co-registration, temporal alignment, and missing-source handling.

4) Spatial Support and Release Form: Spatial support determines both the smallest resolvable target and the number of vectors that must be distributed. SatCLIP [17] and GeoCLIP [18] return a vector for a coordinate without requiring a corresponding satellite image. MOSAIKS [16], Clay [22], and Major TOM Embeddings [20] operate at scene or tile level. Google Satellite Embedding [14], [15] and TESSERA v1 [21] release pixel-wise embeddings at 10 m resolution; TESSERA v2 is evaluated at the same spatial support [105], and ESD [57] operates at 30 m. A simple land-area calculation gives approximately 1.5×10^{12} cells for a global land grid at 10 m resolution. At 64 bytes per cell, this is about 96 TB before masking, tiling, compression, metadata, and projection overhead. Scene-level products require fewer vectors but cannot resolve variation within an input footprint. Parcel, administrative, and plot targets require aggregation chosen for their within-unit variation [184].

The release format determines who performs the encoding. Precomputed layers from Google Satellite Embedding [14], [15], TESSERA v1 [21], and ESD [57] remove user-side global inference. Clay v1.5 releases weights for encoding new inputs when its preprocessing is reproduced [22], while LGND distributes a separate vector collection generated with that encoder [23]. Copernicus-FM similarly provides a model, whereas Copernicus-Embed-025deg provides 768-dimensional vectors on a global 0.25° grid [60], [144]. Model weights permit new inputs and preprocessing choices but retain inference costs; released vectors are immediately usable but inherit the producer's input archive, masking, compositing, temporal definition, and encoder version. Temporal and multimodal inputs increase the information represented by each vector, while fine spatial support increases the number of vectors stored and queried. Product choice should follow target scale, temporal sensitivity, source availability, and acceptable compression loss.

C. Distribution Infrastructure

Earth embeddings are distributed through cloud services, public data repositories, spatial indexes, product-specific software, and model libraries. Hosting services store collections; spatial indexes relate vectors to geographic footprints and source imagery; product-specific software implements queries and decoding; and model libraries provide interfaces to multiple datasets or encoders. Table IV compares resources for publishing, accessing, and generating Earth embeddings.

Google Satellite Embedding can be analyzed server-side in Google Earth Engine or accessed as Cloud-Optimized GeoTIFF files in Google Cloud Storage [14], [15], [215]. The Copernicus Data Space Ecosystem publishes the Global Embeddings Dataset as GeoParquet files through EODATA S3 [219]. Hugging Face hosts Major TOM Core and embedding datasets [20], [220], while Source Cooperative provides catalog and object-storage access to LGND Clay Embeddings and Earth Index [23], [137], [221].

Data-organization tools, publication guidance, and product-specific clients do not host the same resources as cloud platforms. Major TOM defines a geographic grid and metadata conventions for organizing compatible EO datasets and their derived embeddings [19]. Geo-Embeddings provides recommendations for storing, documenting, and publishing gridded and irregular embedding collections, together with draft STAC and Zarr conventions that remain under development [224], [225]. GeoTessera is specific to TESSERA [21], [216], [226]: its versioned manifest indexes tiles, its client retrieves quantized NumPy arrays and scale factors from object storage, and its Zarr interface supports regional and point queries. It can also export georeferenced GeoTIFFs. Cloud-Optimized GeoTIFF, GeoParquet, NumPy, and Zarr provide different storage layouts, which affect how clients index, subset, and transfer embeddings.

Libraries for reusable encoders differ in breadth. TorchGeo [227], [228] provides geospatial dataset classes, spatial queries, and sampling for patch- and pixel-level embeddings, including Clay, Major TOM, Earth Index, Copernicus-Embed, TESSERA, Google Satellite Embedding, and ESD. TerraTorch is maintained within the TorchGeo organization and builds on TorchGeo and PyTorch Lightning to load, adapt, and extract embeddings from EO foundation models; it does not host precomputed global vectors [229]. RS-Embed [147], [148] uses one spatial and temporal query specification to retrieve selected precomputed products or run supported encoders on demand. GeoAI provides regional download, dequantization, comparison, and GeoTIFF export for Google Satellite Embedding; it also catalogs remote-sensing foundation models and loads supported backbones through TerraTorch [230]–[232]. AiTLAS [235], [236] provides model adapters, configuration, and task pipelines for EO models but does not itself publish a global precomputed embedding collection.

TorchSpatial implements 15 location encoders and LocBench in the same codebase [163]. SRAI combines vector-data acquisition, regionalization, and regional embedding methods for sources such as OpenStreetMap and Overture Maps [233], [234]. The LGND API exposes hosted Clay embedding collections, similarity search, and creation of new embedding collections from user-supplied imagery [22], [222], [223]. Catalog discovery, version tracking, spatial and temporal query, provenance, and cross-product composition remain divided among these interfaces.

D. Evaluation Benchmarks

Evaluation protocols determine which properties of an embedding are measured. Community benchmarks compare models using the same tasks, label budgets, and adaptation methods, but most were designed for foundation model adaptation rather than for precomputed vectors used as fixed geospatial data. Table V uses Cls, Seg, Reg, CD, OD, and IS for classification, semantic segmentation, regression, change detection, object detection, and instance segmentation, respectively; SDG denotes Sustainable Development Goal. The final "Sat. emb." column marks benchmarks designed specifically for fixed or precomputed satellite embeddings.

1) Task-Based Benchmarks: GEO-Bench [237] contains 6 classification and 6 semantic segmentation tasks and reports 20 baseline configurations, rather than 20 geospatial foundation models. Prithvi-EO 2.0 reports an 8% improvement over its predecessor under this protocol [10]. GEO-Bench does not include regression or change detection, while FoMo-Bench [239] adds 15 multimodal forest monitoring datasets spanning classification, segmentation, and object detection.

PANGAEA [183] adds regression and temporal inputs and evaluates 9 selected model entries, with SSL4EO-S12 represented by 4 variants, on 11 datasets for semantic segmentation, change detection, and regression. Its comparison with U-Net [243] and a standard Vision Transformer [98] shows that geospatial pretraining does not consistently outperform supervised models when labels are plentiful. GEO-Bench-2 [63] covers 19 datasets and 5 task types and reports normalized scores within capability groups. It uses TerraTorch [229] to apply a shared hyperparameter-search and repeated-seed protocol to 14 model configurations, including Clay [22], Prithvi [10], TerraMind [81], DOFA [13], DeCUR [109], SatlasPretrain [77], and DINOv3 [104]. The reported rankings vary by capability: natural-image ConvNeXt models [244] remain competitive for high-resolution RGB imagery and object detection, whereas EO pretraining is more useful for some multispectral and temporal tasks. Landsat-Bench [241] narrows the comparison to 3 Landsat classification benchmarks evaluated with nearest-neighbor classification [245] and linear probing. Model rankings must therefore be read together with the task, sensor, adaptation method, and amount of labeled training data.

Copernicus-Bench [60] contains 15 tasks using Sentinel-1, Sentinel-2, Sentinel-3, and Sentinel-5P data, organized into preprocessing, base applications, and specialized applications. PhilEO Bench [238] provides a 400 GB Sentinel-2

TABLE IV
INFRASTRUCTURE FOR PUBLISHING, ACCESSING, AND GENERATING EARTH EMBEDDINGS.

Infrastructure	Type	Primary function	Access / format	Representative resources	Link
Google Earth Engine and Cloud Storage [15], [215]	Cloud analysis and storage	Server-side analysis and direct access to annual embedding files	Earth Engine API; GCS / COG	Google Satellite Embedding [14]	↗
Copernicus Data Space Ecosystem [219]	Data hosting	Hosting and direct distribution of embedding collections	EODATA S3 / GeoParquet	Global Embeddings Dataset	↗
Hugging Face Hub [220]	Dataset repository	Versioned hosting and bulk distribution of EO datasets	Hub API / Parquet	Major TOM Core and embedding datasets [20]	↗
Source Cooperative [221]	Data publishing	Catalog and object access for public geospatial collections	HTTPS / S3; resource-specific formats	LGND Clay Embeddings [23]; Earth Index [137]	↗
LGND API [222], [223]	Hosted embedding service	Access, similarity search, and generation of embeddings from user imagery	REST API; bearer token; GeoParquet export	LGND Clay Embeddings and user-defined Clay collections [22], [23]	↗
Major TOM [19]	Data specification and tools	Shared geographic grid and metadata for compatible EO datasets	Python tools; grid and metadata schema	Major TOM Core and derived embedding collections [20]	↗
Geo-Embeddings [224], [225]	Conventions and registry	Guidance for storing, documenting, and publishing geospatial embeddings	Web documentation; draft STAC / Zarr conventions	Best practices, metadata templates, and implementation registry	↗
GeoTessera [216], [226]	Product client	Tile indexing, spatial query, dequantization, and export	Python / CLI; S3 / Zarr	TESSERA embeddings [21]	↗
TorchGeo [227], [228] TerraTorch [229]	Data and model toolkit	Geospatial data loading and sampling; foundation-model inference, embedding extraction, and adaptation	Python / PyPI; dataset API / CLI / YAML	Clay, Major TOM, Earth Index, TESSERA, Google Satellite Embedding, ESD, and EO foundation-model backbones [14], [20]–[22], [57], [137]	↗ ↗
RS-Embed [147], [148]	Embedding interface	Retrieval of precomputed vectors and on-demand encoder inference	Python / PyPI; Earth Engine / local inference	TESSERA, Google Satellite Embedding, Copernicus-Embed, and encoder adapters [14], [21], [60], [144]	↗
GeoAI [230]–[232]	Embedding and model toolkit	Download, analysis, and export of embeddings; discovery and loading of EO foundation models	Python / PyPI; COG / GeoTIFF; TerraTorch	Google Satellite Embedding and registered EO foundation models [14]	↗
TorchSpatial [163]	Location-embedding library	Implementation and evaluation of coordinate encoders	Python / source; PyTorch	Fifteen location encoders and LocBench	↗
SRAI [233], [234]	Regional-embedding framework	Data acquisition, regionalization, and embedding of vector geospatial data	Python / PyPI; OSM / Overture / H3	Count-based, contextual, and neural regional embeddings	↗
AiTLAS [235], [236]	Model integration toolkit	Model adapters, configuration, and task pipelines	Python / PyPI	AnySat, Copernicus-FM, CROMA, Galileo, Panopticon, Presto, and TerraMind [60], [62], [66], [81], [110], [112], [118]	↗

data set for land-cover classification, road segmentation, and building-density regression, using fixed decoders and label budgets. SustainFM [240] defines 16 tasks corresponding to Sustainable Development Goals 1–16 and extends evaluation to transferability, operational impact, and energy efficiency. REOBench [242] measures robustness across 6 tasks and 12 appearance-based or geometric image corruptions. Their protocols assess sensor dependence, transfer, efficiency, and robustness in addition to aggregate scores.

2) Evaluation of Fixed Embeddings: A benchmark for fixed embeddings evaluates precomputed satellite vectors rather than adapting the complete encoder. Using frozen features alone does not meet this definition. Landsat-Bench compares encoder outputs, and TorchSpatial / LocBench [163] evaluates 15 coordinate encoders on seven geo-aware image classification and ten image regression datasets. LocBench also introduces a Geo-Bias Score, but its inputs are locations rather than satellite embedding products.

Existing embedding benchmarks test compression, hidden tasks, and model selection. NeuCo-Bench [182] organizes five data groups spanning eight EO tasks and evaluates fixed-size representations with one evaluation pipeline, hidden test labels, and a score that combines predictive quality with stability. A subsequent study using NeuCo-Bench reports fixed representations more than 500$\times$ smaller than raw images and examines how pooling, normalization, and compression affect

TABLE V
COMMUNITY BENCHMARKS FOR GEOSPATIAL FOUNDATION MODELS AND EARTH OBSERVATION EMBEDDINGS.

Benchmark	**Year**	**Venue**	**Scope**	**Sat. emb.**
GEO-Bench [237]	2023	NeurIPS	12 tasks: 6 Cls, 6 Seg	
PhilEO Bench [238]	2024	IGARSS	Global Sentinel-2 data; Cls, Seg, Reg	
TorchSpatial / LocBench [163]	2024	NeurIPS	17 data sets: 7 Cls, 10 Reg	
FoMo-Bench [239]	2025	AAAI	15 data sets; Cls, Seg, OD	
PANGAEA [183]	2026	GRSM	11 data sets; Seg, CD, Reg	
Copernicus-Bench [60]	2025	ICCV	15 tasks using Sentinel-1, -2, -3, and -5P	
SustainFM [240]	2025	arXiv	16 tasks corresponding to SDGs 1–16	
GEO-Bench-2 [63]	2025	arXiv	19 data sets; Cls, Seg, Reg, OD, IS	
Landsat-Bench [241]	2025	ICMLW	3 Landsat benchmarks; Cls	
REOBench [242]	2025	NeurIPS	6 tasks; 12 corruption types	
NeuCo-Bench [182]	2026	CVPRW	5 data groups, 8 EO tasks; Cls, Reg	✓

downstream performance [246].

Embed2Scale and the TESSERA v2 scaling study examine representation size in different ways. The Embed2Scale Challenge [247] represents each image by a single 1,024-dimensional vector, reducing the number of scalar values by more than 7,000× relative to the source imagery; winning solutions fused features from several pretrained models [181], [248]. The TESSERA v2 study reports 395 training runs across 15 downstream tasks and finds that converged pretraining loss has a correlation below 0.2 in magnitude with aggregate downstream performance, while encoder capacity changes with training-data scale and projection-network size remains approximately fixed [105]. Downstream scores were more informative than pretraining loss within this model family; whether the result extends to other architectures, sensors, and objectives remains unknown.

3) Benchmark Results and Remaining Gaps: Benchmark results depend on the target and evaluation protocol. Temporal and multisensor representations such as AlphaEarth [14] and the TESSERA series [21], [105] are designed for targets that depend on seasonal or complementary sensor information. Dimension counts are comparable only with matched spatial support, inputs, and adaptation protocols. PANGAEA [183] evaluates models with 10%, 50%, and 100% of the labeled training data and finds that supervised baselines remain competitive on several tasks, with the relative benefit of pretraining depending on the task and label budget. Benchmark reports should therefore state the adaptation method, amount of labeled training data, input data, and target.

Geographic and temporal transfer remain weakly measured. PANGAEA, SustainFM, and GEO-Bench-2 include more regions [63], [183], [240], but regional and environmental coverage remains uneven. A 2026 agricultural benchmark [249] evaluates Prithvi [10], SpectralGPT [11], and SatMAE [59] on multitemporal crop segmentation and change detection across four U.S. states; region-separated splits report lower performance under geographic transfer. The result supports region-separated evaluation. Annual products also require tests across years and in regions undergoing rapid land-cover change. Cross-model scores are further confounded by differences in source imagery and preprocessing. Major TOM [19], [20] applies several encoders to the same tiles, while Earth Embeddings as Products [37] provides standardized TorchGeo loaders [227]. Geographic and temporal transfer should also be tested with identical source inputs.

Aggregate benchmark scores often rely on thousands of labeled pixels or patches, whereas many field studies have far fewer observations [183]. Reporting performance across several labeled training-set sizes would characterize applications with limited labels more directly. Task composition introduces a second mismatch. Classification and segmentation dominate, while regression of biomass, canopy height, and yield, multi-year change detection, retrieval, and out-of-distribution generalization remain less common. Class separation does not guarantee that an embedding preserves the smooth variation required for continuous prediction. Current benchmarks also do not determine whether year-to-year distances distinguish gradual environmental change from sensor or preprocessing artifacts. GEO-Bench-2 [63] includes regression, and Embed2Scale [247] evaluates compression, but no benchmark combines continuous variables, temporal transfer, retrieval, and fixed label budgets in one protocol for fixed embeddings.

IV. EXPERIMENTS

The experiments examine how Earth embeddings organize the same geographically distributed samples and how well they support prediction of discrete and continuous land-surface properties. We first compare global and local structure using Uniform Manifold Approximation and Projection (UMAP) [250], linear centered kernel alignment (CKA) [251], and cosine-neighborhood overlap. We then evaluate land-cover classification, continuous-variable regression, and the sensitivity of predictive performance to embedding dimension.

A. Data

Fig. 6 shows the 9,132 candidate locations distributed across terrestrial land areas. Each location defines a $640\,\mathrm{m} \times 640\,\mathrm{m}$ patch and is associated with one of the 11 ESA WorldCover 2021 v200 reference classes [252]; these labels are used only to color descriptive visualizations.

The inputs comprise reflectance from 3 observation sources and 7 learned embeddings. The observation sources are Sentinel-2 [44], Landsat [2], and MODIS [64]. The learned inputs are ESD [57], Google Satellite Embedding (GSE) [14], [15], AgriFM [253], Copernicus-FM [60], TESSERA [21],

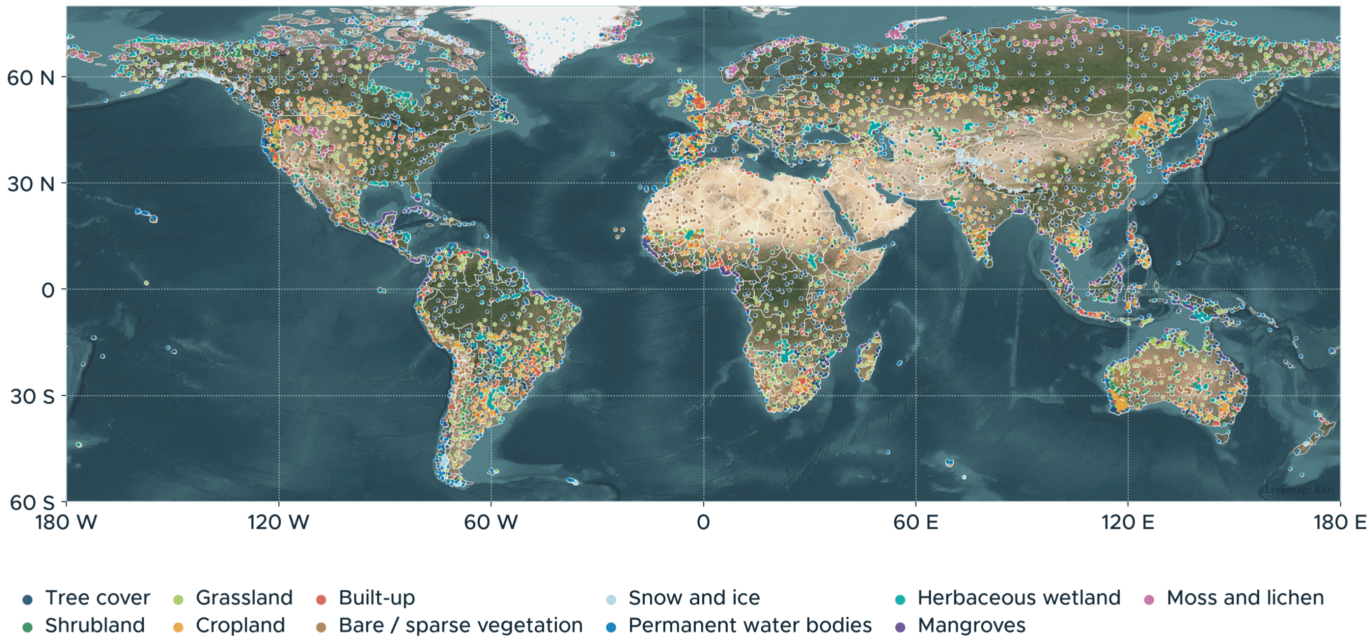

Fig. 6. Global distribution and WorldCover classes of the evaluation samples.

TerraMind [81], and WildSAT [254]. Representation-space and predictive comparisons use all 10 inputs, and the UMAP projection also includes their concatenation.

The classification targets are the Esri annual land-use and land-cover product at $10\,\mathrm{m}$ resolution [255], FROM-GLC10 2017 [256], and ESA WorldCover 2021 v200 [252]. The continuous targets are elevation from Copernicus GLO-30 [50], above-ground biomass from the ESA Climate Change Initiative [257], and Meta global canopy height [258]. These datasets cover discrete surface types and continuous variables with different units, spatial patterns, and class or value distributions.

B. Internal Representation Analysis

The internal comparison does not use a downstream target. UMAP provides a qualitative view of local organization, while linear CKA and neighborhood overlap measure global geometric similarity and local retrieval consistency. All inputs undergo the same preprocessing before comparison.

1) Low-Dimensional Structure: Let $X^{(s)} \in \mathbb{R}^{n \times d_s}$ denote the processed matrix for input s, where rows correspond to the same locations and d_s may differ across inputs. Spatial features were mean pooled, ℓ_2 normalized, winsorized at the 1^{st} and 99^{th} percentiles, and scaled by the median and interquartile range. Land-cover labels color the projected points but do not enter the UMAP fit or any quantitative metric.

In Fig. 7, the aligned locations have different local arrangements across sources. The three reflectance inputs form broad, continuous manifolds, although their shapes are not identical, and ESD [57] has a similarly diffuse organization. GSE [14], [15], Copernicus-FM [60], and TESSERA [21] divide the samples into more fragmented local components, whereas AgriFM [253], TerraMind [81], and WildSAT [254] produce elongated structures with several class-dominated regions. The concatenated representation has a compact, multi-branch organization that does not reproduce any single input space, so concatenation changes the projected neighborhoods rather than merely enlarging one of the component manifolds.

No projection uniformly separates all land-cover classes. Some regions are dominated by a single class, but spectrally or structurally related surfaces still overlap. The UMAP panels are descriptive: coordinates, orientation, and distances are not comparable across independently fitted panels, and visual separation is not a quantitative clustering or prediction score. Linear CKA and neighborhood overlap provide pairwise comparisons of global geometry and local retrieval behavior.

2) Global Geometry and Local Neighborhoods: Linear CKA compares global representation geometry. For row-normalized and column-centered matrices X and Y, linear CKA is

$$\mathrm{CKA}(X, Y) = \frac{\|X^{\mathsf{T}} Y\|_F^2}{\|X^{\mathsf{T}} X\|_F \, \|Y^{\mathsf{T}} Y\|_F}. \tag{9}$$

CKA is invariant to orthogonal transformations and isotropic rescaling, allowing sources with different feature dimensions to be compared. A high value indicates similar centered linear geometry, not identical vectors or identical nearest-neighbor rankings.

Local agreement is measured directly from cosine neighborhoods. Let $\mathcal{N}_k^X(i)$ be the k nearest neighbors of location i in representation X under cosine distance. The overlap between two representations is

$$O_k(X, Y) = \frac{1}{n} \sum_{i=1}^{n} \frac{\left|\mathcal{N}_k^X(i) \cap \mathcal{N}_k^Y(i)\right|}{k}. \tag{10}$$

The score lies between zero and one and measures whether the same locations would be retrieved locally in both spaces. We evaluate k from 5 to 200; the value printed in each matrix cell

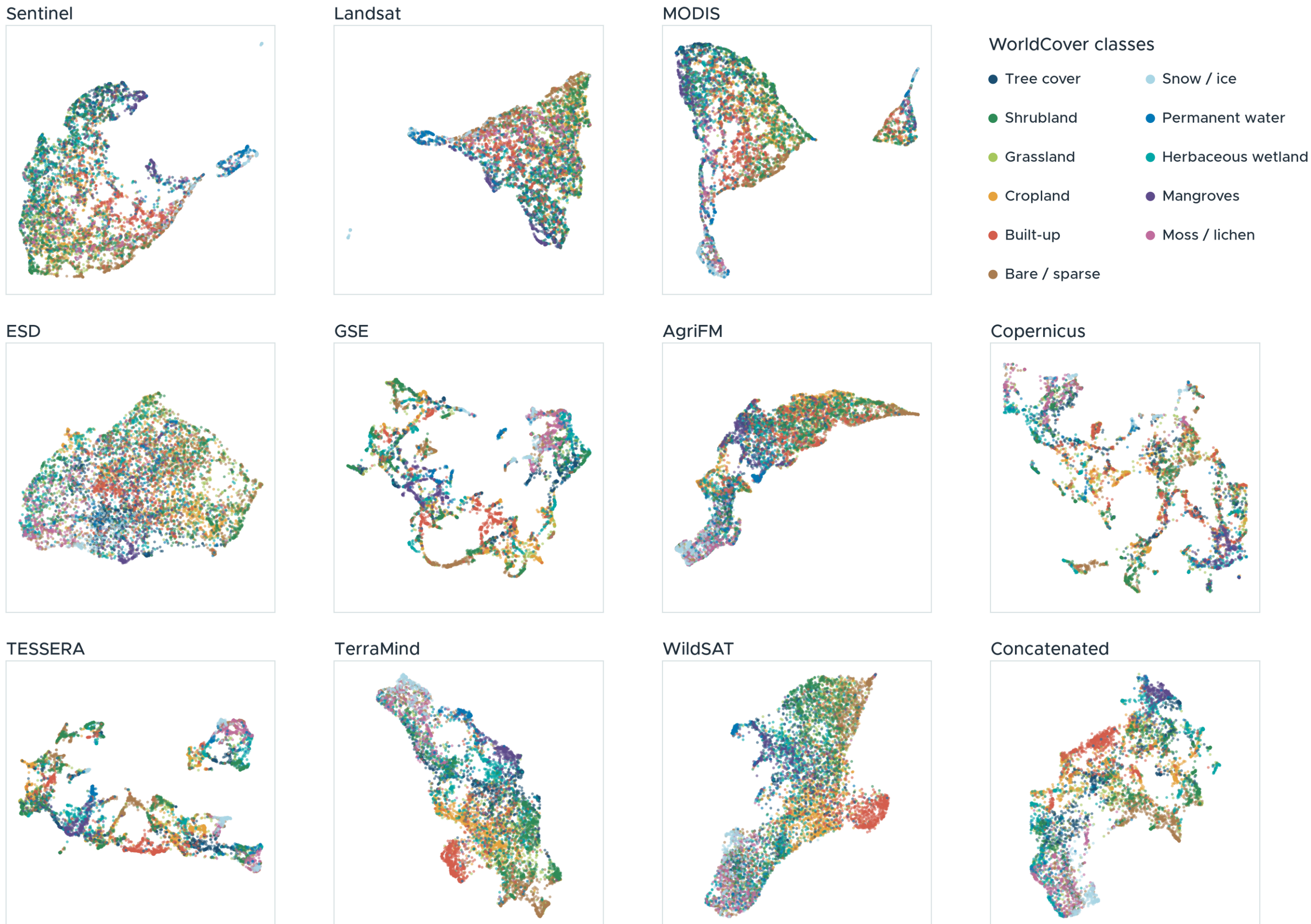

Fig. 7. UMAP projections of the aligned feature sources, colored by WorldCover class.

is the mean across these neighborhood sizes. The figures report cosine-based results, and Euclidean-distance counterparts provide a sensitivity check. Both pairwise matrices are symmetric, so Fig. 8 shows only the lower triangle. Each neighborhood-overlap cell reports the change across the evaluated values of k on a common scale.

Fig. 8(a) shows two groups with relatively high global similarity. Among the reflectance inputs, Sentinel and Landsat are the closest pair (0.728), followed by Sentinel and MODIS (0.489), consistent with shared optical measurements but different spatial and temporal support. Among the learned representations, GSE [14], [15] and TESSERA [21] have the highest CKA (0.614). TerraMind [81] also has comparatively high CKA with WildSAT [254] (0.566), AgriFM [253] (0.534), TESSERA (0.519), and GSE (0.507). By contrast, CKA between Copernicus-FM [60] or ESD [57] and the reflectance inputs is only 0.135–0.203. These values describe linear geometry, not predictive quality or complementarity.

The local-overlap ranking in Fig. 8(b) is related but not identical. GSE and TESSERA again form the closest pair, with a mean overlap of 0.474 across the evaluated neighborhood sizes. TESSERA–TerraMind (0.318), GSE–TerraMind (0.303), and GSE–Copernicus-FM (0.281) form the next strongest learned-representation relations. For GSE and TESSERA, overlap rises from 0.381 at $k = 5$ to 0.503 at $k = 200$, so the pair shares both small and broader neighborhoods. The increase with k is partly mechanical because larger neighborhoods offer more opportunities for intersection; comparisons among pairs at the same k are more informative than the increase alone.

Global and local agreement are nevertheless not interchangeable. Sentinel and Landsat have the highest CKA, yet their mean neighborhood overlap is only 0.222 and increases from 0.076 at $k = 5$ to 0.294 at $k = 200$. Their representations therefore share strong large-scale linear structure while differing more substantially in the identities of the nearest locations. The Euclidean sensitivity check preserves GSE–TESSERA and the TerraMind-centered learned group among the strongest relations, but changes the prominence of the raw-sensor pairs. CKA and neighborhood overlap identify related spaces but do not measure task utility. The following classification and regression experiments compare the target information available to the evaluated prediction models.

C. Downstream Predictive Performance

The downstream experiments use common data splits and prediction models to compare discrete land-cover classification

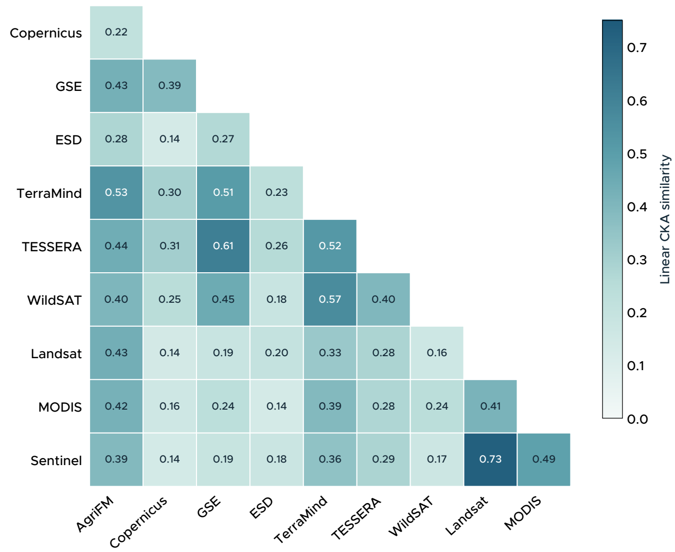

(a) Linear CKA similarity.

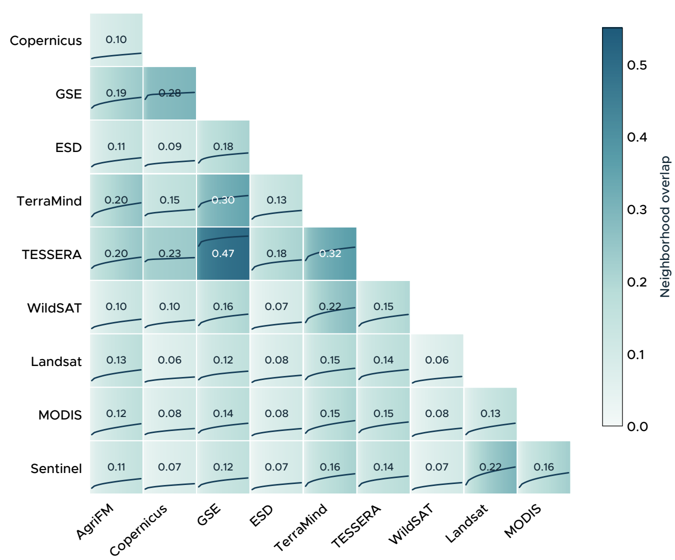

(b) Cosine-neighborhood overlap.

Fig. 8. Pairwise similarity between feature spaces measured by linear CKA and cosine-neighborhood overlap.

and continuous-variable regression. Performance is reported by target and metric, followed by sensitivity to embedding dimension and variation across prediction models.

1) Experimental Design: Within each target, every input uses the same sampled locations and a fixed partition containing 70% training data and 30% held-out test data. Classification is stratified by class, whereas regression is split without target stratification. We evaluate 14 prediction models for each task. Linear and local methods comprise a learned linear head, k-nearest neighbors [245], a linear support vector classifier or regressor [90], logistic regression [259] for classification, and ridge regression [260] for regression. Tree ensembles comprise random forest [89], gradient boosting and histogram gradient boosting [261], XGBoost [262], LightGBM [263], and CatBoost [264]. The neural predictors are a multilayer perceptron (MLP) [265], a convolutional neural network (CNN) [266], a long short-term memory network (LSTM) [97], and a Vision Transformer (ViT) [98]. The MLP is the scikit-learn implementation [267]; the linear head, CNN, LSTM, and ViT are trained in PyTorch [268].

Hyperparameters are selected by fivefold cross-validation within the training partition. Where supported by the predictor, classification uses class-balanced sample or loss weights; regression targets are standardized using training-partition statistics and transformed back before evaluation. For scikit-learn predictors [267], each input is normalized per channel, flattened, and reduced by incremental principal component analysis (PCA) [269] fitted only on the corresponding training fold. The PyTorch predictors [268] instead consume the harmonized spatial tensors and preserve their channel and spatial organization. After hyperparameter selection, each predictor is refitted on the full training partition and evaluated on the held-out test partition.

2) Evaluation Measures: Let n be the number of test samples, C the number of classes, and $\mathbf{s}_i$ the class-score vector for sample i. Classification is summarized by accuracy, macro-F1, and top-3 accuracy:

$$\text{Accuracy} = \frac{1}{n}\sum_{i=1}^{n} \mathbb{I}(\hat{y}_i = y_i), \tag{11}$$

$$P_c = \frac{TP_c}{TP_c + FP_c}, \tag{12}$$

$$R_c = \frac{TP_c}{TP_c + FN_c}, \tag{13}$$

$$\text{MacroF1} = \frac{1}{C}\sum_{c=1}^{C} \frac{2P_cR_c}{P_c + R_c}, \tag{14}$$

$$\text{Top3} = \frac{1}{n}\sum_{i=1}^{n} \mathbb{I}(y_i \in \mathcal{T}_3(\mathbf{s}_i))\,. \tag{15}$$

where $\mathcal{T}_3(\mathbf{s}_i)$ contains the three highest-scoring classes. Macro-F1 weights classes equally and is therefore the primary measure for imbalanced land-cover targets. Accuracy weights samples equally, while top-3 accuracy measures whether the reference class remains among the most plausible alternatives.

For continuous targets, we report the coefficient of determination (R^2) and root-mean-square error (RMSE) normalized by the test-target standard deviation. The latter is reported as normalized root-mean-square error (NRMSE):

$$\text{RMSE} = \sqrt{\frac{1}{n}\sum_{i=1}^{n}(y_i - \hat{y}_i)^2}, \tag{16}$$

$$R^2 = 1 - \frac{\sum_{i=1}^{n}(y_i - \hat{y}_i)^2}{\sum_{i=1}^{n}(y_i - \bar{y})^2}, \tag{17}$$

$$\text{NRMSE} = \frac{\text{RMSE}}{\sigma}. \tag{18}$$

Higher values are better for the three classification measures and R^2; lower values are better for NRMSE. Here, σ is the standard deviation of the test targets. Normalization by σ permits comparison across elevation, biomass, and canopy

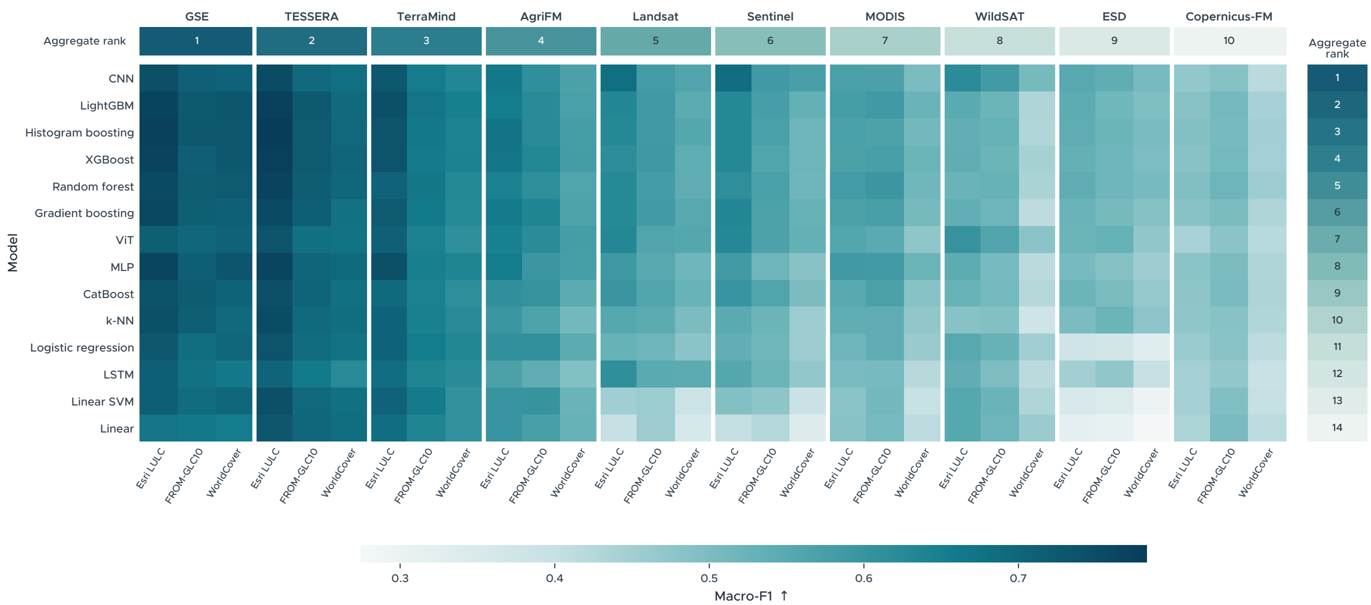

Fig. 9. Macro-F1 across prediction models, embeddings, and land-cover datasets.

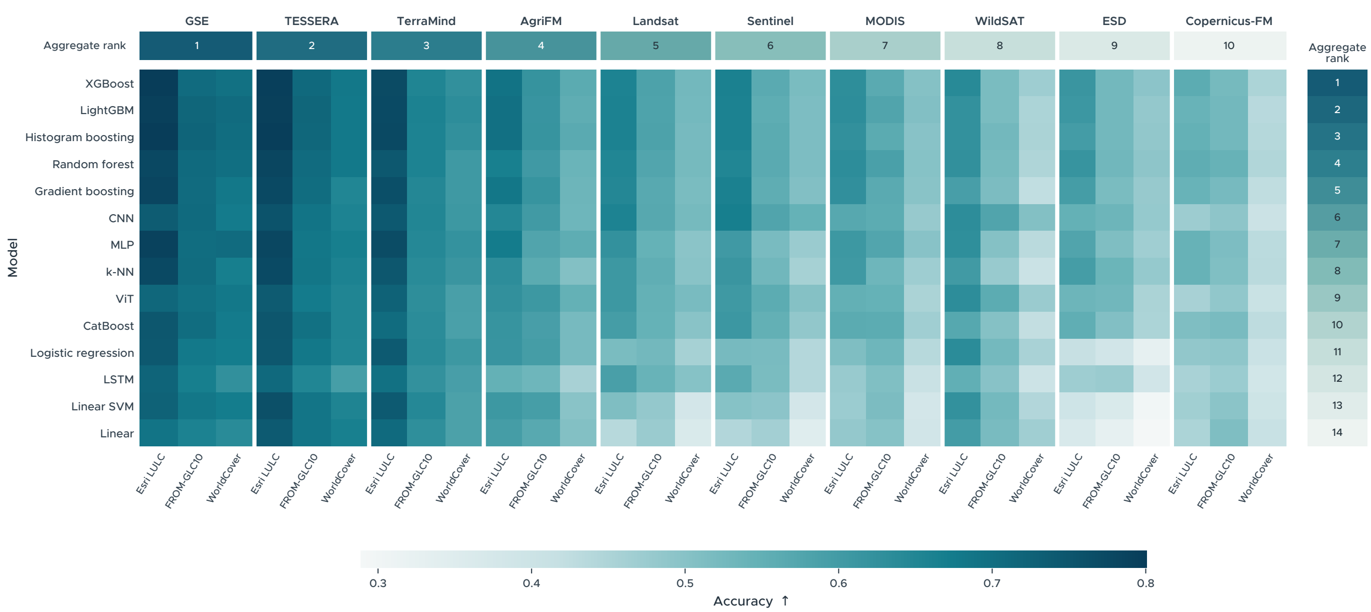

Fig. 10. Accuracy across prediction models, embeddings, and land-cover datasets.

height without conflating predictive error with their physical scales. In the heatmaps, aggregate ranks are obtained by ordering the mean score across the evaluated embeddings and datasets. In the forest summaries, points are means across prediction models and intervals span the corresponding interquartile range.

3) Land-Cover Classification: Figs. 9–11 report macro-F1, accuracy, and top-3 accuracy, respectively. Rows identify prediction models, grouped columns identify embeddings, and the cells within each group correspond to Esri LULC, FROM-GLC10, and WorldCover. The macro-F1 heatmap in Fig. 9 gives mean values of 0.718 for GSE [14], [15], 0.712 for TESSERA [21], and 0.666 for TerraMind [81] across the evaluated models and datasets. TESSERA is strongest on Esri LULC, whereas GSE leads on FROM-GLC10 and WorldCover; TerraMind ranks third on each dataset. AgriFM [253] follows at 0.596, while the remaining learned inputs, WildSAT [254], ESD [57], and Copernicus-FM [60], obtain lower means. The ordering is broadly stable across predictors, but the size of the difference depends on the prediction model. Nonlinear and boosting methods often narrow the differences among inputs, whereas linear predictors produce larger separations.

Accuracy in Fig. 10 gives nearly the same embedding ordering but places less weight on minority-class performance. GSE averages 0.711, TESSERA 0.705, and TerraMind 0.664, compared with 0.588 for AgriFM. At the predictor level,

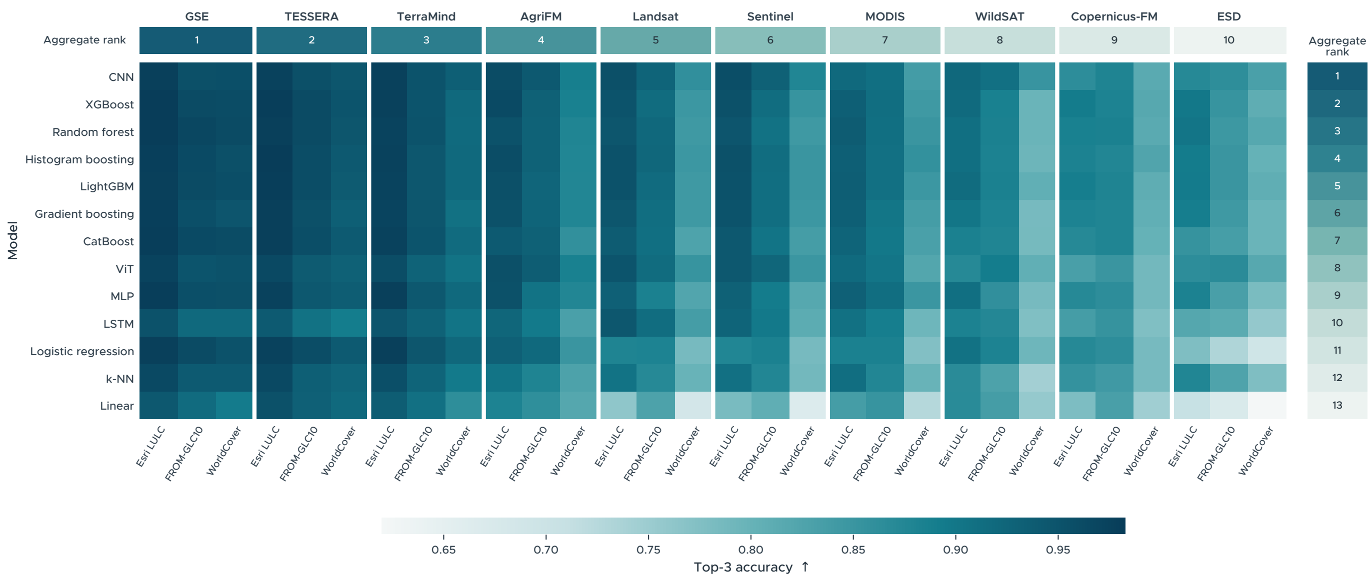

Fig. 11. Top-3 accuracy across prediction models, embeddings, and land-cover datasets.

XGBoost, LightGBM, histogram gradient boosting, and random forest form a close group, while the CNN attains the highest average macro-F1. Macro-F1 reveals class imbalance that accuracy can mask.

Top-3 accuracy in Fig. 11 is more compressed across embeddings. GSE, TESSERA, and TerraMind reach mean values of 0.958, 0.951, and 0.940, respectively, and AgriFM reaches 0.907. The observation inputs also improve substantially under this criterion. The correct class often remains among the top three predictions, but macro-F1 remains the main measure for imbalanced classification.

Class-specific behavior is examined after selecting hyperparameters for each embedding and predictor by macro-F1 within the training folds. The corresponding test-set confusion matrix is normalized within reference classes, after which the 14 matrices are averaged with equal model weights. The percentages in Figs. 12–14 therefore measure mean class recall and mean error allocation across predictors; they are not obtained by pooling predictions or constructing an ensemble.

For Esri LULC, Fig. 12 confirms that GSE and TESSERA retain the most balanced diagonal structure, with mean diagonal recalls of 77.1% and 77.7%; TerraMind follows at 73.4%. Their main errors concern flooded vegetation and bare ground being assigned to rangeland. The lower-scoring inputs show more class-dependent behavior: WildSAT is strong for crops and built areas but reaches only 30.7% for flooded vegetation, while the mean diagonal recalls of Copernicus-FM and ESD are close to 52%. The observation inputs preserve water, trees, and snow more reliably than flooded vegetation or crops.

The FROM-GLC10 matrices in Fig. 13 give GSE, TESSERA, and TerraMind mean diagonal recalls of 72.7%, 72.2%, and 67.8%, respectively. Cropland is most often confused with grassland, and grassland with shrubland; snow and ice are frequently assigned to bare land. These directions recur across learned embeddings and observation inputs. The embeddings differ mainly in error rates, not confusion types.

WorldCover in Fig. 14 is more difficult for the lower-scoring embeddings. GSE and TESSERA maintain mean diagonal recalls above 71%, and TerraMind reaches 66.4%, but shrubland and grassland remain difficult to separate. Moss and lichen have lower recall than spectrally distinctive classes such as built-up land and snow or ice. Wetlands are often assigned to tree cover by the observation inputs, while WildSAT also confuses mangroves with tree cover. The class-level results explain why similar overall accuracy can conceal different class-specific errors.

4) Continuous-Variable Regression: Figs. 15 and 16 report R^2 and NRMSE for Copernicus DEM elevation, ESA Climate Change Initiative above-ground biomass, and Meta canopy height. The R^2 heatmap in Fig. 15 shows stronger task dependence than the classification results. Across the three targets, GSE [14], [15] has the highest aggregate mean R^2 at 0.738, followed by TESSERA [21] at 0.612, TerraMind [81] at 0.609, and Copernicus-FM [60] at 0.519. The aggregate values conceal a marked target difference: Copernicus-FM records the highest mean for elevation (0.926), slightly above GSE (0.918), whereas GSE leads for biomass and canopy height. The high elevation score is expected because Copernicus-FM was pretrained on Copernicus GLO-30 DEM and the released Copernicus embedding therefore retains information derived from the same product used as the regression target [60]. TerraMind is second on both vegetation targets, while the other inputs have aggregate means between 0.30 and 0.36. CNN and ViT provide the strongest predictor-level averages, consistent with nonlinear interactions being useful for the continuous targets.

NRMSE in Fig. 16 gives the same aggregate ordering on a standardized error scale. GSE obtains the lowest mean NRMSE (0.476), followed by TESSERA (0.601), TerraMind (0.623), and Copernicus-FM (0.640); the remaining inputs range from 0.796 to 0.832. NRMSE permits comparison across elevation, biomass, and canopy height despite their different

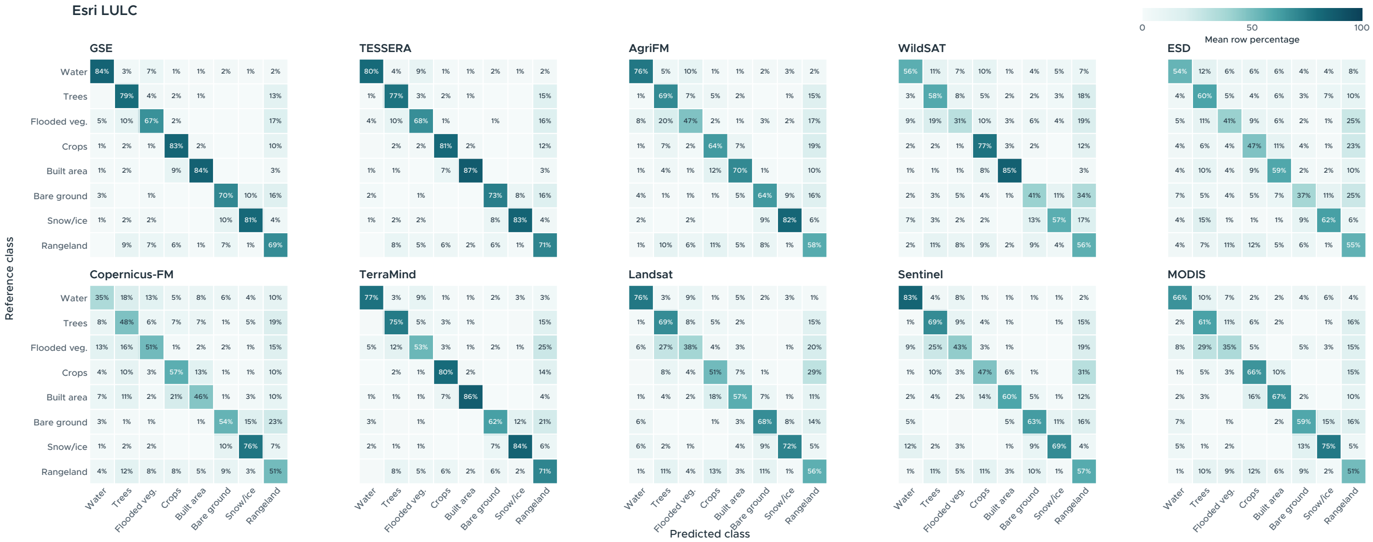

Fig. 12. Model-averaged class confusion for Esri LULC.

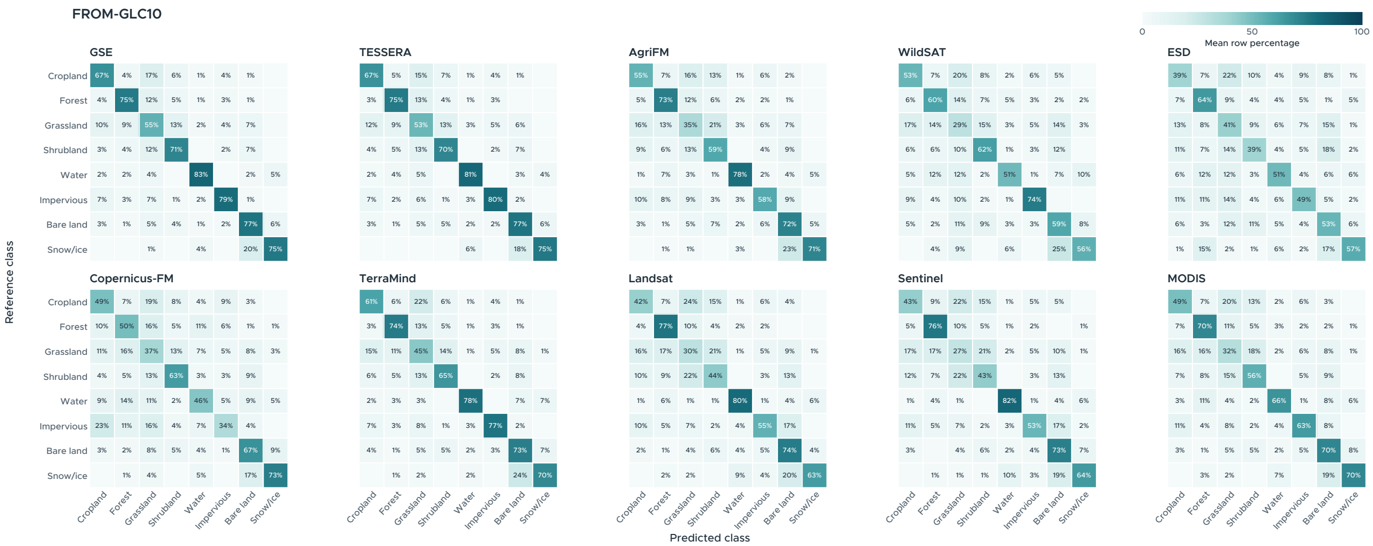

Fig. 13. Model-averaged class confusion for FROM-GLC10.

physical scales.

The binned regression curves use hyperparameters selected within the training folds. For each embedding and target, test observations are divided into 15 ordered bins and predictions are averaged within each bin for each of the 14 predictors. The plotted line is the mean of these model-specific bin means, and the shaded band is their interquartile range. Zero canopy height forms a separate bin before the positive observations are divided into 14 equal-frequency groups. The displayed R^2 is the mean of the 14 model-level scores, rather than the score of an averaged prediction.

Fig. 17 shows the strongest separation among embeddings. Copernicus-FM and GSE follow the 1:1 line over most of the elevation range and have mean R^2 values of 0.925 and 0.919, respectively. TESSERA reaches 0.706 and TerraMind 0.643, with both increasingly underestimating the highest elevations. The other inputs flatten substantially above approximately 1,000 m. Their relatively narrow interquartile bands indicate that this attenuation is shared by several predictors rather than caused by a single model.

Above-ground biomass in Fig. 18 is less accurately recovered than elevation. GSE has the highest mean R^2 (0.658), followed by TerraMind (0.596), TESSERA (0.572), and ESD [57] (0.494). All embeddings are closer to the reference line at low biomass and increasingly underestimate high-biomass locations. The widening bands at the upper end also show that predictor choice matters more where observations are sparse and the target range is large.

The canopy-height curves in Fig. 19 show a similar but weaker ordering. GSE, TerraMind, and TESSERA obtain mean R^2 values of 0.637, 0.578, and 0.547, respectively, while the other inputs range from 0.235 to 0.433. Predictions are close to the reference line for low vegetation, but all curves fall below it as canopy height increases. The explicit zero-

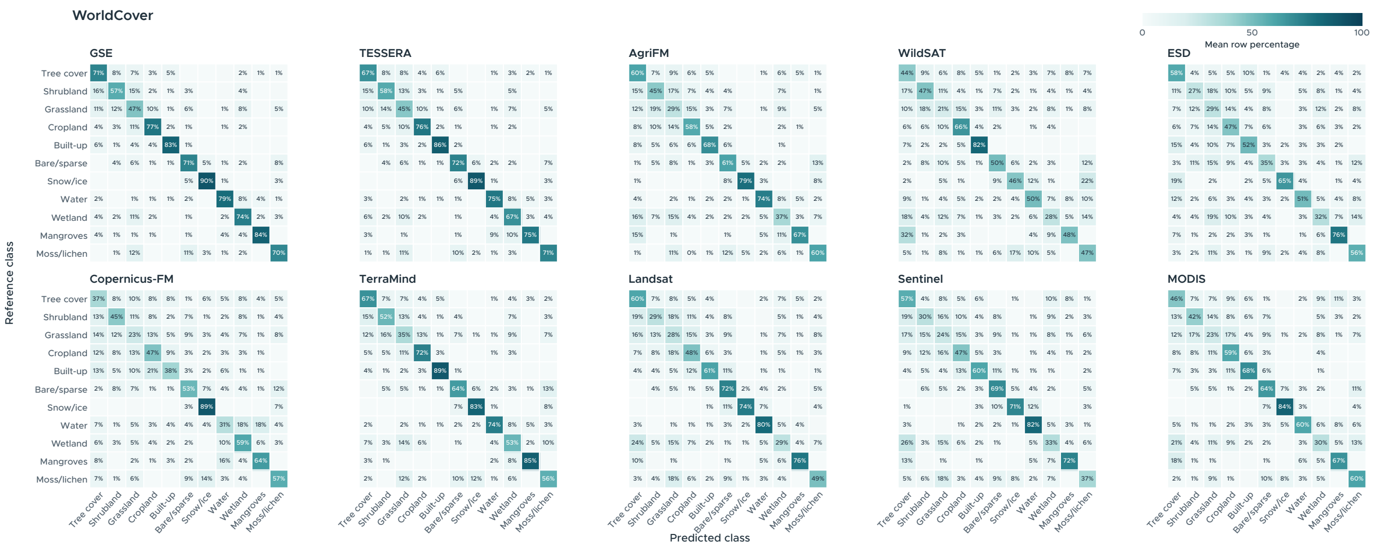

Fig. 14. Model-averaged class confusion for WorldCover.

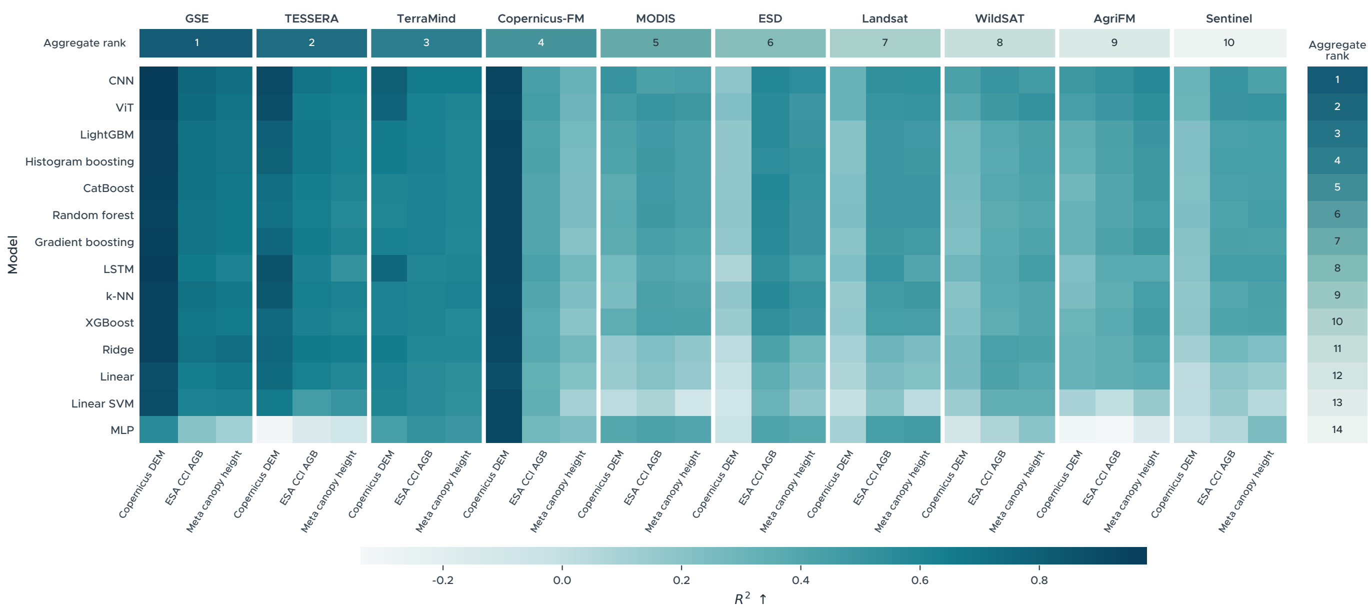

Fig. 15. Coefficient of determination across prediction models, embeddings, and continuous-variable datasets.

height bin separates performance on non-vegetated samples from the positive-height trend.

5) Dimensionality and Pareto Efficiency: Each input at a sampled location is represented as a tensor $\mathbf{X} \in \mathbb{R}^{H\times W\times C}$, where H and W are the spatial dimensions and C is the number of feature channels. For the dimensionality analysis, the normalized tensor is flattened and reduced by Incremental PCA to $d \in \{8, 16, 32, 64, 128, 256, 512, 1024\}$. Thus, d denotes the length of the reduced flattened vector, rather than the channel count of the original tensor. Figs. 20 and 21 show the complete sweep rather than selecting one dimension. For score $q_{r,p,d}$ obtained by representation r, predictor p, and dimension d, the two plotted summaries are

$$\bar{q}_{r,d} = \frac{1}{|\mathcal{P}_{r,d}|} \sum_{p\in\mathcal{P}_{r,d}} q_{r,p,d}, \tag{19}$$

$$\bar{q}_{p,d} = \frac{1}{|\mathcal{R}_{p,d}|} \sum_{r\in\mathcal{R}_{p,d}} q_{r,p,d}. \tag{20}$$

The first average compares representations over the evaluated predictors, and the second compares predictors over the evaluated representations. A point is Pareto efficient when no point at an equal or lower dimension achieves an equal or better score, with the performance inequality reversed for NRMSE.

The embedding profiles show that most gains occur at the lower end of the dimension sweep. Across the classification datasets, the best macro-F1, accuracy, and top-3 results occur between 32 and 128 dimensions. GSE [14], [15] supplies the

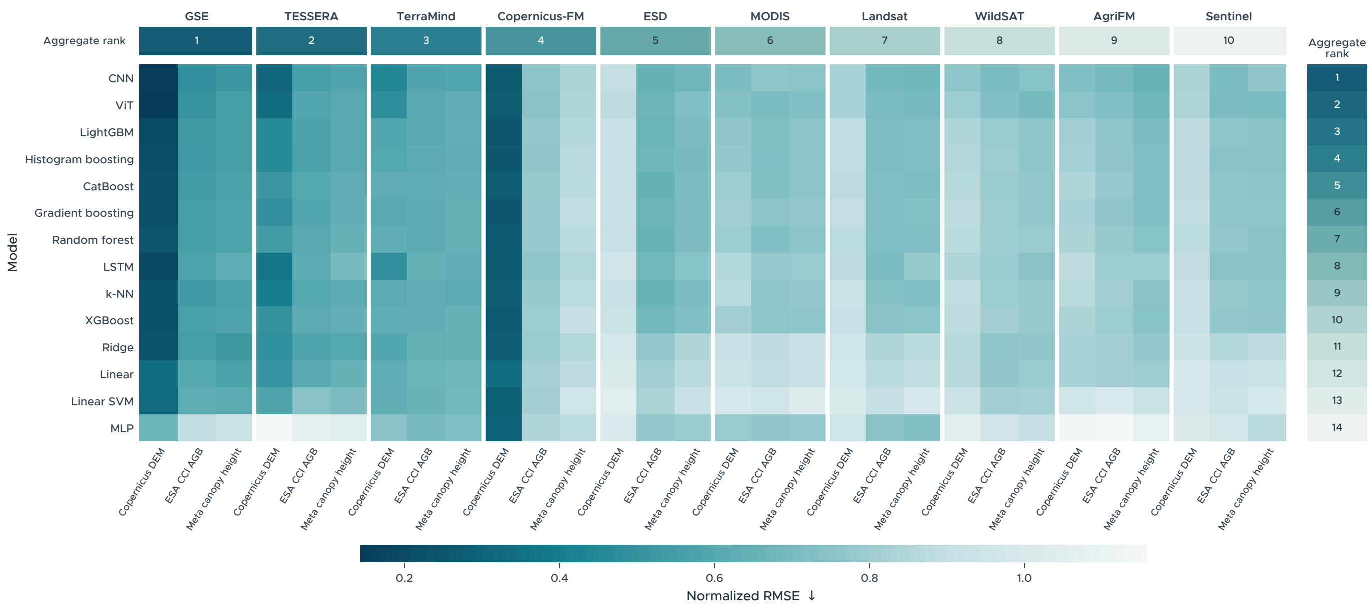

Fig. 16. Normalized RMSE across prediction models, embeddings, and continuous-variable datasets.

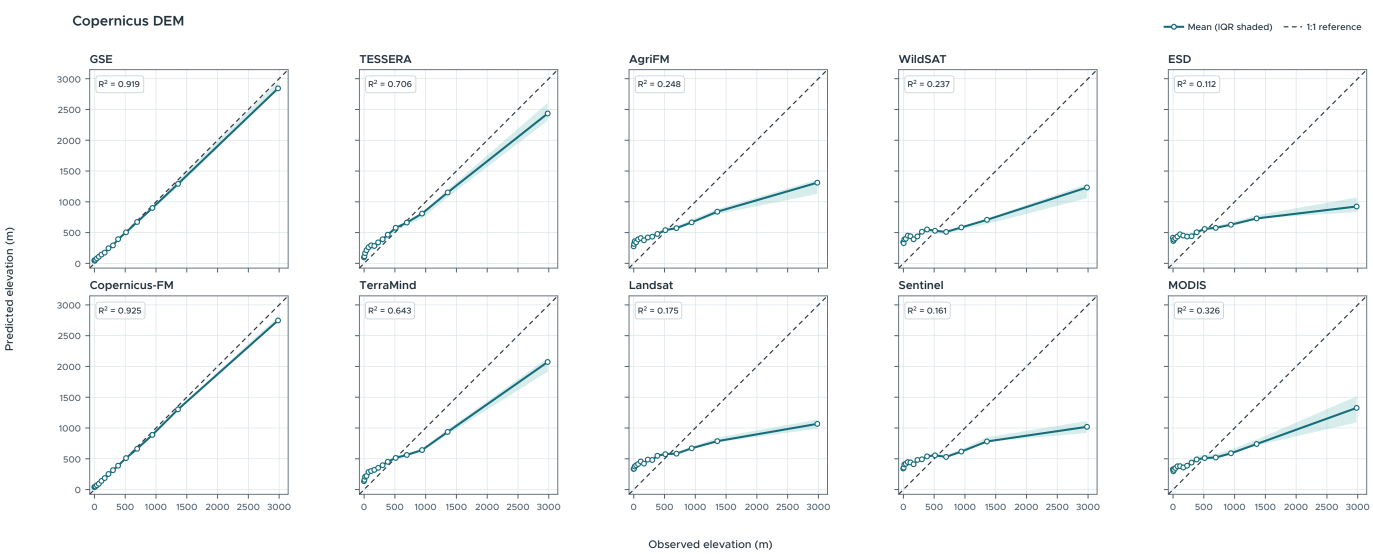

Fig. 17. Model-averaged regression for Copernicus DEM elevation.

global optimum in all but one of the 15 dataset–metric comparisons: TESSERA [21] reaches the highest Esri-LULC macro-F1 (0.754) at 128 dimensions, while GSE leads the remaining classification metrics and all 6 regression comparisons. Elevation and above-ground biomass peak at 64 dimensions for GSE, with R^2 values of 0.942 and 0.686. Canopy height is the main exception to early saturation and improves to $R^2 = 0.665$ at 512 dimensions. Higher dimensions improve some tasks but not others.

The predictor profiles reach a similar conclusion. Their global optima occur between 32 and 128 dimensions: histogram gradient boosting, LightGBM, and XGBoost account for most of the best-performing combinations, while random forest is optimal for WorldCover top-3 accuracy at 32 dimensions. Embedding rankings change with the predictor and dimension.

6) Performance Across Models and Embeddings: Across the 5 metrics, GSE [14], [15], TESSERA [21], and TerraMind [81] perform consistently well on the discrete and continuous targets evaluated here, but their ordering and the differences among other inputs vary by target and predictor. Copernicus-FM [60] illustrates this task dependence by combining the strongest elevation result with substantially lower classification, biomass, and canopy-height scores. Learned embeddings do not uniformly outperform the observation inputs: Landsat [2], Sentinel-2 [44], and MODIS [64] remain competitive with several learned embeddings, particularly for classification. Downstream rankings also differ from the pairwise geometric relations because CKA and neighborhood overlap measure similarity between feature spaces, whereas

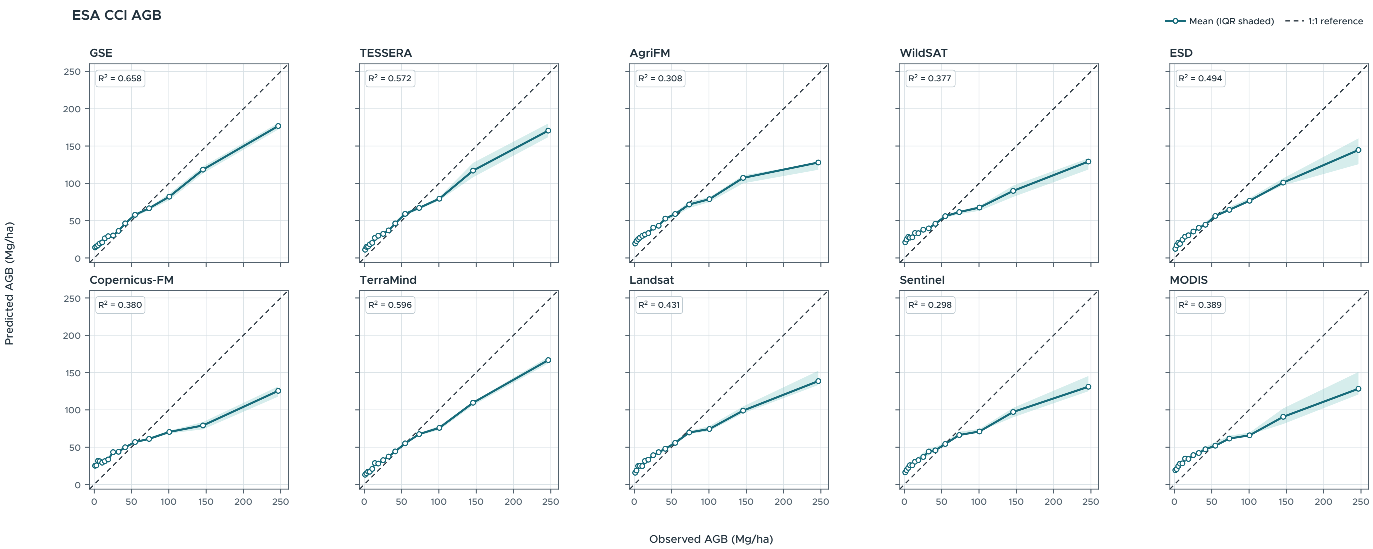

Fig. 18. Model-averaged regression for ESA CCI above-ground biomass.

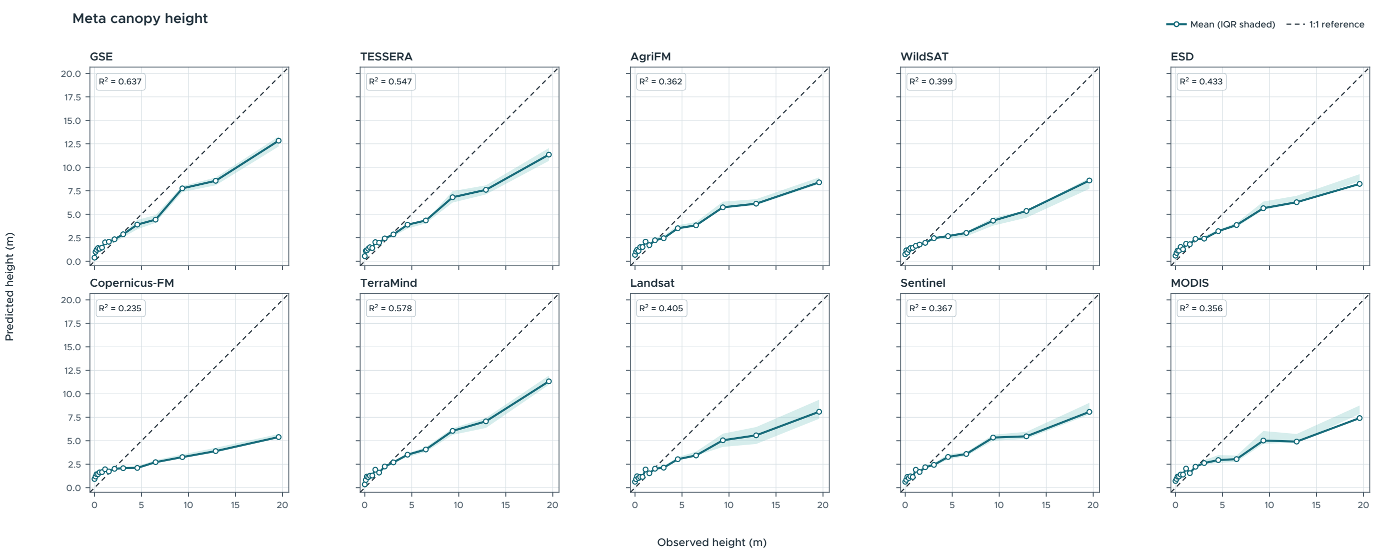

Fig. 19. Model-averaged regression for Meta canopy height.

the predictive experiments measure task performance.

V. Applications

Earth embeddings have been used for agriculture, ecological monitoring, biophysical estimation, environmental mapping, retrieval, and socioeconomic prediction. Fig. 23 summarizes these domains, and Fig. 24 links the evaluated embeddings to their reported downstream uses.

A. Agriculture and Ecology

Agricultural and ecological applications include crop and forest mapping, biomass estimation, vegetation monitoring, and biodiversity assessment [270]–[290]. They use either released embedding layers or features extracted from reusable encoders, with representations frozen, pooled, or adapted before prediction. Recent ecological mapping experiments also apply Prithvi-EO 2.0 and TerraMind to land-cover generation, forest functional-trait mapping, and peatland detection [291].

Several studies report gains when few labeled samples are available, but the best representation varies by region and target. Wang et al. [292] combined 64-dimensional AlphaEarth embeddings [14] with Sentinel-2 spectral, textural, and topographic variables in a random-forest classifier [89]; the selected configuration reached 92.69% overall accuracy and a Kappa coefficient of 0.90 in Rizhao, China, and was applied without retraining in Qingdao. Because the model used a combined feature set, this result does not isolate the contribution of AlphaEarth. For 18 tree species and groups in Trentino, Ball et al. [280] found that AlphaEarth [14] and TESSERA [21] increased weighted F1 from 0.80 to 0.83 and macro F1 from 0.50 to 0.55 relative to conventional Sentinel-1/2 composites; performance approached saturation with 5% of the training parcels. Across 6 crop datasets on 5 continents,

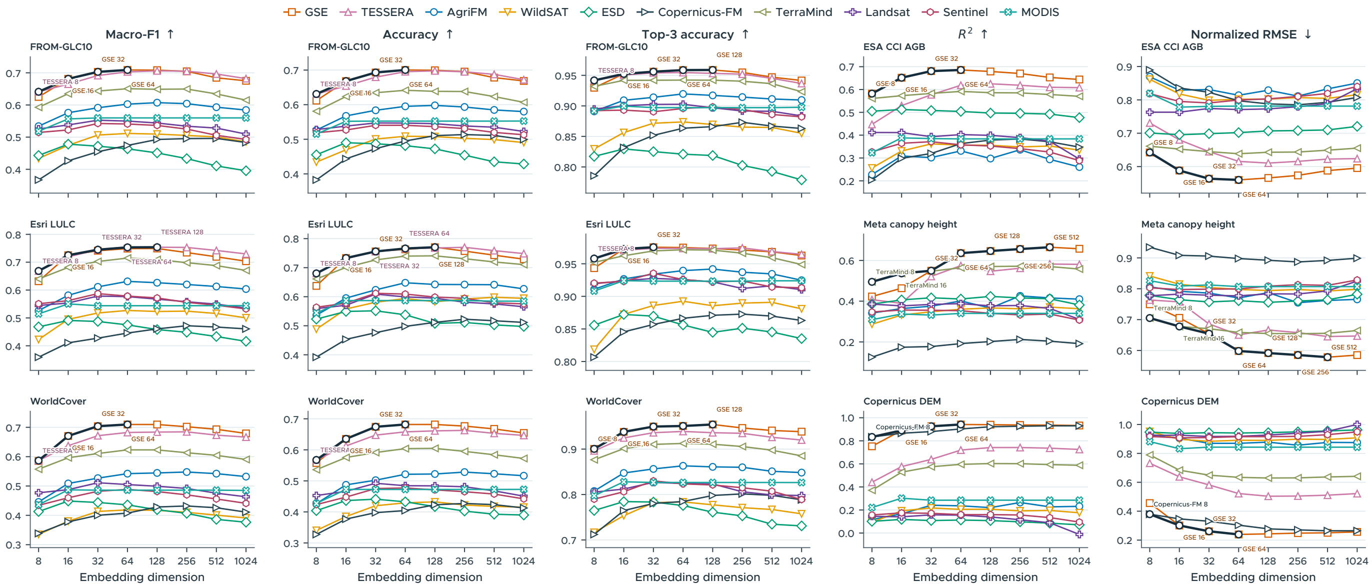

Fig. 20. Predictive performance across embeddings, embedding dimensions, and downstream datasets.

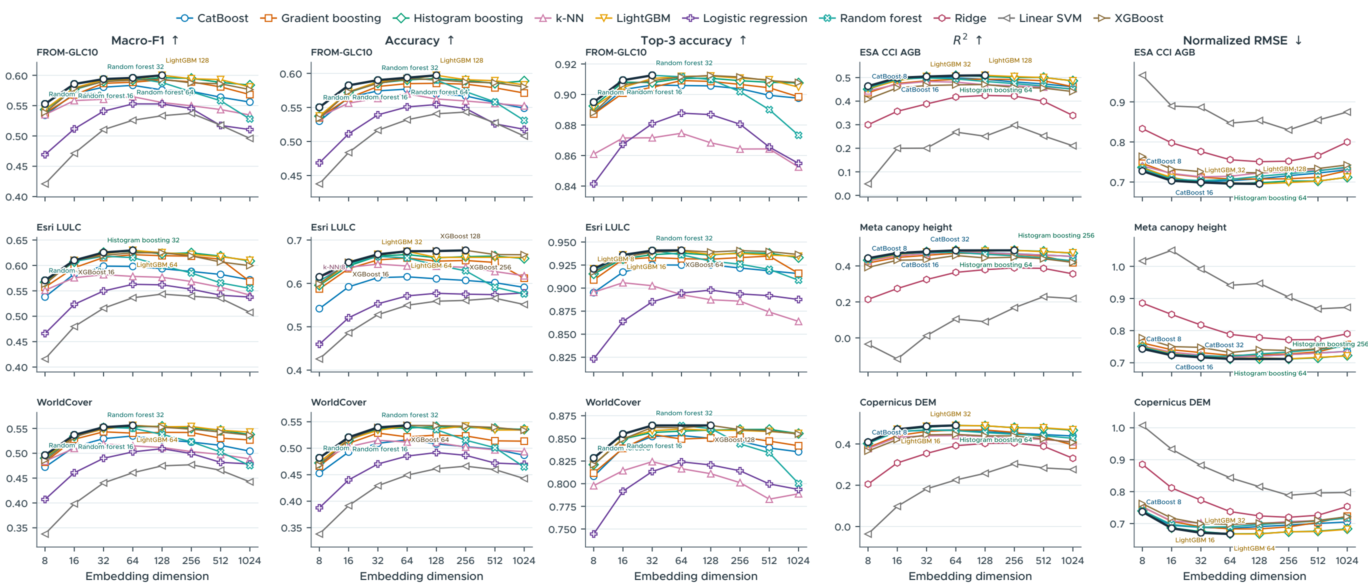

Fig. 21. Predictive performance across prediction models, embedding dimensions, and downstream datasets.

Sentinel-2-specific initialization with SSL4EO-S12 [101] or SatlasPretrain [77] performed better than ImageNet initialization [92], with the largest benefit from out-of-distribution pretraining at 10–100 in-region samples [293].

Temporal alignment limits transfer even when local classification is accurate. In the Trentino experiment, cross-year weighted F1 decreased from 0.81 to 0.73 for TESSERA and from 0.82 to 0.69 for AlphaEarth [280]. In Senegal's groundnut basin, TESSERA [21] scored highest under the authors' performance, plausibility, transferability, and accessibility criteria; one cross-year experiment reported accuracy 28% higher than the next-best method, rather than an average gain across all settings [14], [218]. AlphaEarth was also competitive for locally trained crop-yield prediction and county-level tillage mapping in the United States, but it showed weaker spatial transfer, limited sensitivity to management timing, and lower interpretability [189]. Annual summaries are therefore less suited to agricultural targets determined by within-season events.

Large-area crop mapping also exposes the difference between reusable encoders and precomputed products. AgriFM uses multisource temporal representations for crop mapping, but users must run the released encoder [253]. Zvonkov et al. [272] generated 128-dimensional Presto embeddings [62] over all 56,785 km^2 of Togo in 16 hours at a reported cost of \$313.40, producing a 128.8 GB asset. On CropHarvest, the resulting map reached 0.897 overall accuracy and an F1 score of 0.808, compared with 0.859 and 0.745 for the corresponding AlphaEarth map. WorldCereal likewise uses Presto in its crop-mapping workflow and fine-tunes it on the

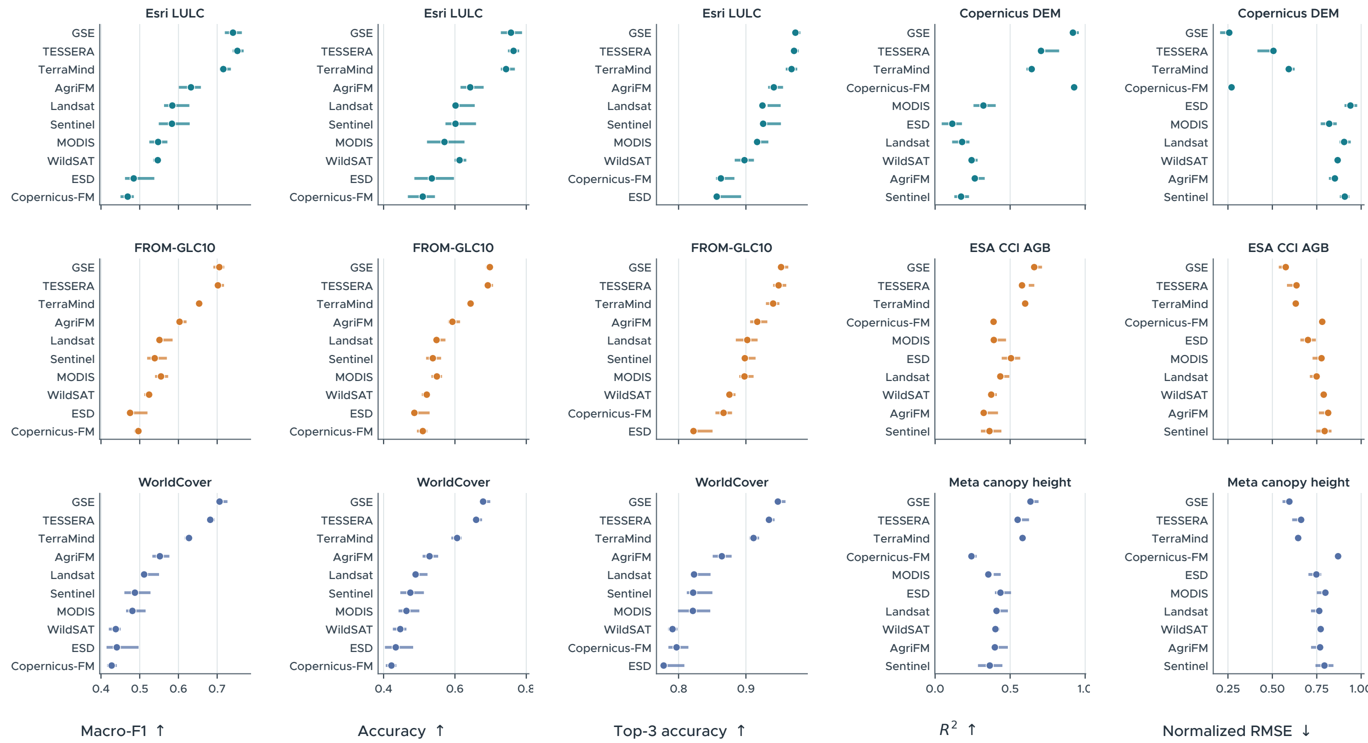

Fig. 22. Predictive performance across embeddings, prediction models, and downstream datasets.

WorldCereal reference database [294].

B. Biophysical Estimation and Environmental Monitoring

Biophysical estimation and environmental monitoring cover vegetation structure, hydrology, terrain, hazards, atmospheric variables, and ecosystem restoration [295]–[313]. Continuous-variable studies show that embeddings can encode environmental gradients without consistently replacing expert covariates or task-specific spatial models. For Danish peatlands, AlphaEarth-only models had RMSE values 6% and 3% higher than expert-variable models for soil organic carbon and water-table depth; hybrid models combining the embeddings with topography, water proximity, and synthetic wet and drained conditions improved the spatial patterns [14], [314]. Over approximately $8{,}000\,\mathrm{km}^2$ of Nouvelle-Aquitaine, an AlphaEarth ridge-regression baseline reached a test R^2 of 0.38 for surface height, compared with 0.78 for U-Net [243] and 0.84 for U-Net++ [315]; U-Net++ had a test RMSE of $16.42\,\mathrm{m}$ [306]. In these studies, embeddings are reusable covariates but do not uniformly replace physically selected variables or spatial architectures.

Performance varies across target strata, regions, and forest types. Forest-biomass prediction from 89 plots at the Yunhe Forestry Station was weak when all plots were pooled ($R^2 = 0.06$), despite comparisons among random forest [89], support vector regression [90], a multilayer perceptron, and Gaussian-process regression. The best R^2 values differed by forest type: 0.33 for broad-leaved forest, 0.13 for mixed forest, and 0.48 for coniferous forest [279]. For landslide susceptibility in Nantou County, Hong Kong, and Emilia-Romagna, CNN1D [266], CNN2D, and Vision Transformer [98] classifiers using the full 64-dimensional AlphaEarth representation improved F1 by approximately 4–15% and AUC by 0.04–0.11 over conventional conditioning factors; PCA-reduced embeddings [126] were less accurate [304].

Temporal aggregation further constrains environmental monitoring. Annual AlphaEarth embeddings paired with 5 air-pollutant records in Quito produced $R^2 = 0.71$ for nitrogen dioxide and sulfur dioxide under fivefold cross-validation, compared with 0.55 for particulate matter, 0.61 for carbon monoxide, and a negative value for ozone [296]. Annual vectors can encode persistent land-use and urban-form correlates, but not all of the short-term chemistry and meteorology needed for atmospheric prediction.

C. Geospatial Retrieval and Socioeconomic Applications

Retrieval uses distances between embeddings directly, whereas socioeconomic prediction adds labels, aggregation choices, and a downstream model. GeoCLIP [18] evaluates worldwide image-to-coordinate retrieval, and Major TOM Embeddings [20] supports similarity search over its released vectors. RANGE [161] augments coordinate embeddings with visual features retrieved from an auxiliary database and reports gains of up to 13.1% on classification and 0.145 in R^2 on regression relative to the evaluated location-embedding baselines. EarthEmbeddingExplorer provides an interactive interface for similarity retrieval over Sentinel-2 imagery [316]. Dimension-level associations have also been used for retrieval with AlphaEarth [317], while FUSAR-GPT injects AlphaEarth spatiotemporal features into a SAR vision–language model for grounded interpretation [318].

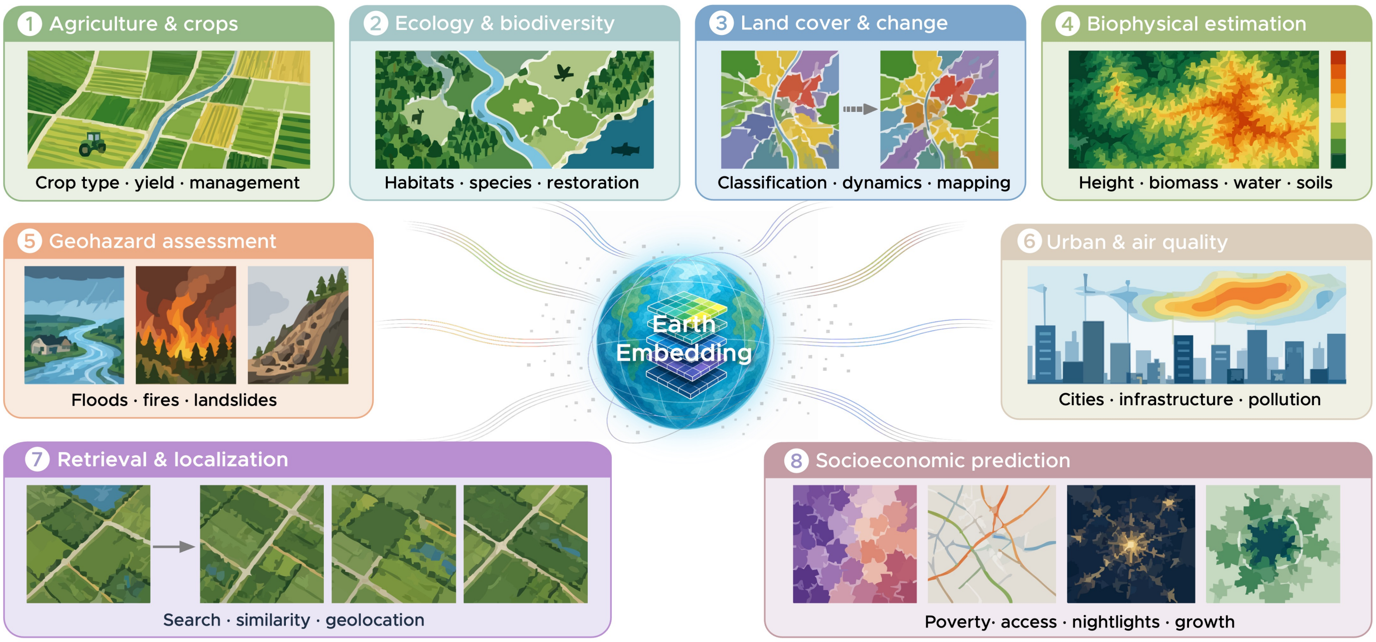

Fig. 23. Application domains supported by Earth embedding products.

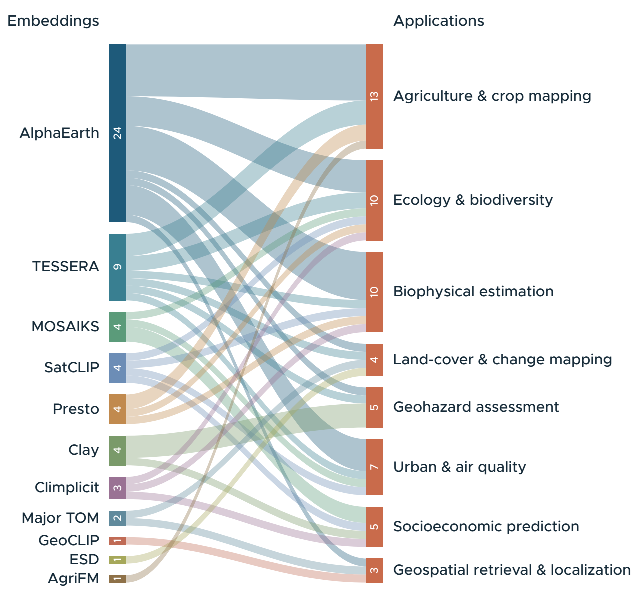

Fig. 24. Links between Earth embeddings and downstream applications.

Socioeconomic applications remain sensitive to the labels and spatial units used for prediction [319]–[324]. MOSAIKS [16] used one precomputed feature set for forest cover, population density, road length, and housing value, and SatCLIP [17] evaluates coordinate embeddings on ecological and socioeconomic tasks. Sherman et al. [325] combined MOSAIKS daytime features with nighttime imagery to estimate the Human Development Index for 61,530 municipalities and 819,309 grid cells. Pettersson and Daoud [319] used AlphaEarth embeddings in a graph neural network across 37 Demographic and Health Survey datasets, where graph structure produced a small improvement over image-only baselines.

Aggregation changes the information presented to the downstream model. Corley et al. [184] compared 11 training-free and 2 parametric methods on 81,000 embedding GeoTIFFs from AlphaEarth, OlmoEarth [326], and TESSERA. Mean pooling reduced accuracy by over 10 points for some embeddings under geographic splits; generalized mean pooling improved accuracy without increasing dimensionality, while concatenated minimum, maximum, mean, and standard-deviation statistics gave the highest accuracy at four times the embedding size. An evaluation using NeuCo-Bench also found mean pooling competitive, although the best layer and objective varied by task [246].

D. *Success Conditions, Failure Modes, and Practical Costs*

Embeddings do not consistently outperform task-specific remote sensing features. Gains are reported when labeled training data are limited, including tea mapping, tree-species classification, and crop transfer with limited in-region training data [280], [292], [293]. Other studies find that embeddings match rather than exceed expert features, or that performance varies sharply across target strata [189], [279], [314]. Comparisons should therefore report the amount of labeled training data, spatial split, target resolution, and baseline feature set.

Temporal information helps when the target follows seasonal trajectories, but the available products do not resolve every temporal process. TESSERA performs well in the Senegal crop-transfer experiment [218], whereas annual AlphaEarth embeddings show limited sensitivity to tillage and cover-crop timing [189]. The same temporal limitation appears in the Quito study, where annual embeddings predict persistent pollution patterns more accurately than ozone dynamics [296].

Flood progression, active fires, and within-season crop management require observations or embeddings updated more frequently than once per year.

Spatial resolution constrains downstream use. A 10 m embedding can provide contextual information for objects smaller than one pixel, but it cannot directly resolve the geometry of individual tree crowns, narrow roads, or small buildings. Pixel-, patch-, scene-, and coordinate-level embeddings should therefore be compared only after matching their support to the label geometry. Pooling experiments further show that converting pixel embeddings to parcel or patch features can alter geographic transfer performance [184].

Geographic transfer remains dependent on the target region and the available labels. Chang et al. [293] found the greatest benefit from remote sensing pretraining with 10–100 in-region samples, but did not remove the need for local data. Ma et al. [189] similarly reported weaker spatial transfer for agricultural practices than for locally trained models. Frozen embeddings reduce feature-computation costs, but they do not correct a mismatch between the downstream labels and the geographic or temporal distribution represented during pretraining.

Computational cost depends on whether vectors are precomputed or generated for the study area. The Togo workflow generated Presto embeddings for $56{,}785\,\mathrm{km}^2$ at a reported cost of \$313.40, or approximately \$5.52 per $1{,}000\,\mathrm{km}^2$ for that cloud computation [272]. This estimate applies only to the reported computation. Precomputed products such as AlphaEarth avoid user-side encoding, but access, storage, label collection, and downstream validation still contribute to total cost.

VI. Challenges and Outlooks

Reliable use of global embedding products requires consistent data specifications, stable representations, uncertainty assessment, and evaluation across regions and time. Fig. 25 relates these requirements to standardization, multimodal data, open access, and evaluation of released products.

A. Standardization and Computational Sustainability

Current products differ in spatial support, file format, temporal definition, and access method. Google Satellite Embedding is distributed as annual, pixel-wise Cloud-Optimized GeoTIFFs [14], [215]; TESSERA uses quantized tiled arrays accessed through GeoTessera [21], [226]; and Major TOM, the Copernicus Global Embeddings Dataset, and LGND Clay Embeddings use GeoParquet for patch- or scene-level vectors and their metadata [20], [23], [219]. Earth Embeddings as Products and recent TorchGeo loaders expose several releases through similar query patterns [37], [227], [228], but they do not remove differences in coordinate reference systems, tiling grids, temporal support, numeric precision, or source-data provenance. A minimal metadata specification should record the encoder and source-data versions, spatial footprint, valid time, numeric encoding, and processing history. OGC work on analysis-ready data and geodatacubes provides a precedent, although it does not yet define an Earth-embedding specification [327].

Combining products requires spatial aggregation, temporal matching, normalization, and dimensional alignment. Google Satellite Embedding stores a 64-dimensional, signed 8-bit annual vector at 10 m resolution [14], [215], whereas the DINOv2 release described by Major TOM stores 1,024-dimensional floating-point vectors for single-date 224-pixel fragments in GeoParquet [9], [20], [141]. Resampling and alignment can change neighborhood structure or remove fine-scale variation. A vector-valued data-cube specification could define spatial and temporal indexes while retaining each product's native support and provenance.

Storage remains a constraint even after inference has been centralized. A global land grid at 10 m resolution contains approximately 1.5×10^{12} cells. At 64 signed 8-bit values per cell, one uncompressed annual layer contains about 96 TB of numeric values before masking, file compression, tiling overhead, and metadata. At a fixed grid and precision, increasing the vector width from 64 to 1,024 multiplies value storage by sixteen, while changing from annual to monthly output multiplies it by twelve. These are upper bounds; actual archive sizes depend on coverage, masking, compression, and spatial support. Compression studies also address different costs. Across 6 remote sensing foundation models and 4 classification tasks, post-hoc slimming retained more than 71% of relative accuracy at 1% of the original floating-point operations [217]; this reduces encoder computation, not vector storage. TESSERA v2 instead reports that a 16-dimensional prefix retains approximately 92% of the aggregate performance of its 128-dimensional vector while using one eighth of the value storage [105]. Quantization [127], ordered dimensions, and spatially coarser summaries may reduce distribution costs, but their effects should be tested separately for classification, continuous-variable regression, rare classes, and temporal change.

Precomputed layers reduce computation for users but do not eliminate the cost of training, global inference, hosting, and repeated updates. Current planetary releases depend on producers that can maintain large accelerator and object-storage resources [14], [21], [57], so long-term reliability depends on continued compute, storage, and maintenance. Google states that annual Satellite Embedding production will continue subject to source-data availability and that anticipated delivery changes will receive advance notice [215]. Comparable version, update, and deprecation policies are not yet documented consistently across the reviewed products. Stable archives and explicit maintenance responsibility are therefore prerequisites for long-term access, including community or public-sector mirrors.

B. Temporal Coherence and Representational Stability

Temporal support differs substantially among released embeddings. Google Satellite Embedding and TESSERA provide annual summaries [14], [15], [21]; ESD retains within-year temporal information in each annual record [57]; and Major TOM and the Copernicus Global Embeddings Dataset

Fig. 25. Challenges and research directions for global Earth embedding products.

associate vectors with individual source acquisitions [20], [219]. The current public LGND Clay collection instead provides monthly aggregated chip-level embeddings beginning in 2017 [23]. An annual vector cannot directly represent the timing of an event within the year, while acquisition-level collections preserve time at a much higher storage and processing cost. Generative models such as DiffusionSat support temporal generation, multispectral super-resolution, and inpainting [328]. No reviewed product reports that generated observations improve embedding stability.

Encoder updates create a separate compatibility problem. Let f_{old} and f_{new} denote two encoder versions. Reusing a downstream predictor trained on the old representation requires a map from the new space to the old one, for example

$$f_{\text{old}}(\mathbf{x}) \approx \mathbf{A} f_{\text{new}}(\mathbf{x}). \tag{21}$$

If a linear map $\mathbf{A}$ is accurate on the relevant data, an existing predictor g_{old} can be evaluated as $g_{\text{old}}(\mathbf{A} f_{\text{new}}(\mathbf{x}))$. Orthogonal Procrustes analysis provides one way to estimate a linear alignment [329], but it does not guarantee preservation of task-relevant information. A nonlinear adapter, regeneration of historical embeddings, or retraining of the downstream predictor may be needed when linear alignment is inadequate.

Backward-compatible representation learning treats compatibility as an explicit model-update objective rather than a post-hoc correction [330]. It has been evaluated for visual retrieval, but not for global Earth embedding products. Product updates should therefore include overlap periods generated by both encoder versions, compatibility tests on selected downstream tasks, and an explicit statement of whether old and new vectors can be compared directly. A frozen reference release remains useful when backward compatibility cannot be guaranteed.

Version changes also affect longitudinal analysis. If adjacent annual layers are generated by different encoders, an observed difference can reflect either surface change or representation drift. Regenerating the complete historical archive with each encoder removes this ambiguity but is costly and changes previously published results. Each layer should record the encoder, source archive, preprocessing configuration, and inference date, and mixed-version time series should not be treated as homogeneous without explicit compatibility tests.

C. *Interpretability, Uncertainty, and Trustworthiness*

Embedding dimensions do not correspond directly to named physical variables, which limits the explanations that can accompany scientific or policy decisions. A downstream predictor can identify influential dimensions, but this does not by itself show which observations, environmental processes, or preprocessing choices produced the signal. Interpretation must therefore distinguish statistical predictability from physical meaning.

Rahman [317] analyzes AlphaEarth embeddings using dimension-wise rank correlations as well as random-forest and Transformer models fitted to the complete 64-dimensional vector. The resulting dimension dictionary identifies recurring associations with 26 environmental variables, while spatial and temporal tests examine the stability of those associations. The study models all 64 dimensions but reports their associations through a dimension-level dictionary. Correlation, permutation importance, gradients, and attention weights do not establish causal correspondence between a latent dimension and a physical process. Disentangled representation learning [331], [332] and physics-informed learning [333] offer possible tools, although their assumptions and utility have not been established for released global embeddings.

Current released embedding layers do not expose calibrated, location-specific uncertainty estimates. This differs from uncertainty in a downstream prediction, which depends on labels, the prediction model, and the deployment distribution. Encoder ensembles can measure representation disagreement, but ensemble spread is not automatically calibrated uncertainty and repeated global inference is expensive. Nearest-neighbor distance in a reference feature space has been used for out-of-distribution detection [334]; applied to Earth embeddings, it would flag vectors far from a reference collection but would not distinguish a previously unseen surface from sparse sampling. AlphaEarth's von Mises–Fisher bottleneck does not provide a released confidence value for each location: its concentration parameter is fixed during model construction [14]. Confidence measures intended for comparison across products will require held-out geographic and temporal tests together with calibration against observed downstream errors.

Task accuracy alone is insufficient for claims about reliable use. REOBench measures sensitivity to 12 image-corruption types across 6 tasks [242], while EarthShift evaluates changes in geography, time, scale, sensor, and data source and reports average out-of-distribution degradation of 15–20% across 8 geospatial foundation models and 11 tasks [335]. Although these studies evaluate model features, their protocols can also test released embeddings. Reliability claims also require documentation of data gaps, supported temporal and spatial scales, version history, and validation outside the regions used to fit downstream predictors.

D. Geographic Equity and Representational Bias

Planetary coverage does not imply uniform representation quality. Pretraining collections use different spatial sampling strategies: MMEarth balances 1.2 million locations across 14 biomes [69], whereas SSL4EO-S12 samples approximately 250,000 locations around the world's 10,000 most populated cities and removes most patch overlap [101]. Kaur et al. [336] report that the geographic and spectral composition of pretraining data affects downstream performance, with the preferred sampling strategy depending on the model and target distribution. Coverage maps and sample counts should therefore be accompanied by distributions over biome, sensor conditions, acquisition time, and relevant target populations.

MMEarth-Bench reports lower performance under geographic transfer across five environmental tasks and 12 modalities [337]. EarthShift reports similar losses across shifts in geography, time, scale, sensor, and data source [335]. Comparisons across climate, data availability, and socioeconomic conditions require the same tasks, spatially separated labels, identical downstream protocols, and enough observations in each group to separate representation quality from label noise and target prevalence.

Observation conditions also vary geographically. Persistent cloud, seasonal snow, illumination geometry, topographic shadow, and sensor revisit patterns alter which measurements are available at a location [338]. These factors can create distribution shifts, but their effect on embedding quality must be measured rather than inferred from geography alone. Multimodal products may reduce dependence on any single sensor, and a recent comparison found that combinations of AlphaEarth, TESSERA, GeoCLIP, and SatCLIP improved on the best individual embedding in four of six evaluated tasks; the gains remained task- and location-dependent [185]. Regional evaluation should therefore report source availability and test both individual and combined embeddings under the same labels and splits.

Users of general-purpose vectors still select labels, choose aggregation rules, train task-specific predictors, and validate outputs. Evaluation of released products should combine spatial and temporal holdouts with categorical and continuous targets, while reporting storage, access, and prediction costs alongside accuracy. NeuCo-Bench evaluates fixed embeddings and compression with the same procedure across tasks [182], and robustness benchmarks measure geographic and sensor shifts. Rare classes, rapid change, uncertainty calibration, and cross-product fusion remain poorly tested in released embeddings.

VII. Conclusion

Earth embedding research now includes reusable image encoders, coordinate-based models, and precomputed vector collections [14], [17], [21], [23], [76]. The product releases are the main practical change: users can download or query vectors instead of rerunning feature extraction over large image archives. Because a vector may represent a coordinate, image tile, pixel, or temporal sequence, product choice must match the spatial and temporal scale of the intended analysis.

Community benchmarks show that embedding performance depends on the prediction task, available labels, and evaluation protocol [182], [183], [237]. In our experiments, similarity between feature spaces did not determine classification or regression accuracy, and increasing embedding dimension did not consistently improve prediction. Application studies likewise report benefits for some mapping and estimation tasks, while results vary across targets, regions, and temporal settings [189], [280], [293], [314]. These findings support evaluation by task and region rather than a universal ordering of embeddings.

Future releases need explicit specifications for spatial and temporal support, masking, precision, aggregation, and encoder versions. Evaluation should cover predictive quality, geographic and temporal transfer, uncertainty, and compatibility across updates [37], [335], [337]. Stable interfaces, version records, and continued access to historical vectors are necessary if Earth embeddings are to function as reproducible geospatial data products rather than transient model outputs.

References

[1] Copernicus Data Space Ecosystem, "Copernicus Data Space Ecosystem Dashboard—Accurate and Up-to-Date Insights in the Ecosystem," https://dataspace.copernicus.eu/news/2023-12-21-copernicus-data-space-ecosystem-dashboard-accurate-and-date-insights-ecosystem, 2023, accessed: Aug. 2, 2026.

[2] U.S. Geological Survey, "Landsat missions," https://www.usgs.gov/landsat-missions, 2026.

[3] NASA Harmonized Landsat Sentinel-2 Project, “Harmonized landsat and sentinel-2 data products,” https://hls.gsfc.nasa.gov/data-products/, 2026, accessed: Aug. 2, 2026.

[4] D. Tuia, R. Roscher, J. D. Wegner, N. Jacobs, X. Zhu, and G. Camps-Valls, “Toward a collective agenda on ai for earth science data analysis,” *IEEE Geosci. Remote Sens. Mag.*, vol. 9, no. 2, pp. 88–104, Jun. 2021. [Online]. Available: http://dx.doi.org/10.1109/mgrs.2020.3043504

[5] T. Chen, S. Kornblith, M. Norouzi, and G. Hinton, “A simple framework for contrastive learning of visual representations,” in *Proc. Int. Conf. Mach. Learn. (ICML)*, ser. Proceedings of Machine Learning Research, H. D. III and A. Singh, Eds., vol. 119. PMLR, 13–18 Jul 2020, pp. 1597–1607. [Online]. Available: https://proceedings.mlr.press/v119/chen20j.html

[6] K. He, H. Fan, Y. Wu, S. Xie, and R. Girshick, “Momentum contrast for unsupervised visual representation learning,” in *Proc. IEEE/CVF Conf. Comput. Vis. Pattern Recognit. (CVPR)*. IEEE, June 2020, pp. 9729–9738. [Online]. Available: http://dx.doi.org/10.1109/cvpr42600.2020.00975

[7] K. He, X. Chen, S. Xie, Y. Li, P. Dollár, and R. Girshick, “Masked autoencoders are scalable vision learners,” in *Proc. IEEE/CVF Conf. Comput. Vis. Pattern Recognit. (CVPR)*. IEEE, June 2022, pp. 16 000–16 009. [Online]. Available: http://dx.doi.org/10.1109/cvpr52688.2022.01553

[8] M. Caron, H. Touvron, I. Misra, H. Jégou, J. Mairal, P. Bojanowski, and A. Joulin, “Emerging properties in self-supervised vision transformers,” in *Proc. IEEE/CVF Int. Conf. Comput. Vis. (ICCV)*. IEEE, October 2021, pp. 9650–9660. [Online]. Available: http://dx.doi.org/10.1109/iccv48922.2021.00951

[9] M. Oquab, T. Darcet, T. Moutakanni, H. V. Vo, M. Szafraniec, V. Khalidov, P. Fernandez, D. Haziza, F. Massa, A. El-Nouby, M. Assran, N. Ballas, W. Galuba, R. Howes, P.-Y. Huang, S.-W. Li, I. Misra, M. Rabbat, V. Sharma, G. Synnaeve, H. Xu, H. Jégou, J. Mairal, P. Labatut, A. Joulin, and P. Bojanowski, “DINOv2: Learning robust visual features without supervision,” *Trans. Mach. Learn. Res.*, 2024. [Online]. Available: https://openreview.net/forum?id=a68SUt6zFt

[10] D. Szwarcman, S. Roy, P. Fraccaro, T. E. Gíslason, B. Blumenstiel, R. Ghosal, P. H. de Oliveira, J. L. de Sousa Almeida, R. Sedona, Y. Kang, S. Chakraborty, S. Wang, C. Gomes, A. Kumar, V. Gaur, M. Truong, D. Godwin, S. Khallaghi, H. Lee, C.-Y. Hsu, A. A. Asanjan, B. Mujeci, D. Shidham, R. O. Balogun, V. Kolluru, T. Keenan, P. Arevalo, W. Li, H. Alemohammad, P. Olofsson, T. Mayer, C. Hain, R. Kennedy, B. Zadrozny, D. Bell, G. Cavallaro, C. Watson, M. Maskey, R. Ramachandran, and J. B. Moreno, “Prithvi-eo-2.0: A versatile multitemporal foundation model for earth observation applications,” *IEEE Trans. Geosci. Remote Sens.*, vol. 64, pp. 1–20, 2026. [Online]. Available: http://dx.doi.org/10.1109/tgrs.2025.3642610

[11] D. Hong, B. Zhang, X. Li, Y. Li, C. Li, J. Yao, N. Yokoya, H. Li, P. Ghamisi, X. Jia, A. Plaza, P. Gamba, J. A. Benediktsson, and J. Chanussot, “Spectralgpt: Spectral remote sensing foundation model,” *IEEE Trans. Pattern Anal. Mach. Intell.*, vol. 46, no. 8, pp. 5227–5244, Aug. 2024. [Online]. Available: http://dx.doi.org/10.1109/tpami.2024.3362475

[12] C. J. Reed, R. Gupta, S. Li, S. Brockman, C. Funk, B. Clipp, K. Keutzer, S. Candido, M. Uyttendaele, and T. Darrell, “Scale-mae: A scale-aware masked autoencoder for multiscale geospatial representation learning,” in *Proc. IEEE/CVF Int. Conf. Comput. Vis. (ICCV)*. IEEE, October 2023, pp. 4088–4099. [Online]. Available: https://openaccess.thecvf.com/content/ICCV2023/html/Reed_Scale-MAE_A_Scale-Aware_Masked_Autoencoder_for_Multiscale_Geospatial_Representation_Learning_ICCV_2023_paper.html

[13] Z. Xiong, Y. Wang, F. Zhang, A. J. Stewart, J. Hanna, D. Borth, I. Papoutsis, B. Le Saux, G. Camps-Valls, and X. X. Zhu, “Neural plasticity-inspired multimodal foundation model for earth observation,” 2024. [Online]. Available: https://arxiv.org/abs/2403.15356

[14] C. F. Brown, M. R. Kazmierski, V. J. Pasquarella, W. J. Rucklidge, M. Samsikova, C. Zhang, E. Shelhamer, E. Lahera, O. Wiles, S. Ilyushchenko, N. Gorelick, L. L. Zhang, S. Alj, E. Schechter, S. Askay, O. Guinan, R. Moore, A. Boukouvalas, and P. Kohli, “Alphaearth foundations: An embedding field model for accurate and efficient global mapping from sparse label data,” 2025. [Online]. Available: https://arxiv.org/abs/2507.22291

[15] Google Earth Engine, “Satellite embedding V1,” Earth Engine Data Catalog, https://developers.google.com/earth-engine/datasets/catalog/GOOGLE_SATELLITE_EMBEDDING_V1_ANNUAL, 2026, accessed: Jul. 30, 2026.

[16] E. Rolf, J. Proctor, T. Carleton, I. Bolliger, V. Shankar, M. Ishihara, B. Recht, and S. Hsiang, “A generalizable and accessible approach to machine learning with global satellite imagery,” *Nat. Commun.*, vol. 12, no. 1, p. 4392, jul 2021. [Online]. Available: http://dx.doi.org/10.1038/s41467-021-24638-z

[17] K. Klemmer, E. Rolf, C. Robinson, L. Mackey, and M. Rußwurm, “Satclip: Global, general-purpose location embeddings with satellite imagery,” *Proc. AAAI Conf. Artif. Intell.*, vol. 39, no. 4, pp. 4347–4355, Apr. 2025. [Online]. Available: http://dx.doi.org/10.1609/aaai.v39i4.32457

[18] V. Vivanco Cepeda, G. K. Nayak, and M. Shah, “Geoclip: Clip-inspired alignment between locations and images for effective worldwide geo-localization,” in *Adv. Neural Inf. Process. Syst.*, ser. NeurIPS 2023, vol. 36. Curran Associates, Inc., 2023, pp. 8690–8701. [Online]. Available: https://proceedings.neurips.cc/paper_files/paper/2023/file/1b57aaddf85ab01a2445a79c9edc1f4b-Paper-Conference.pdf

[19] A. Francis and M. Czerkawski, “Major tom: Expandable datasets for earth observation,” in *Proc. IEEE Int. Geosci. Remote Sens. Symp. (IGARSS)*. IEEE, Jul. 2024, pp. 2935–2940. [Online]. Available: http://dx.doi.org/10.1109/igarss53475.2024.10640760

[20] M. Czerkawski, M. Kluczek, and J. S. Bojanowski, “Global and dense embeddings of earth: Major tom floating in the latent space,” 2024. [Online]. Available: https://arxiv.org/abs/2412.05600

[21] Z. Feng, C. Atzberger, S. Jaffer, J. Knezevic, S. Sormunen, R. Young, M. C. Lisaius, M. Immitzer, T. Jackson, J. Ball, D. A. Coomes, A. Madhavapeddy, A. Blake, and S. Keshav, “Tessera: Temporal embeddings of surface spectra for earth representation and analysis,” in *Proc. IEEE/CVF Conf. Comput. Vis. Pattern Recognit. (CVPR)*, Jun. 2026, pp. 34 818–34 831.

[22] Clay Foundation, “Pretrained model release v1.5,” https://clay-foundation.github.io/model/release-notes/specification.html, 2024.

[23] LGND.ai, “LGND embeddings,” Source Cooperative, https://source.coop/clay/lgnd-embeddings, 2026, accessed: Jul. 30, 2026.

[24] T. Mikolov, K. Chen, G. Corrado, and J. Dean, “Efficient estimation of word representations in vector space,” in *Proc. Int. Conf. Learn. Represent. Workshop*, 2013. [Online]. Available: https://iclr.cc/archive/2013/workshop-proceedings.html

[25] J. Pennington, R. Socher, and C. Manning, “GloVe: Global vectors for word representation,” in *Proc. Conf. Empirical Methods Natural Lang. Process. (EMNLP)*, A. Moschitti, B. Pang, and W. Daelemans, Eds. Doha, Qatar: Association for Computational Linguistics, October 2014, pp. 1532–1543. [Online]. Available: https://aclanthology.org/D14-1162/

[26] J. Devlin, M.-W. Chang, K. Lee, and K. Toutanova, “BERT: Pre-training of deep bidirectional transformers for language understanding,” in *Proc. Conf. North Amer. Chapter Assoc. Comput. Linguistics: Human Lang. Technol. (NAACL-HLT)*, J. Burstein, C. Doran, and T. Solorio, Eds. Minneapolis, Minnesota: Association for Computational Linguistics, Jun. 2019, pp. 4171–4186. [Online]. Available: https://aclanthology.org/N19-1423/

[27] G. Mai, W. Huang, J. Sun, S. Song, D. Mishra, N. Liu, S. Gao, T. Liu, G. Cong, Y. Hu, C. Cundy, Z. Li, R. Zhu, and N. Lao, “On the opportunities and challenges of foundation models for geoai (vision paper),” *ACM Trans. Spatial Algorithms Syst.*, vol. 10, no. 2, pp. 1–46, jun 2024. [Online]. Available: http://dx.doi.org/10.1145/3653070

[28] S. Lu, J. Guo, J. R. Zimmer-Dauphinee, J. M. Nieusma, X. Wang, P. VanValkenburgh, S. A. Wernke, and Y. Huo, “Vision foundation models in remote sensing: A survey,” *IEEE Geosci. Remote Sens. Mag.*, vol. 13, no. 3, pp. 190–215, Sep. 2025. [Online]. Available: http://dx.doi.org/10.1109/mgrs.2025.3541952

[29] A. Xiao, W. Xuan, J. Wang, J. Huang, D. Tao, S. Lu, and N. Yokoya, “Foundation models for remote sensing and earth observation: A survey,” *IEEE Geosci. Remote Sens. Mag.*, vol. 13, no. 4, pp. 297–324, Dec. 2025. [Online]. Available: http://dx.doi.org/10.1109/mgrs.2025.3576766

[30] L. Yang, N. Chen, J. Yue, Y. Liu, J. Ma, P. Ghamisi, A. Plaza, and L. Fang, “Survey of multimodal geospatial foundation models: Techniques, applications, and challenges,” 2025. [Online]. Available: https://arxiv.org/abs/2510.22964

[31] G. Zhou, L. Qian, and P. Gamba, “Advances on multimodal remote sensing foundation models for earth observation downstream tasks: A survey,” *Remote Sens.*, vol. 17, no. 21, p. 3532, Oct. 2025. [Online]. Available: http://dx.doi.org/10.3390/rs17213532

[32] Z. Huang, H. Yan, Q. Zhan, S. Yang, M. Zhang, C. Zhang, Y. Lei, Z. Liu, Q. Liu, and Y. Wang, “A survey on remote sensing foundation models: From vision to multimodality,” 2025. [Online]. Available: https://arxiv.org/abs/2503.22081

[33] D. Hong, C. Li, X. Li, G. Camps-Valls, and J. Chanussot, "Foundation models in remote sensing: Evolving from unimodality to multimodality," *IEEE Geosci. Remote Sens. Mag.*, vol. 14, no. 2, pp. 10–35, Apr. 2026. [Online]. Available: http://dx.doi.org/10.1109/mgrs.2026.3669086

[34] K. Lane and M. Karimzadeh, "A genealogy of foundation models in remote sensing," *ACM Trans. Spatial Algorithms Syst.*, vol. 12, no. 3, pp. 1–36, May 2026. [Online]. Available: http://dx.doi.org/10.1145/3789505

[35] C. Huo, K. Chen, S. Zhang, Z. Wang, H. Yan, J. Shen, Y. Hong, G. Qi, H. Fang, and Z. Wang, "When remote sensing meets foundation model: A survey and beyond," *Remote Sens.*, vol. 17, no. 2, p. 179, Jan. 2025. [Online]. Available: http://dx.doi.org/10.3390/rs17020179

[36] X. X. Zhu, Z. Xiong, Y. Wang, A. J. Stewart, K. Heidler, Y. Wang, Z. Yuan, T. Dujardin, Q. Xu, and Y. Shi, "On the foundations of earth foundation models," *Commun. Earth Environ.*, vol. 7, no. 1, p. 103, jan 2026. [Online]. Available: http://dx.doi.org/10.1038/s43247-025-03127-x

[37] H. Fang, A. J. Stewart, I. Corley, X. X. Zhu, and H. Azizpour, "Earth embeddings as products: Taxonomy, ecosystem, and standardized access," 2026. [Online]. Available: https://arxiv.org/abs/2601.13134

[38] E. Rolf, K. Klemmer, and M. Rußwurm, "Earth embeddings: Harnessing the information in earth observation data with machine learning," in *Proc. ACM SIGGRAPH Conf. Frontiers*, ser. SIGGRAPH Frontiers '25. ACM, Aug. 2025, pp. 1–2. [Online]. Available: http://dx.doi.org/10.1145/3736539.3754446

[39] K. Klemmer, E. Rolf, M. Rußwurm, G. Camps-Valls, M. Czerkawski, S. Ermon, A. Francis, N. Jacobs, H. Kerner, L. Mackey, G. Mai, O. Mac Aodha, M. Reichstein, C. Robinson, D. Rolnick, E. Shelhamer, V. Sitzmann, D. Tuia, and X. Zhu, "Earth embeddings: Toward artificial intelligence-centric representations of our planet," *IEEE Geosci. Remote Sens. Mag.*, pp. 2–15, 2026. [Online]. Available: https://doi.org/10.1109/MGRS.2026.3710416

[40] C. Gomes, I. Wittmann, D. Robert, J. Jakubik, T. Reichelt, S. Maurogiovanni, R. Vinge, J. Hurst, E. Scheurer, R. Sedona, T. Brunschwiler, S. Kesselheim, M. Batič, P. Stier, J. D. Wegner, G. Cavallaro, E. Pebesma, M. Marszalek, M. A. Belenguer-Plomer, K. Adriko, P. Fraccaro, R. Kienzler, R. Briq, S. Benassou, M. Lazzarini, and C. M. Albrecht, "Lossy neural compression for geospatial analytics: A review," *IEEE Geosci. Remote Sens. Mag.*, vol. 13, no. 3, pp. 97–135, Sep. 2025. [Online]. Available: http://dx.doi.org/10.1109/mgrs.2025.3546527

[41] L. Wang, "Satellite embedding: A review," jun 2026. [Online]. Available: https://eartharxiv.org/repository/view/13346/

[42] A. J. Stewart, H. Fang, I. A. Corley, and X. X. Zhu, "Earth embeddings," 2026, book chapter. [Online]. Available: https://arxiv.org/abs/2608.03410

[43] J. Priem, H. Piwowar, and R. Orr, "Openalex: A fully-open index of scholarly works, authors, venues, institutions, and concepts," in *Proc. 26th Int. Conf. Sci. Technol. Innov. Indicators (STI)*. Centre for Science and Technology Studies, Leiden University, 2022. [Online]. Available: https://doi.org/10.5281/zenodo.6936227

[44] M. Drusch, U. Del Bello, S. Carlier, O. Colin, V. Fernandez, F. Gascon, B. Hoersch, C. Isola, P. Laberinti, P. Martimort, A. Meygret, F. Spoto, O. Sy, F. Marchese, and P. Bargellini, "Sentinel-2: Esa's optical high-resolution mission for gmes operational services," *Remote Sens. Environ.*, vol. 120, pp. 25–36, May 2012. [Online]. Available: http://dx.doi.org/10.1016/j.rse.2011.11.026

[45] M. Claverie, J. Ju, J. G. Masek, J. L. Dungan, E. F. Vermote, J.-C. Roger, S. V. Skakun, and C. Justice, "The harmonized landsat and sentinel-2 surface reflectance data set," *Remote Sens. Environ.*, vol. 219, pp. 145–161, Dec. 2018. [Online]. Available: http://dx.doi.org/10.1016/j.rse.2018.09.002

[46] R. Torres, P. Snoeij, D. Geudtner, D. Bibby, M. Davidson, E. Attema, P. Potin, B. Rommen, N. Floury, M. Brown, I. N. Traver, P. Deghaye, B. Duesmann, B. Rosich, N. Miranda, C. Bruno, M. L'Abbate, R. Croci, A. Pietropaolo, M. Huchler, and F. Rostan, "Gmes sentinel-1 mission," *Remote Sens. Environ.*, vol. 120, pp. 9–24, May 2012. [Online]. Available: http://dx.doi.org/10.1016/j.rse.2011.05.028

[47] A. Rosenqvist, M. Shimada, S. Suzuki, F. Ohgushi, T. Tadono, M. Watanabe, K. Tsuzuku, T. Watanabe, S. Kamijo, and E. Aoki, "Operational performance of the alos global systematic acquisition strategy and observation plans for alos-2 palsar-2," *Remote Sens. Environ.*, vol. 155, pp. 3–12, Dec. 2014. [Online]. Available: http://dx.doi.org/10.1016/j.rse.2014.04.011

[48] R. Dubayah, J. B. Blair, S. Goetz, L. Fatoyinbo, M. Hansen, S. Healey, M. Hofton, G. Hurtt, J. Kellner, S. Luthcke, J. Armston, H. Tang, L. Duncanson, S. Hancock, P. Jantz, S. Marselis, P. L. Patterson, W. Qi, and C. Silva, "The global ecosystem dynamics investigation: High-resolution laser ranging of the earth's forests and topography," *Sci. Remote Sens.*, vol. 1, p. 100002, Jun. 2020. [Online]. Available: http://dx.doi.org/10.1016/j.srs.2020.100002

[49] J. Muñoz-Sabater, E. Dutra, A. Agustí-Panareda, C. Albergel, G. Arduini, G. Balsamo, S. Boussetta, M. Choulga, S. Harrigan, H. Hersbach, B. Martens, D. G. Miralles, M. Piles, N. J. Rodríguez-Fernández, E. Zsoter, C. Buontempo, and J.-N. Thépaut, "Era5-land: a state-of-the-art global reanalysis dataset for land applications," *Earth Syst. Sci. Data*, vol. 13, no. 9, pp. 4349–4383, Sep. 2021. [Online]. Available: http://dx.doi.org/10.5194/essd-13-4349-2021

[50] "Copernicus DEM," 2022. [Online]. Available: https://dataspace.copernicus.eu/explore-data/data-collections/copernicus-contributing-missions/collections-description/COP-DEM

[51] NASA Earthdata, "VIIRS," https://www.earthdata.nasa.gov/data/instruments/viirs, 2024, accessed: Aug. 13, 2026.

[52] European Space Agency, "Sentinel-3," https://www.esa.int/Applications/Observing_the_Earth/Copernicus/Sentinel-3, 2026.

[53] A. Neuenschwander, K. Pitts, B. Jelley, J. Robbins, J. Markel, S. Popescu, R. Nelson, D. Harding, D. Pederson, B. Klotz, and R. Sheridan, "ATLAS/ICESat-2 L3A land and vegetation height, version 7," 2025. [Online]. Available: https://nsidc.org/data/atl08/versions/7

[54] European Space Agency, "Sentinel-5p," https://www.esa.int/Applications/Observing_the_Earth/Copernicus/Sentinel-5P, 2026.

[55] Planet Labs, "Planetscope," https://docs.planet.com/data/imagery/planetscope/, 2026, accessed: Aug. 13, 2026.

[56] Earth Resources Observation and Science (EROS) Center, "USGS EROS Archive – aerial photography – national agriculture imagery program (NAIP)," https://www.usgs.gov/centers/eros/science/usgs-eros-archive-aerial-photography-national-agriculture-imagery-program-naip, 2018.

[57] S. Chen, J. Wang, S. Yuan, J. Li, Y. Xia, Y. Liao, J. Wei, J. Yuan, X. Xu, X. Zhu, P. Zhu, H. Zhang, Y. Zhou, H. Fu, H. Huang, B. Chen, F. Dai, and P. Gong, "Democratizing planetary-scale analysis: an ultra-lightweight earth embedding database for accurate and flexible global land monitoring," *Earth Syst. Sci. Data*, vol. 18, no. 7, pp. 5375–5398, Jul. 2026. [Online]. Available: http://dx.doi.org/10.5194/essd-18-5375-2026

[58] S. Chen, J. Wang, Q. Liu, X. Liang, R. Liu, P. Qin, J. Yuan, J. Wei, S. Yuan, H. Huang, and P. Gong, "Global 30 m seamless data cube (2000–2022) of land surface reflectance generated from landsat 5, 7, 8, and 9 and modis terra constellations," *Earth Syst. Sci. Data*, vol. 16, no. 11, pp. 5449–5475, Nov. 2024. [Online]. Available: http://dx.doi.org/10.5194/essd-16-5449-2024

[59] Y. Cong, S. Khanna, C. Meng, P. Liu, E. Rozi, Y. He, M. Burke, D. Lobell, and S. Ermon, "Satmae: Pre-training transformers for temporal and multi-spectral satellite imagery," in *Adv. Neural Inf. Process. Syst.*, ser. NeurIPS 2022, vol. 35. Curran Associates, Inc., 2022, pp. 197–211. [Online]. Available: https://proceedings.neurips.cc/paper_files/paper/2022/file/01c561df365429f33fcd7a7faa44c985-Paper-Conference.pdf

[60] Y. Wang, Z. Xiong, C. Liu, A. J. Stewart, T. Dujardin, N. I. Bountos, A. Zavras, F. Gerken, I. Papoutsis, L. Leal-Taixé, and X. X. Zhu, "Towards a unified copernicus foundation model for earth vision," in *Proc. IEEE/CVF Int. Conf. Comput. Vis. (ICCV)*. IEEE, Oct. 2025, pp. 9888–9899. [Online]. Available: http://dx.doi.org/10.1109/iccv51701.2025.00922

[61] Earth Resources Observation and Science (EROS) Center, "Landsat 8-9 operational land imager / thermal infrared sensor level-1, collection 2," 2020, accessed: Aug. 2, 2026. [Online]. Available: https://www.usgs.gov/centers/eros/science/usgs-eros-archive-landsat-archives-landsat-8-9-operational-land-imager-and

[62] G. Tseng, R. Cartuyvels, I. Zvonkov, M. Purohit, D. Rolnick, and H. R. Kerner, "Lightweight, pre-trained transformers for remote sensing timeseries," in *NeurIPS 2023 Workshop Tackling Climate Change Mach. Learn.*, 2023. [Online]. Available: https://www.climatechange.ai/papers/neurips2023/58

[63] N. Simumba, N. Lehmann, P. Fraccaro, H. Alemohammad, G. De Mel, S. Khan, M. Maskey, N. Longepe, X. X. Zhu, H. Kerner, J. Bernabe-Moreno, and A. Lacoste, "Geo-bench-2: From performance to capability, rethinking evaluation in geospatial ai," 2025. [Online]. Available: https://arxiv.org/abs/2511.15658

[64] NASA Earthdata, "MODIS," https://www.earthdata.nasa.gov/data/instruments/modis, 2024, accessed: Aug. 13, 2026.

[65] M. Schmitt, L. H. Hughes, C. Qiu, and X. X. Zhu, "Sen12ms – a curated dataset of georeferenced multi-spectral sentinel-1/2 imagery for deep learning and data fusion," *ISPRS Ann. Photogramm. Remote Sens. Spatial Inf. Sci.*, vol. IV-2/W7, pp. 153–160, Sep. 2019. [Online]. Available: http://dx.doi.org/10.5194/isprs-annals-iv-2-w7-153-2019

[66] A. Fuller, K. Millard, and J. Green, "Croma: Remote sensing representations with contrastive radar-optical masked autoencoders," in *Adv. Neural Inf. Process. Syst.*, ser. NeurIPS 2023, vol. 36. Curran Associates, Inc., 2023, pp. 5506–5538. [Online]. Available: https://proceedings.neurips.cc/paper_files/paper/2023/file/11822e84689e631615199db3b75cd0e4-Paper-Conference.pdf

[67] Y. Wang, C. M. Albrecht, and X. X. Zhu, "Multilabel-guided soft contrastive learning for efficient earth observation pretraining," *IEEE Trans. Geosci. Remote Sens.*, vol. 62, pp. 1–16, 2024. [Online]. Available: http://dx.doi.org/10.1109/tgrs.2024.3466896

[68] H. Bi, Y. Feng, B. Tong, M. Wang, H. Yu, Y. Mao, H. Chang, W. Diao, P. Wang, Y. Yu, H. Peng, Y. Zhang, K. Fu, and X. Sun, "Ringmoe: Mixture-of-modality-experts multi-modal foundation models for universal remote sensing image interpretation," *IEEE Trans. Pattern Anal. Mach. Intell.*, vol. 48, no. 4, pp. 4388–4405, Apr. 2026. [Online]. Available: http://dx.doi.org/10.1109/tpami.2025.3643453

[69] V. Nedungadi, A. Kariryaa, S. Oehmcke, S. Belongie, C. Igel, and N. Lang, "Mmearth: Exploring multi-modal pretext tasks for geospatial representation learning," in *Proc. Eur. Conf. Comput. Vis. (ECCV)*, A. Leonardis, E. Ricci, S. Roth, O. Russakovsky, T. Sattler, and G. Varol, Eds. Cham: Springer Nature Switzerland, 2025, pp. 164–182. [Online]. Available: http://dx.doi.org/10.1007/978-3-031-73039-9_10

[70] NASA Earthdata, "SRTM," https://www.earthdata.nasa.gov/data/instruments/srtm, 2024, accessed: Aug. 13, 2026.

[71] ——, "ASTER global digital elevation model V003," https://www.earthdata.nasa.gov/data/catalog/lpcloud-astgtm-003, 2025, accessed: Aug. 13, 2026.

[72] C3S, "ERA5 hourly data on single levels from 1940 to present," 2018. [Online]. Available: https://cds.climate.copernicus.eu/doi/10.24381/cds.adbb2d47

[73] J. Dollinger, D. Robert, E. Plekhanova, L. Drees, and J. D. Wegner, "Climplicit: Climatic implicit embeddings for global ecological tasks," in *ICLR Workshop Tackling Climate Change Mach. Learn.*, 2025. [Online]. Available: https://www.climatechange.ai/papers/iclr2025/44

[74] A. Toker, L. Kondmann, M. Weber, M. Eisenberger, A. Camero, J. Hu, A. Hoderlein, Ç. Şenaras, T. Davis, D. Cremers, G. Marchisio, X. X. Zhu, and L. Leal-Taixé, "Dynamicearthnet: Daily multi-spectral satellite dataset for semantic change segmentation," in *Proc. IEEE/CVF Conf. Comput. Vis. Pattern Recognit. (CVPR)*. IEEE, jun 2022, pp. 21 158–21 167. [Online]. Available: http://dx.doi.org/10.1109/cvpr52688.2022.02048

[75] A. Van Etten, D. Hogan, J. M. Manso, J. Shermeyer, N. Weir, and R. Lewis, "The multi-temporal urban development spacenet dataset," in *Proc. IEEE/CVF Conf. Comput. Vis. Pattern Recognit. (CVPR)*. IEEE, jun 2021, pp. 6398–6407. [Online]. Available: http://dx.doi.org/10.1109/cvpr46437.2021.00633

[76] N. Jean, S. Wang, A. Samar, G. Azzari, D. Lobell, and S. Ermon, "Tile2vec: Unsupervised representation learning for spatially distributed data," *Proc. AAAI Conf. Artif. Intell.*, vol. 33, no. 01, pp. 3967–3974, Jul. 2019. [Online]. Available: http://dx.doi.org/10.1609/aaai.v33i01.33013967

[77] F. Bastani, P. Wolters, R. Gupta, J. Ferdinando, and A. Kembhavi, "Satlaspretrain: A large-scale dataset for remote sensing image understanding," in *Proc. IEEE/CVF Int. Conf. Comput. Vis. (ICCV)*. IEEE, October 2023, pp. 16 772–16 782. [Online]. Available: https://openaccess.thecvf.com/content/ICCV2023/html/Bastani_SatlasPretrain_A_Large-Scale_Dataset_for_Remote_Sensing_Image_Understanding_ICCV_2023_paper.html

[78] J. Irvin, L. Tao, J. Zhou, Y. Ma, L. Nashold, B. Liu, and A. Y. Ng, "Usat: A unified self-supervised encoder for multi-sensor satellite imagery," 2023. [Online]. Available: https://arxiv.org/abs/2312.02199

[79] A. Meraner, P. Ebel, X. X. Zhu, and M. Schmitt, "Cloud removal in sentinel-2 imagery using a deep residual neural network and sar-optical data fusion," *ISPRS J. Photogramm. Remote Sens.*, vol. 166, pp. 333–346, Aug. 2020. [Online]. Available: http://dx.doi.org/10.1016/j.isprsjprs.2020.05.013

[80] C. Bodnar, W. P. Bruinsma, A. Lucic, M. Stanley, A. Allen, J. Brandstetter, P. Garvan, M. Riechert, J. A. Weyn, H. Dong, J. K. Gupta, K. Thambiratnam, A. T. Archibald, C.-C. Wu, E. Heider, M. Welling, R. E. Turner, and P. Perdikaris, "A foundation model for the earth system," *Nature*, vol. 641, no. 8065, pp. 1180–1187, May 2025. [Online]. Available: http://dx.doi.org/10.1038/s41586-025-09005-y

[81] J. Jakubik, F. Yang, B. Blumenstiel, E. Scheurer, R. Sedona, S. Maurogiovanni, J. Bosmans, N. Dionelis, V. Marsocci, N. Kopp, R. Ramachandran, P. Fraccaro, T. Brunschwiler, G. Cavallaro, J. Bernabe-Moreno, and N. Longépé, "Terramind: Large-scale generative multimodality for earth observation," in *Proc. IEEE/CVF Int. Conf. Comput. Vis. (ICCV)*. IEEE, Oct. 2025, pp. 7383–7394. [Online]. Available: http://dx.doi.org/10.1109/iccv51701.2025.00693

[82] N. Puriy, J. Jakubik, B. Blumenstiel, and K. Schindler, "Terraflow: Multimodal, multitemporal representation learning for earth observation," 2026. [Online]. Available: https://arxiv.org/abs/2603.12762

[83] C. J. Tucker, "Red and photographic infrared linear combinations for monitoring vegetation," *Remote Sens. Environ.*, vol. 8, no. 2, pp. 127–150, May 1979. [Online]. Available: http://dx.doi.org/10.1016/0034-4257(79)90013-0

[84] S. K. McFEETERS, "The use of the normalized difference water index (ndwi) in the delineation of open water features," *Int. J. Remote Sens.*, vol. 17, no. 7, pp. 1425–1432, May 1996. [Online]. Available: http://dx.doi.org/10.1080/01431169608948714

[85] Y. Zha, J. Gao, and S. Ni, "Use of normalized difference built-up index in automatically mapping urban areas from tm imagery," *Int. J. Remote Sens.*, vol. 24, no. 3, pp. 583–594, Jan. 2003. [Online]. Available: http://dx.doi.org/10.1080/01431160304987

[86] D. K. Hall, G. A. Riggs, V. V. Salomonson, N. E. DiGirolamo, and K. J. Bayr, "Modis snow-cover products," *Remote Sens. Environ.*, vol. 83, no. 1-2, pp. 181–194, Nov. 2002. [Online]. Available: http://dx.doi.org/10.1016/s0034-4257(02)00095-0

[87] R. M. Haralick, K. Shanmugam, and I. Dinstein, "Textural features for image classification," *IEEE Trans. Syst., Man, Cybern.*, vol. SMC-3, no. 6, pp. 610–621, Nov. 1973. [Online]. Available: http://dx.doi.org/10.1109/tsmc.1973.4309314

[88] T. Ojala, M. Pietikainen, and T. Maenpaa, "Multiresolution gray-scale and rotation invariant texture classification with local binary patterns," *IEEE Trans. Pattern Anal. Mach. Intell.*, vol. 24, no. 7, pp. 971–987, Jul. 2002. [Online]. Available: http://dx.doi.org/10.1109/tpami.2002.1017623

[89] L. Breiman, "Random forests," *Mach. Learn.*, vol. 45, no. 1, pp. 5–32, Oct. 2001. [Online]. Available: http://dx.doi.org/10.1023/a:1010933404324

[90] C. Cortes and V. Vapnik, "Support-vector networks," *Mach. Learn.*, vol. 20, no. 3, pp. 273–297, Sep. 1995. [Online]. Available: http://dx.doi.org/10.1007/bf00994018

[91] P. O. Gislason, J. A. Benediktsson, and J. R. Sveinsson, "Random forests for land cover classification," *Pattern Recognit. Lett.*, vol. 27, no. 4, pp. 294–300, Mar. 2006. [Online]. Available: http://dx.doi.org/10.1016/j.patrec.2005.08.011

[92] J. Deng, W. Dong, R. Socher, L.-J. Li, K. Li, and L. Fei-Fei, "Imagenet: A large-scale hierarchical image database," in *Proc. IEEE Conf. Comput. Vis. Pattern Recognit. (CVPR)*. IEEE, jun 2009, pp. 248–255. [Online]. Available: http://dx.doi.org/10.1109/cvpr.2009.5206848

[93] K. Simonyan and A. Zisserman, "Very deep convolutional networks for large-scale image recognition," in *Proc. Int. Conf. Learn. Represent. (ICLR)*, 2015. [Online]. Available: https://iclr.cc/archive/www/2015.html

[94] K. He, X. Zhang, S. Ren, and J. Sun, "Deep residual learning for image recognition," in *Proc. IEEE Conf. Comput. Vis. Pattern Recognit. (CVPR)*. IEEE, jun 2016, pp. 770–778. [Online]. Available: https://openaccess.thecvf.com/content_cvpr_2016/html/He_Deep_Residual_Learning_CVPR_2016_paper.html

[95] G. Cheng, J. Han, and X. Lu, "Remote sensing image scene classification: Benchmark and state of the art," *Proc. IEEE*, vol. 105, no. 10, pp. 1865–1883, Oct. 2017. [Online]. Available: http://dx.doi.org/10.1109/jproc.2017.2675998

[96] M. Volpi and D. Tuia, "Dense semantic labeling of subdecimeter resolution images with convolutional neural networks," *IEEE Trans. Geosci. Remote Sens.*, vol. 55, no. 2, pp. 881–893, Feb. 2017. [Online]. Available: http://dx.doi.org/10.1109/tgrs.2016.2616585

[97] S. Hochreiter and J. Schmidhuber, "Long short-term memory," *Neural Comput.*, vol. 9, no. 8, pp. 1735–1780, Nov. 1997. [Online]. Available: http://dx.doi.org/10.1162/neco.1997.9.8.1735

[98] A. Dosovitskiy, L. Beyer, A. Kolesnikov, D. Weissenborn, X. Zhai, T. Unterthiner, M. Dehghani, M. Minderer, G. Heigold, S. Gelly, J. Uszkoreit, and N. Houlsby, "An image is worth 16x16 words: Transformers for image recognition at scale," in *Proc. Int. Conf. Learn. Represent. (ICLR)*, 2021. [Online]. Available: https://openreview.net/forum?id=YicbFdNTTy

[99] M. Neumann, A. S. Pinto, X. Zhai, and N. Houlsby, "In-domain representation learning for remote sensing," in *ICLR*

2020 Workshop AI Earth Sci., 2020. [Online]. Available: https://ai4earthscience.github.io/iclr-2020-workshop/papers/ai4earth10.pdf

[100] O. Mañas, A. Lacoste, X. Giró-i Nieto, D. Vazquez, and P. Rodríguez, "Seasonal contrast: Unsupervised pre-training from uncurated remote sensing data," in *Proc. IEEE/CVF Int. Conf. Comput. Vis. (ICCV)*. IEEE, October 2021, pp. 9414–9423. [Online]. Available: https://openaccess.thecvf.com/content/ICCV2021/html/Manas_Seasonal_Contrast_Unsupervised_Pre-Training_From_Uncurated_Remote_Sensing_Data_ICCV_2021_paper.html

[101] Y. Wang, N. A. A. Braham, Z. Xiong, C. Liu, C. M. Albrecht, and X. X. Zhu, "Ssl4eo-s12: A large-scale multimodal, multitemporal dataset for self-supervised learning in earth observation [software and data sets]," *IEEE Geosci. Remote Sens. Mag.*, vol. 11, no. 3, pp. 98–106, Sep. 2023. [Online]. Available: http://dx.doi.org/10.1109/mgrs.2023.3281651

[102] X. Sun, P. Wang, W. Lu, Z. Zhu, X. Lu, Q. He, J. Li, X. Rong, Z. Yang, H. Chang, Q. He, G. Yang, R. Wang, J. Lu, and K. Fu, "Ringmo: A remote sensing foundation model with masked image modeling," *IEEE Trans. Geosci. Remote Sens.*, vol. 61, pp. 1–22, 2023. [Online]. Available: http://dx.doi.org/10.1109/tgrs.2022.3194732

[103] X. Guo, J. Lao, B. Dang, Y. Zhang, L. Yu, L. Ru, L. Zhong, Z. Huang, K. Wu, D. Hu, H. He, J. Wang, J. Chen, M. Yang, Y. Zhang, and Y. Li, "Skysense: A multi-modal remote sensing foundation model towards universal interpretation for earth observation imagery," in *Proc. IEEE/CVF Conf. Comput. Vis. Pattern Recognit. (CVPR)*. IEEE, June 2024, pp. 27 672–27 683. [Online]. Available: https://openaccess.thecvf.com/content/CVPR2024/html/Guo_SkySense_A_Multi-Modal_Remote_Sensing_Foundation_Model_Towards_Universal_Interpretation_CVPR_2024_paper.html

[104] O. Siméoni, H. V. Vo, M. Seitzer, F. Baldassarre, M. Oquab, C. Jose, V. Khalidov, M. Szafraniec, S. Yi, M. Ramamonjisoa, F. Massa, D. Haziza, L. Wehrstedt, J. Wang, T. Darcet, T. Moutakanni, L. Sentana, C. Roberts, A. Vedaldi, J. Tolan, J. Brandt, C. Couprie, J. Mairal, H. Jégou, P. Labatut, and P. Bojanowski, "DINOv3," *Trans. Mach. Learn. Res.*, 2026. [Online]. Available: https://openreview.net/forum?id=2NlGyqNjns

[105] Z. Feng, S. Jaffer, I. Shokar, J. Knezevic, M. Elvers, C. Atzberger, R. Young, A. Naik, N. Robinson, A. Blake, D. Coomes, A. Madhavapeddy, and S. Keshav, "Tessera v2: Scaling pixel-wise earth foundation models," 2026. [Online]. Available: https://arxiv.org/abs/2607.03949

[106] A. van den Oord, Y. Li, and O. Vinyals, "Representation learning with contrastive predictive coding," 2018. [Online]. Available: https://arxiv.org/abs/1807.03748

[107] U. Mall, B. Hariharan, and K. Bala, "Change-aware sampling and contrastive learning for satellite images," in *Proc. IEEE/CVF Conf. Comput. Vis. Pattern Recognit. (CVPR)*. IEEE, Jun. 2023, pp. 5261–5270. [Online]. Available: http://dx.doi.org/10.1109/cvpr52729.2023.00509

[108] J. Zbontar, L. Jing, I. Misra, Y. LeCun, and S. Deny, "Barlow twins: Self-supervised learning via redundancy reduction," in *Proc. Int. Conf. Mach. Learn. (ICML)*, ser. Proceedings of Machine Learning Research, M. Meila and T. Zhang, Eds., vol. 139. PMLR, 18–24 Jul 2021, pp. 12 310–12 320. [Online]. Available: https://proceedings.mlr.press/v139/zbontar21a.html

[109] Y. Wang, C. M. Albrecht, N. A. A. Braham, C. Liu, Z. Xiong, and X. X. Zhu, "Decoupling common and unique representations for multimodal self-supervised learning," in *Proc. Eur. Conf. Comput. Vis. (ECCV)*, A. Leonardis, E. Ricci, S. Roth, O. Russakovsky, T. Sattler, and G. Varol, Eds. Cham: Springer Nature Switzerland, 2025, pp. 286–303. [Online]. Available: http://dx.doi.org/10.1007/978-3-031-73397-0_17

[110] L. Waldmann, A. Shah, Y. Wang, N. Lehmann, A. Stewart, Z. Xiong, X. X. Zhu, S. Bauer, and J. Chuang, "Panopticon: Advancing any-sensor foundation models for earth observation," in *Proc. IEEE/CVF Conf. Comput. Vis. Pattern Recognit. Workshops (CVPRW)*. IEEE, jun 2025, pp. 2229–2239. [Online]. Available: https://openaccess.thecvf.com/content/CVPR2025W/EarthVision/html/Waldmann_Panopticon_Advancing_Any-Sensor_Foundation_Models_for_Earth_Observation_CVPRW_2025_paper.html

[111] M. Assran, Q. Duval, I. Misra, P. Bojanowski, P. Vincent, M. Rabbat, Y. LeCun, and N. Ballas, "Self-supervised learning from images with a joint-embedding predictive architecture," in *Proc. IEEE/CVF Conf. Comput. Vis. Pattern Recognit. (CVPR)*. IEEE, jun 2023, pp. 15 619–15 629. [Online]. Available: https://openaccess.thecvf.com/content/CVPR2023/html/Assran_Self-Supervised_Learning_From_Images_With_a_Joint-Embedding_Predictive_Architecture_CVPR_2023_paper.html

[112] G. Astruc, N. Gonthier, C. Mallet, and L. Landrieu, "Anysat: One earth observation model for many resolutions, scales, and modalities," in *Proc. IEEE/CVF Conf. Comput. Vis. Pattern Recognit. (CVPR)*. IEEE, Jun. 2025, pp. 19 530–19 540. [Online]. Available: http://dx.doi.org/10.1109/cvpr52734.2025.01819

[113] A. Radford, J. W. Kim, C. Hallacy, A. Ramesh, G. Goh, S. Agarwal, G. Sastry, A. Askell, P. Mishkin, J. Clark, G. Krueger, and I. Sutskever, "Learning transferable visual models from natural language supervision," in *Proc. Int. Conf. Mach. Learn. (ICML)*, ser. Proceedings of Machine Learning Research, M. Meila and T. Zhang, Eds., vol. 139. PMLR, 18–24 Jul 2021, pp. 8748–8763. [Online]. Available: https://proceedings.mlr.press/v139/radford21a.html

[114] F. Liu, D. Chen, Z. Guan, X. Zhou, J. Zhu, Q. Ye, L. Fu, and J. Zhou, "Remoteclip: A vision language foundation model for remote sensing," *IEEE Trans. Geosci. Remote Sens.*, vol. 62, pp. 1–16, 2024. [Online]. Available: http://dx.doi.org/10.1109/tgrs.2024.3390838

[115] U. Mall, C. P. Phoo, M. K. Liu, C. Vondrick, B. Hariharan, and K. Bala, "Remote sensing vision-language foundation models without annotations via ground remote alignment," in *Proc. Int. Conf. Learn. Represent. (ICLR)*, 2024. [Online]. Available: https://openreview.net/forum?id=w9tc699w3Z

[116] K. Heidler, L. Mou, D. Hu, P. Jin, G. Li, C. Gan, J.-R. Wen, and X. X. Zhu, "Self-supervised audiovisual representation learning for remote sensing data," *Int. J. Appl. Earth Obs. Geoinf.*, vol. 116, p. 103130, Feb. 2023. [Online]. Available: http://dx.doi.org/10.1016/j.jag.2022.103130

[117] A. Dhakal, A. Ahmad, S. Khanal, S. Sastry, H. Kerner, and N. Jacobs, "Sat2cap: Mapping fine-grained textual descriptions from satellite images," in *Proc. IEEE/CVF Conf. Comput. Vis. Pattern Recognit. Workshops (CVPRW)*. IEEE, Jun. 2024, pp. 533–542. [Online]. Available: http://dx.doi.org/10.1109/cvprw63382.2024.00058

[118] G. Tseng, A. Fuller, M. Reil, H. Herzog, P. Beukema, F. Bastani, J. R. Green, E. Shelhamer, H. Kerner, and D. Rolnick, "Galileo: Learning global & local features of many remote sensing modalities," in *Proc. Int. Conf. Mach. Learn. (ICML)*, ser. Proceedings of Machine Learning Research, A. Singh, M. Fazel, D. Hsu, S. Lacoste-Julien, F. Berkenkamp, T. Maharaj, K. Wagstaff, and J. Zhu, Eds., vol. 267. PMLR, 13–19 Jul 2025, pp. 60 280–60 300. [Online]. Available: https://proceedings.mlr.press/v267/tseng25a.html

[119] L. Jing, P. Vincent, Y. LeCun, and Y. Tian, "Understanding dimensional collapse in contrastive self-supervised learning," in *Proc. Int. Conf. Learn. Represent. (ICLR)*, 2022. [Online]. Available: https://openreview.net/forum?id=YevsQ05DEN7

[120] T. Wang and P. Isola, "Understanding contrastive representation learning through alignment and uniformity on the hypersphere," in *Proc. Int. Conf. Mach. Learn. (ICML)*, ser. Proceedings of Machine Learning Research, H. D. III and A. Singh, Eds., vol. 119. PMLR, 13–18 Jul 2020, pp. 9929–9939. [Online]. Available: https://proceedings.mlr.press/v119/wang20k.html

[121] V. W. Liang, Y. Zhang, Y. Kwon, S. Yeung, and J. Zou, "Mind the gap: Understanding the modality gap in multi-modal contrastive representation learning," in *Adv. Neural Inf. Process. Syst. 35*, ser. NeurIPS 2022. Neural Information Processing Systems Foundation, Inc. (NeurIPS), 2022, pp. 17 612–17 625. [Online]. Available: http://dx.doi.org/10.52202/068431-1280

[122] L. Betti, S. Ricke, I. Obadic, A. J. Stewart, and E. Rolf, "What's in an earth embedding? an explainability analysis of location encoders," 2026. [Online]. Available: https://arxiv.org/abs/2606.24997

[123] T. L. van der Plas, J. J. W. Bakermans, and I. N. Athanasiadis, "NeurEO: Dissecting earth observation embeddings with computational neuroscience," in *EurIPS Workshop Adv. Represent. Learn. Earth Observ.*, 2025. [Online]. Available: https://github.com/REO-workshop/2025-EurIPS-REO-workshop/blob/main/papers/NeurEO_Plas.pdf

[124] N. Tishby, F. C. Pereira, and W. Bialek, "The information bottleneck method," in *Proc. 37th Annu. Allerton Conf. Commun., Control, Comput.*, B. Hajek and R. S. Sreenivas, Eds., 1999, pp. 368–377. [Online]. Available: https://www.princeton.edu/~wbialek/our_papers/tishby+al_99.pdf

[125] A. Rao, M. Rußwurm, K. Klemmer, and E. Rolf, "Measuring the intrinsic dimension of earth representations," in *Proc. Int. Conf. Learn. Represent. (ICLR)*, 2026. [Online]. Available: https://openreview.net/forum?id=gQPD83DrGp

[126] I. T. Jolliffe, *Principal Component Analysis*, 2nd ed. Springer New York, 2002.

[127] H. Jégou, M. Douze, and C. Schmid, "Product quantization for nearest neighbor search," *IEEE Trans. Pattern Anal. Mach. Intell.*, vol. 33, no. 1, pp. 117–128, Jan. 2011. [Online]. Available: http://dx.doi.org/10.1109/tpami.2010.57

[128] G. Astruc, N. Gonthier, C. Mallet, and L. Landrieu, "Omnisat: Self-supervised modality fusion for earth observation," in *Proc.*

Eur. Conf. Comput. Vis. (ECCV), A. Leonardis, E. Ricci, S. Roth, O. Russakovsky, T. Sattler, and G. Varol, Eds. Cham: Springer Nature Switzerland, 2025, pp. 409–427. [Online]. Available: http://dx.doi.org/10.1007/978-3-031-73390-1_24

[129] B. Han, S. Zhang, X. Shi, and M. Reichstein, "Bridging remote sensors with multisensor geospatial foundation models," in *Proc. IEEE/CVF Conf. Comput. Vis. Pattern Recognit. (CVPR)*. IEEE, June 2024, pp. 27 852–27 862. [Online]. Available: http://dx.doi.org/10.1109/cvpr52733.2024.02631

[130] M. K. Do, K. Han, P. Lai, K. T. Phan, and W. Xiang, "Robsense: A robust multi-modal foundation model for remote sensing with static, temporal, and incomplete data adaptability," in *Proc. IEEE/CVF Conf. Comput. Vis. Pattern Recognit. (CVPR)*, Jun. 2025, pp. 7427–7436.

[131] Y. Zhang, L. Ru, K. Wu, L. Yu, L. Liang, Y. Li, and J. Chen, "Skysense v2: A unified foundation model for multi-modal remote sensing," in *Proc. IEEE/CVF Int. Conf. Comput. Vis. (ICCV)*. IEEE, oct 2025, pp. 9136–9146. [Online]. Available: https://openaccess.thecvf.com/content/ICCV2025/html/Zhang_SkySense_V2_A_Unified_Foundation_Model_for_Multi-modal_Remote_Sensing_ICCV_2025_paper.html

[132] X. Li, C. Li, G. Vivone, and D. Hong, "Seamo: A season-aware multimodal foundation model for remote sensing," *Inf. Fusion*, vol. 125, p. 103334, Jan. 2026. [Online]. Available: http://dx.doi.org/10.1016/j.inffus.2025.103334

[133] X. Qin, D. Wang, J. Zhang, F. Wang, X. Su, B. Du, and L. Zhang, "Timo: Spatiotemporal foundation model for satellite image time series," 2025. [Online]. Available: https://arxiv.org/abs/2505.08723

[134] M. S. Danish, M. A. Munir, S. R. A. Shah, M. H. Khan, R. M. Anwer, J. Laaksonen, F. S. Khan, and S. Khan, "Terrafm: A scalable foundation model for unified multisensor earth observation," in *Proc. Int. Conf. Learn. Represent. (ICLR)*, 2026. [Online]. Available: https://openreview.net/forum?id=cBxuzdUDNx

[135] L. Bai, X. Zhang, S. Zhang, Z. Zhang, X. Wang, Z. Yang, R. Huang, Y. Zhang, Y. Zhang, D. Wang, J. Wang, and W. Wang, "GeoLink: Empowering remote sensing foundation model with OpenStreetMap data," in *Adv. Neural Inf. Process. Syst.*, D. Belgrave, C. Zhang, H. Lin, R. Pascanu, P. Koniusz, M. Ghassemi, and N. Chen, Eds., vol. 38. Curran Associates, Inc., 2025, pp. 168 557–168 587. [Online]. Available: https://proceedings.neurips.cc/paper_files/paper/2025/file/f681209306654a0c1f690f65810e8e45-Paper-Conference.pdf

[136] K. Ayush, B. Uzkent, C. Meng, K. Tanmay, M. Burke, D. Lobell, and S. Ermon, "Geography-aware self-supervised learning," in *Proc. IEEE/CVF Int. Conf. Comput. Vis. (ICCV)*. IEEE, oct 2021, pp. 10 181–10 190. [Online]. Available: http://dx.doi.org/10.1109/iccv48922.2021.01002

[137] Earth Genome, "Earth Index Embeddings," Source Cooperative, 2025. [Online]. Available: https://source.coop/earthgenome/earthindexembeddings

[138] Copernicus Data Space Ecosystem, "Global embedding dataset now available on CDSE," https://dataspace.copernicus.eu/news/2025-11-14-global-embedding-dataset-now-available-cdse, 2025, accessed: Jul. 30, 2026.

[139] F. Mentzer, D. Minnen, E. Agustsson, and M. Tschannen, "Finite scalar quantization: Vq-vae made simple," in *Proc. Int. Conf. Learn. Represent. (ICLR)*, 2024. [Online]. Available: https://openreview.net/forum?id=8ishA3LxN8

[140] G. Mai, N. Lao, Y. He, J. Song, and S. Ermon, "CSP: Self-supervised contrastive spatial pre-training for geospatial-visual representations," in *Proc. Int. Conf. Mach. Learn. (ICML)*, ser. Proceedings of Machine Learning Research, A. Krause, E. Brunskill, K. Cho, B. Engelhardt, S. Sabato, and J. Scarlett, Eds., vol. 202. PMLR, 23–29 Jul 2023, pp. 23 498–23 515. [Online]. Available: https://proceedings.mlr.press/v202/mai23a.html

[141] M. Czerkawski, M. Kluczek, and J. S. Bojanowski, "Core-S2RGB-DINOv2," Hugging Face Datasets, https://huggingface.co/datasets/Major-TOM/Core-S2RGB-DINOv2, 2025.

[142] X. Zhai, B. Mustafa, A. Kolesnikov, and L. Beyer, "Sigmoid loss for language image pre-training," in *Proc. IEEE/CVF Int. Conf. Comput. Vis. (ICCV)*. IEEE, October 2023, pp. 11 975–11 986. [Online]. Available: http://dx.doi.org/10.1109/iccv51070.2023.01100

[143] M. Czerkawski, M. Kluczek, and J. S. Bojanowski, "Core-S2RGB-SigLIP," Hugging Face Datasets, https://huggingface.co/datasets/Major-TOM/Core-S2RGB-SigLIP, 2025.

[144] Y. Wang, Z. Xiong, C. Liu, A. J. Stewart, T. Dujardin, N. I. Bountos, A. Zavras, F. Gerken, I. Papoutsis, L. Leal-Taixé, and X. X. Zhu, "Copernicus-Embed-025deg," GitHub repository, https://github.com/zhu-xlab/Copernicus-FM/tree/main/Copernicus-Embed-025deg, 2025.

[145] Z. Zhang, T. Zhao, Y. Guo, and J. Yin, "Rs5m and georsclip: A large-scale vision- language dataset and a large vision-language model for remote sensing," *IEEE Trans. Geosci. Remote Sens.*, vol. 62, pp. 1–23, 2024. [Online]. Available: http://dx.doi.org/10.1109/tgrs.2024.3449154

[146] Z. Wang, R. Prabha, T. Huang, J. Wu, and R. Rajagopal, "Skyscript: A large and semantically diverse vision-language dataset for remote sensing," *Proc. AAAI Conf. Artif. Intell.*, vol. 38, no. 6, pp. 5805–5813, Mar. 2024. [Online]. Available: http://dx.doi.org/10.1609/aaai.v38i6.28393

[147] D. Ye, D. Kiv, W. Hu, J. Shi, and S. Wang, "Any model, any place, any time: Get remote sensing foundation model embeddings on demand," 2026. [Online]. Available: https://arxiv.org/abs/2602.23678

[148] CyberGIS Center, "rs-embed," GitHub repository, https://github.com/cybergis/rs-embed, 2026, version 0.2.1; accessed Jul. 30, 2026. [Online]. Available: https://github.com/cybergis/rs-embed/releases/tag/v0.2.1

[149] G. Mai, K. Janowicz, B. Yan, R. Zhu, L. Cai, and N. Lao, "Multi-scale representation learning for spatial feature distributions using grid cells," in *Proc. Int. Conf. Learn. Represent. (ICLR)*, 2020. [Online]. Available: https://iclr.cc/virtual_2020/poster_rJljdh4KDH.html

[150] G. Mai, Y. Xuan, W. Zuo, Y. He, J. Song, S. Ermon, K. Janowicz, and N. Lao, "Sphere2vec: A general-purpose location representation learning over a spherical surface for large-scale geospatial predictions," *ISPRS J. Photogramm. Remote Sens.*, vol. 202, pp. 439–462, Aug. 2023. [Online]. Available: http://dx.doi.org/10.1016/j.isprsjprs.2023.06.016

[151] M. Rußwurm, K. Klemmer, E. Rolf, R. Zbinden, and D. Tuia, "Geographic location encoding with spherical harmonics and sinusoidal representation networks," in *Proc. Int. Conf. Learn. Represent. (ICLR)*, 2024. [Online]. Available: https://proceedings.iclr.cc/paper_files/paper/2024/hash/073c8584ef86bee26fe9d639ec648e28-Abstract-Conference.html

[152] A. Rao, R. Crasto, T. Ooms, D. Rolnick, K. Klemmer, and M. Rußwurm, "Localized, high-resolution geographic representations with slepian functions," in *Proc. Int. Conf. Mach. Learn. (ICML)*, 2026. [Online]. Available: https://icml.cc/virtual/2026/poster/62670

[153] E. Cole, G. V. Horn, C. Lange, A. Shepard, P. Leary, P. Perona, S. Loarie, and O. Mac Aodha, "Spatial implicit neural representations for global-scale species mapping," in *Proc. Int. Conf. Mach. Learn. (ICML)*, ser. Proceedings of Machine Learning Research, A. Krause, E. Brunskill, K. Cho, B. Engelhardt, S. Sabato, and J. Scarlett, Eds., vol. 202. PMLR, 23–29 Jul 2023, pp. 6320–6342. [Online]. Available: https://proceedings.mlr.press/v202/cole23a.html

[154] D. Cher, H. Iqbal, E. Xing, B. Wei, and N. Jacobs, "Tessellating the earth: Learnable spherical voronoi partitions for location encoding," in *Proc. Eur. Conf. Comput. Vis. (ECCV)*, 2026. [Online]. Available: https://arxiv.org/abs/2606.27514

[155] X. Hao, W. Chen, X. Zou, and Y. Liang, "Nature makes no leaps: Building continuous location embeddings with satellite imagery from the web," in *Proc. ACM Web Conf. (WWW)*, ser. WWW '25. ACM, Apr. 2025, pp. 2799–2812. [Online]. Available: http://dx.doi.org/10.1145/3696410.3714629

[156] S. Choudhury, C. Suvarna, I. Tsogsuren, A. R. Kreidieh, E. Aharoni, C.-T. Lu, and N. Arora, "S2vec: Self-supervised geospatial embeddings for the built environment," *ACM Trans. Spatial Algorithms Syst.*, vol. 12, no. 3, pp. 1–21, May 2026. [Online]. Available: http://dx.doi.org/10.1145/3787217

[157] Y. Wen, J. Cai, Q. Ma, L. Li, X. Chen, C. Webster, and Y. Zhou, "MoRA: Mobility as the backbone for geospatial representation learning at scale," in *Proc. Int. Conf. Learn. Represent. (ICLR)*, 2026. [Online]. Available: https://openreview.net/forum?id=IlBr5JJsCj

[158] D. Michail, E. Saka, I. Giannopoulos, and I. Papoutsis, "Osmgraphclip: Learning global location representations from openstreetmap graphs," 2026. [Online]. Available: https://arxiv.org/abs/2606.08046

[159] G. Astruc, E. Trulls, J. Hosang, L. Landrieu, and P.-E. Sarlin, "Unigeoclip: Unified geospatial contrastive learning," in *Proc. IEEE/CVF Conf. Comput. Vis. Pattern Recognit. Workshops (CVPRW)*, Jun. 2026, pp. 7847–7856.

[160] Z. Liu, N. Lao, Z. Wang, J. Jiao, and G. Mai, "Gair: Location-aware self-supervised contrastive pre-training with geo-aligned implicit representations," *ISPRS J. Photogramm. Remote Sens.*, vol. 237, pp. 166–182, Jul. 2026. [Online]. Available: http://dx.doi.org/10.1016/j.isprsjprs.2026.04.035

[161] A. Dhakal, S. Sastry, S. Khanal, A. Ahmad, E. Xing, and N. Jacobs, "Range: Retrieval augmented neural fields for multi-resolution geo-embeddings," in *Proc. IEEE/CVF Conf. Comput. Vis. Pattern Recognit. (CVPR)*. IEEE, Jun. 2025, pp. 24 680–24 689. [Online]. Available: http://dx.doi.org/10.1109/cvpr52734.2025.02298

[162] Z. Wang, K. Lane, L. Cai, M. Karimzadeh, and E. Rolf, "A proxy consistency loss for grounded fusion of Earth observation and location encoders," in *Proc. IEEE/CVF Conf. Comput. Vis. Pattern Recognit. Workshops (CVPRW)*, Jun. 2026. [Online]. Available: https://arxiv.org/abs/2604.18881

[163] N. Wu, Q. Cao, Z. Wang, Z. Liu, Y. Qi, J. Zhang, J. Ni, X. Yao, H. Ma, L. Mu, S. Ermon, T. Ganu, A. Nambi, N. Lao, and G. Mai, "Torchspatial: A location encoding framework and benchmark for spatial representation learning," in *Adv. Neural Inf. Process. Syst.*, vol. 37. Curran Associates, Inc., 2024, pp. 81 437–81 460. [Online]. Available: https://proceedings.neurips.cc/paper_files/paper/2024/file/9449c2d5b0cc8c9a445752f3ff195a1c-Paper-Datasets_and_Benchmarks_Track.pdf

[164] M. Tom, Y. Jiang, E. Baltsavias, and K. Schindler, "Learning a joint embedding of multiple satellite sensors: A case study for lake ice monitoring," *IEEE Trans. Geosci. Remote Sens.*, vol. 60, pp. 1–15, 2022. [Online]. Available: http://dx.doi.org/10.1109/tgrs.2022.3211184

[165] M. Tarasiou and S. Zafeiriou, "Embedding earth: Self-supervised contrastive pre-training for dense land cover classification," 2022. [Online]. Available: https://arxiv.org/abs/2203.06041

[166] M. J. Smith, L. Fleming, and J. Geach, "Earthpt: a foundation model for earth observation," in *NeurIPS 2023 Workshop Tackling Climate Change Mach. Learn.*, 2023. [Online]. Available: https://www.climatechange.ai/papers/neurips2023/2

[167] M. Allen, F. Dorr, J. A. Gallego-Mejia, L. Martínez-Ferrer, A. Jungbluth, F. Kalaitzis, and R. Ramos-Pollán, "Fewshot learning on global multimodal embeddings for earth observation tasks," in *NeurIPS 2023 R0-FoMo Workshop*, 2023. [Online]. Available: https://arxiv.org/abs/2310.00119

[168] B. Blumenstiel, V. Moor, R. Kienzler, and T. Brunschwiler, "Multi-spectral remote sensing image retrieval using geospatial foundation models," in *Proc. IEEE Int. Geosci. Remote Sens. Symp. (IGARSS)*. IEEE, Jul. 2024, pp. 7286–7291. [Online]. Available: http://dx.doi.org/10.1109/igarss53475.2024.10641903

[169] C. Gomes and T. Brunschwiler, "Neural embedding compression for efficient multi-task earth observation modelling," in *Proc. IEEE Int. Geosci. Remote Sens. Symp. (IGARSS)*. IEEE, Jul. 2024, pp. 8268–8273. [Online]. Available: http://dx.doi.org/10.1109/igarss53475.2024.10642535

[170] Y. Glaser, J. E. Stopa, L. M. Wolniewicz, R. Foster, D. Vandemark, A. Mouche, B. Chapron, and P. Sadowski, "Wv-net: A foundation model for sar ocean satellite imagery," *Artif. Intell. Earth Syst.*, vol. 4, no. 4, Oct. 2025. [Online]. Available: http://dx.doi.org/10.1175/aies-d-25-0003.1

[171] P. Ravirathinam, A. Parthasarathy, A. Khandelwal, R. Ghosh, and V. Kumar, "Towards knowledge guided pretraining approaches for multimodal foundation models: Applications in remote sensing," *ACM Trans. Spatial Algorithms Syst.*, Mar. 2026. [Online]. Available: http://dx.doi.org/10.1145/3806229

[172] A. Jha, M. Singha, A. Bhattacharya, and B. Banerjee, "RS^{3}Lip: Consistency for remote sensing image classification on part embeddings using self-supervised learning and CLIP," *Comput. Vis. Image Underst.*, vol. 251, p. 104254, Feb. 2025. [Online]. Available: http://dx.doi.org/10.1016/j.cviu.2024.104254

[173] I. Dumeur, S. Valero, and J. Inglada, "Paving the way toward foundation models for irregular and unaligned satellite image time series," *IEEE Trans. Geosci. Remote Sens.*, vol. 63, pp. 1–21, 2025. [Online]. Available: http://dx.doi.org/10.1109/tgrs.2025.3589013

[174] I. Fayad, M. Zimmer, M. Schwartz, F. Gieseke, P. Ciais, G. Belouze, S. Brood, A. De Truchis, and A. D'Aspremont, "DUNIA: Pixel-sized embeddings via cross-modal alignment for earth observation applications," in *Proc. Int. Conf. Mach. Learn. (ICML)*, ser. Proceedings of Machine Learning Research, A. Singh, M. Fazel, D. Hsu, S. Lacoste-Julien, F. Berkenkamp, T. Maharaj, K. Wagstaff, and J. Zhu, Eds., vol. 267. PMLR, 13–19 Jul 2025, pp. 16 375–16 406. [Online]. Available: https://proceedings.mlr.press/v267/fayad25a.html

[175] S. Choudhury, Y. Salunkhe, S. Mehrotra, and B. Banerjee, "Rejepa: A novel joint-embedding predictive architecture for efficient remote sensing image retrieval," in *Proc. IEEE/CVF Conf. Comput. Vis. Pattern Recognit. Workshops (CVPRW)*. IEEE, Jun. 2025, pp. 2364–2373. [Online]. Available: http://dx.doi.org/10.1109/cvprw67362.2025.00223

[176] Q. Zhang, D. Wang, and X. Yu, "Rlita: A region-level image–text alignment method for remote sensing foundation model," *Remote Sens.*, vol. 17, no. 10, p. 1661, May 2025. [Online]. Available: http://dx.doi.org/10.3390/rs17101661

[177] T. Han, H. Chen, C. Wang, Y. Ren, and M. Wu, "Towards a new era of geo-foundation models: Expert-guided multimodal alignment and geospatial context awareness," in *Proc. 33rd ACM SIGSPATIAL Int. Conf. Adv. Geographic Inf. Syst.*, ser. SIGSPATIAL '25. ACM, Nov. 2025, pp. 454–465. [Online]. Available: http://dx.doi.org/10.1145/3748636.3762756

[178] R. Ji, X. Wang, C. Niu, W. Zhang, Y. Mei, and K. Tan, "Specaware: a spectral-content aware foundation model for unifying multi-sensor learning in hyperspectral remote sensing mapping," *ISPRS J. Photogramm. Remote Sens.*, vol. 234, pp. 242–260, Apr. 2026. [Online]. Available: http://dx.doi.org/10.1016/j.isprsjprs.2026.02.024

[179] M. Gonzalez-Calabuig, K.-H. Cohrs, V. Nedungadi, Z. Osika, R. Cartuyvels, S. Knoblauch, J. Massant, S. Nath, P. Ebel, and V. Sitokonstantinou, "Shrug-fm: Reliability-aware foundation models for earth observation," in *Proc. IEEE/CVF Conf. Comput. Vis. Pattern Recognit. Workshops (CVPRW)*, Jun. 2026, pp. 7919–7928. [Online]. Available: https://openaccess.thecvf.com/content/CVPR2026W/EarthVision/html/Gonzalez-Calabuig_SHRUG-FM_Reliability-Aware_Foundation_Models_for_Earth_Observation_CVPRW_2026_paper.html

[180] E. S. Aimar, G. Zhambulova, F. S. Khan, Y. Xu, and M. Felsberg, "Vlm2geovec: Toward universal multimodal embeddings for remote sensing," 2025. [Online]. Available: https://arxiv.org/abs/2512.11490

[181] Z. Xu, R. Tang, M. Bianco, Q. Zhang, R. Madhok, N. Karianakis, and F. Yu, "Geospatial foundational embedder: Top-1 winning solution on earthvision embed2scale challenge (cvpr 2025)," 2025. [Online]. Available: https://arxiv.org/abs/2509.06993

[182] R. Vinge, I. Wittmann, J. Schneider, M. Marszalek, L. Gilch, T. Brunschwiler, and C. M. Albrecht, "Neuco-bench: A novel benchmark framework for neural embeddings in earth observation," in *Proc. IEEE/CVF Conf. Comput. Vis. Pattern Recognit. Workshops (CVPRW)*, Jun. 2026, pp. 8063–8074.

[183] V. Marsocci, Y. Jia, G. L. Bellier, D. Kerekes, L. Zeng, S. Hafner, S. Gerard, E. Brune, R. Yadav, A. Shibli, H. Fang, Y. Ban, M. Vergauwen, N. Audebert, and A. Nascetti, "Pangaea: Assessing geospatial foundation models capabilities through a global and inclusive benchmark," *IEEE Geosci. Remote Sens. Mag.*, vol. 14, no. 1, pp. 245–285, Feb. 2026. [Online]. Available: http://dx.doi.org/10.1109/mgrs.2025.3628194

[184] I. Corley, C. Robinson, I. Becker-Reshef, and J. M. L. Ferres, "From pixels to patches: Pooling strategies for earth embeddings," in *ICLR 2026 Workshop Mach. Learn. Remote Sens.*, 2026. [Online]. Available: https://openreview.net/forum?id=oPfOVLFIrU

[185] T. L. van der Plas, J. J. Bakermans, V. Nedungadi, G. Tijūnaitytė, M. Rußwurm, and I. N. Athanasiadis, "Better together: Evaluating the complementarity of earth embedding models," 2026. [Online]. Available: https://arxiv.org/abs/2605.18667

[186] H. Khan and A. Ahmad, "Evaluating alphaearth foundation embeddings for pixel- and object-based land cover classification in google earth engine," Nov. 2025. [Online]. Available: http://dx.doi.org/10.20944/preprints202511.2172.v1

[187] S. Mantey, I. S. Attipoe, and A. Alhassan, "A comparative analysis of satellite imagery for land cover classification: Evaluating google satellite embeddings, sentinel-2, and landsat-8 data with xgboost," Dec. 2025. [Online]. Available: http://dx.doi.org/10.21203/rs.3.rs-7961146/v1

[188] D. K. Dalei, S. Shrivastava, and N. Panigrahi, "Geographic places to semantic spaces: Analysis of geospatial embeddings," *ISPRS Ann. Photogramm. Remote Sens. Spatial Inf. Sci.*, vol. X-5/W2-2025, pp. 131–135, Dec. 2025. [Online]. Available: http://dx.doi.org/10.5194/isprs-annals-x-5-w2-2025-131-2025

[189] Y. Ma, Y. Shen, A. Swatantran, and D. B. Lobell, "Harvesting alphaearth: Benchmarking the geospatial foundation model for agricultural downstream tasks," *Int. J. Appl. Earth Obs. Geoinf.*, vol. 149, p. 105258, May 2026. [Online]. Available: http://dx.doi.org/10.1016/j.jag.2026.105258

[190] S. Mantey, I. S. K. Attipoe, and J. K. Lawerteh, "Boosting algorithm: An ensemble learning tool for land use land cover classification using google alpha earth foundations satellite embeddings," *Adv. Remote Sens.*, vol. 15, no. 01, pp. 1–22, 2026. [Online]. Available: http://dx.doi.org/10.4236/ars.2026.151001

[191] Z. Feng, C. Atzberger, S. Jaffer, J. Knezevic, S. Sormunen, R. Young, M. Lisaius, M. Immitzer, T. Jackson, J. Ball, D. Coomes, A. Madhavapeddy, A. Blake, and S. Keshav, "Applications of the tessera geospatial foundation model to diverse environmental mapping tasks," 2026. [Online]. Available: http://dx.doi.org/10.2139/ssrn.6142416

[192] M. G. Frasch, "Reducing intersectional disparities in postpartum depression screening through geospatial foundation model embeddings:

A cross-sectional study of 209,872 us women," 2026. [Online]. Available: http://dx.doi.org/10.2139/ssrn.6311855

[193] K. Lee-Burkhart, Y. Hatanaka, P. Sadowski, and Q. Chen, "Geospatial foundation model embeddings improve land surface temperature recovery in the hawaiian islands," 2026. [Online]. Available: http://dx.doi.org/10.2139/ssrn.6462445

[194] Y. J. E. Gbodjo and D. Ienco, "Assessing the generalization of geospatial embeddings for temporaltransfer in land cover classification," 2026. [Online]. Available: http://dx.doi.org/10.2139/ssrn.6890917

[195] M.-H. Kim and H.-M. Park, "Cosmo: Contrastive satellite image embedding techniques reflecting expert weather bulletins," *IEEE Access*, vol. 14, pp. 92 385–92 398, 2026. [Online]. Available: http://dx.doi.org/10.1109/access.2026.3702845

[196] S. Li, Y. He, D. Yang, Y. Li, and W. Liu, "Incorporating learned geospatial embeddings to deep image prior for inpainting cloud areas in remotely sensed images," *Sci. Remote Sens.*, vol. 13, p. 100404, Jun. 2026. [Online]. Available: http://dx.doi.org/10.1016/j.srs.2026.100404

[197] S. Sim, "Embedding-only uplink for onboard retrieval under shift in remote sensing," *IEEE Geosci. Remote Sens. Lett.*, vol. 23, p. 8500205, 2026. [Online]. Available: http://dx.doi.org/10.1109/lgrs.2026.3718430

[198] J. Lyu, M. Yang, J. Cai, Y. Hu, G. Lu, J. Qiu, and R. Dong, "Structure-semantic decoupled modulation of global geospatial embeddings for high-resolution remote sensing mapping," 2026. [Online]. Available: https://arxiv.org/abs/2604.19591

[199] P. Du, L. Cui, Y. Lian, H. Li, J. Fan, X. Zhou, and Y. Chen, "Global inversion of terrestrial net ecosystem exchange: Integrating explicit multi-source predictors and high-dimensional remote-sensing embeddings," *Remote Sens.*, vol. 18, no. 9, p. 1390, Apr. 2026. [Online]. Available: http://dx.doi.org/10.3390/rs18091390

[200] H. Park, M. Seo, and D.-G. Choi, "Rethinking electro-optical vision foundation models for remote sensing retrieval: A controlled comparison with generalist vfm," 2026. [Online]. Available: https://arxiv.org/abs/2605.02283

[201] J. Walsh, W. Fawcett, G. Colvard, and R. Ramos-Pollán, "Zero-shot satellite image retrieval through joint embeddings: Application to crisis response," May 2026. [Online]. Available: http://dx.doi.org/10.56272/a2c9ee39

[202] M. A. Arefeen, B. Debnath, R. K. Rajendran, M. Sankaradas, and S. T. Chakradhar, "Open-sat: Llm-guided query embedding refinement for open-vocabulary object retrieval in satellite imagery," 2026. [Online]. Available: https://arxiv.org/abs/2605.05344

[203] D. Johnson, "Calibrated spatial uncertainty for earth observation foundation models via matérn-motivated latent stochastic regularization," May 2026. [Online]. Available: http://dx.doi.org/10.31223/x5rx9z

[204] K. Zheng, G. He, R. Yin, and G. Wang, "Seed-driven grid adaptation method: A prior-guided active learning framework for impervious surface mapping on the qinghai–xizang plateau using google satellite embeddings," *Remote Sens.*, vol. 18, no. 10, p. 1596, May 2026. [Online]. Available: http://dx.doi.org/10.3390/rs18101596

[205] M. A. Hossain, A. V. Patel, S. K. Singh, and B. Banerjee, "Hq-jepa: Hybrid quantum joint-embedding predictive architecture for cross-modal remote sensing representation learning," 2026. [Online]. Available: https://arxiv.org/abs/2605.31068

[206] M. A. Hossain, A. V. Patel, N. Dube, and B. Banerjee, "Cr-jepa: Cross-modal joint-embedding predictive learning for remote sensing image retrieval," 2026. [Online]. Available: https://arxiv.org/abs/2606.00706

[207] S. Knoblauch, H. Li, G. Mai, K. Klemmer, S. Gao, and W. Li, "Spatial representation learning beyond pixels: Unifying raster data and vector semantics for human-centric geospatial foundation models," 2026. [Online]. Available: https://arxiv.org/abs/2606.02374

[208] M. B. Joseph, F. D. S. Mendes, D. M. T. Nguyen, C. Sothe, and C. B. Anderson, "Continuous biome representations from earth observation embeddings," 2026. [Online]. Available: https://arxiv.org/abs/2606.11510

[209] J. Kumari and A. S. Singh, "emem: A research on content-addressed, verifiable earth-memory protocol for ai agents over foundation-model embeddings," 2026. [Online]. Available: https://zenodo.org/doi/10.5281/zenodo.20706893

[210] J. Han, B. Zhang, X. Sun, Q. Zhang, Y. Dong, D. Lu, C. Hu, L. Yang, F. Zhang, Y. Wei, and J. Guo, "Fusionrs: A large-scale rgb-infrared-style remote sensing dataset for cross-modal vision-language learning," 2026. [Online]. Available: https://arxiv.org/abs/2606.17020

[211] J. Hecht, L. Arzoumanidis, Z. Li, and Y. Dehbi, "Multi-modal contrastive learning for implicit earth embeddings via location tying," 2026. [Online]. Available: https://arxiv.org/abs/2606.20167

[212] L. Silva and J. Gonçalves, "Evaluating alphaearth and tessera geospatial embeddings for machine learning-based burned area mapping in portugal," 2026. [Online]. Available: https://zenodo.org/doi/10.5281/zenodo.21252157

[213] C. I. Alvarez, P. Schneider, and M. Wurm, "Evaluating geospatial foundation-model embeddings for tropomi-based annual surface no2 estimation across europe," Jul. 2026. [Online]. Available: http://dx.doi.org/10.22541/essoar.15005949/v1

[214] Biswanath Das, Pranab Dhara, and Vijender Kumar, "Identification of major kharif paddy growing areas in india- using msi data ,google satellite embedding and advanced machine learning," 2026. [Online]. Available: https://www.researchgate.net/doi/10.13140/RG.2.2.22893.96485

[215] Google Earth Engine, "AlphaEarth Foundations GCS data," Official documentation, https://developers.google.com/earth-engine/guides/aef_on_gcs_readme, 2026, accessed: Jul. 30, 2026.

[216] Cambridge Centre for Earth Observation, "GeoTessera," GitHub repository, https://github.com/ucam-eo/geotessera, 2026, accessed: Jul. 30, 2026.

[217] L. Hackel, T. Burgert, and B. Demir, "How much of a model do we need? redundancy and slimmability in remote sensing foundation models," 2026. [Online]. Available: https://arxiv.org/abs/2601.22841

[218] M. C. Lisaius, S. Keshav, A. Blake, and C. Atzberger, "Embedding-based crop type classification in the groundnut basin of senegal," 2026. [Online]. Available: https://arxiv.org/abs/2601.16900

[219] Copernicus Data Space Ecosystem, "Global embeddings dataset," Official documentation, https://documentation.dataspace.copernicus.eu/Data/ComplementaryData/Embeddings.html, 2026, accessed: Jul. 30, 2026.

[220] Major TOM, "Major TOM: Expandable datasets for earth observation," Hugging Face, https://huggingface.co/Major-TOM, 2026, accessed: Jul. 30, 2026.

[221] Source Cooperative, "Source cooperative documentation," https://docs.source.coop/, 2026, accessed: Jul. 30, 2026.

[222] LGND AI, "LGND developer documentation: Getting started guide," https://lgnd.ai/lgnd-docs, 2026, accessed: 2026-08-02.

[223] ——, "LGND support," https://lgnd.ai/support, 2026, accessed: 2026-08-02.

[224] Geo-Embeddings, "Best practices — Geo-Embeddings," https://geoembeddings.org/bestpractices.html, 2026, accessed: 2026-08-02.

[225] ——, "Standards — Geo-Embeddings," https://geoembeddings.org/standards.html, 2026, accessed: 2026-08-02.

[226] Cambridge Centre for Earth Observation, "GeoTessera documentation," https://geotessera.readthedocs.io/en/latest/, 2026, accessed: Jul. 30, 2026.

[227] A. J. Stewart, C. Robinson, I. A. Corley, A. Ortiz, J. M. L. Ferres, and A. Banerjee, "Torchgeo: deep learning with geospatial data," in *Proc. 30th ACM SIGSPATIAL Int. Conf. Adv. Geographic Inf. Syst.*, ser. SIGSPATIAL '22. ACM, Nov. 2022, pp. 1–12. [Online]. Available: http://dx.doi.org/10.1145/3557915.3560953

[228] TorchGeo, "TorchGeo v0.9.0," GitHub release, https://github.com/torchgeo/torchgeo/releases/tag/v0.9.0, 2026, accessed: Jul. 30, 2026.

[229] C. Gomes, B. Blumenstiel, J. L. De Sousa Almeida, P. H. De Oliveira, P. Fraccaro, F. M. Escofet, D. Szwarcman, N. Simumba, R. Kienzler, and B. Zadrozny, "Terratorch: The geospatial foundation models toolkit," in *Proc. IEEE Int. Geosci. Remote Sens. Symp. (IGARSS)*. IEEE, Aug. 2025, pp. 6364–6368. [Online]. Available: http://dx.doi.org/10.1109/igarss55030.2025.11243570

[230] Q. Wu, "Geoai: A python package for integrating artificial intelligence with geospatial data analysis and visualization," *J. Open Source Softw.*, vol. 11, no. 118, p. 9605, Feb. 2026. [Online]. Available: http://dx.doi.org/10.21105/joss.09605

[231] OpenGeoAI, "embeddings module - GeoAI," https://opengeoai.org/embeddings/, 2026, accessed: 2026-08-02.

[232] ——, "Foundation models - GeoAI," https://opengeoai.org/foundation_models/, 2026, accessed: 2026-08-02.

[233] P. Gramacki, K. Leśniara, K. Raczycki, S. Woźniak, M. Przymus, and P. Szymański, "Srai: Towards standardization of geospatial ai," in *Proc. 6th ACM SIGSPATIAL Int. Workshop AI Geographic Knowl. Discovery*, ser. SIGSPATIAL '23. Association for Computing Machinery, November 2023, pp. 43–52. [Online]. Available: https://dl.acm.org/doi/10.1145/3615886.3627740

[234] Kraina AI, "Spatial representations for artificial intelligence (srai)," https://kraina-ai.github.io/srai/latest/, 2026, accessed: 2026-08-02.

[235] I. Dimitrovski, I. Kitanovski, P. Panov, A. Kostovska, N. Simidjievski, and D. Kocev, "Aitlas: Artificial intelligence toolbox for earth

observation," *Remote Sens.*, vol. 15, no. 9, p. 2343, Apr. 2023. [Online]. Available: http://dx.doi.org/10.3390/rs15092343

[236] Bias Variance Labs, "AiTLAS 2.0," GitHub repository, https://github.com/biasvariancelabs/aitlas, 2026, accessed: Jul. 30, 2026.

[237] A. Lacoste, N. Lehmann, P. Rodriguez, E. Sherwin, H. Kerner, B. Lütjens, J. Irvin, D. Dao, H. Alemohammad, A. Drouin, M. Gunturkun, G. Huang, D. Vazquez, D. Newman, Y. Bengio, S. Ermon, and X. Zhu, "Geo-bench: Toward foundation models for earth monitoring," in *Adv. Neural Inf. Process. Syst.*, A. Oh, T. Naumann, A. Globerson, K. Saenko, M. Hardt, and S. Levine, Eds., vol. 36. Curran Associates, Inc., 2023, pp. 51 080–51 093. [Online]. Available: https://proceedings.neurips.cc/paper_files/paper/2023/file/a0644215d9cff6646fa334dfa5d29c5a-Paper-Datasets_and_Benchmarks.pdf

[238] C. Fibaek, L. Camilleri, A. Luyts, N. Dionelis, and B. Le Saux, "Phileo bench: Evaluating geo-spatial foundation models," in *Proc. IEEE Int. Geosci. Remote Sens. Symp. (IGARSS)*. IEEE, jul 2024, pp. 2739–2744. [Online]. Available: http://dx.doi.org/10.1109/igarss53475.2024.10642780

[239] N. I. Bountos, A. Ouaknine, I. Papoutsis, and D. Rolnick, "Fomo: Multi-modal, multi-scale and multi-task remote sensing foundation models for forest monitoring," *Proc. AAAI Conf. Artif. Intell.*, vol. 39, no. 27, pp. 27 858–27 868, Apr. 2025. [Online]. Available: http://dx.doi.org/10.1609/aaai.v39i27.35002

[240] P. Ghamisi, W. Yu, X. Zhang, A. Rizaldy, J. Wang, C. Zhou, R. Gloaguen, and G. Camps-Valls, "Geospatial foundation models to enable progress on sustainable development goals," 2025. [Online]. Available: https://arxiv.org/abs/2505.24528

[241] I. Corley, L. Sharma, and R. Crasto, "Landsat-bench: Datasets and benchmarks for landsat foundation models," in *ICML 2025 TerraBytes Workshop*, 2025. [Online]. Available: https://icml.cc/virtual/2025/47916

[242] X. Li, Y. Tao, S. Zhang, S. Liu, Z. Xiong, C. Luo, L. Liu, M. Pechenizkiy, X. Zhu, and T. Huang, "Reobench: Benchmarking robustness of earth observation foundation models," in *Adv. Neural Inf. Process. Syst.*, D. Belgrave, C. Zhang, H. Lin, R. Pascanu, P. Koniusz, M. Ghassemi, and N. Chen, Eds., vol. 38. Curran Associates, Inc., 2025. [Online]. Available: https://proceedings.neurips.cc/paper_files/paper/2025/file/58af38e2fba04b5e00c3450018c56406-Paper-Datasets_and_Benchmarks_Track.pdf

[243] O. Ronneberger, P. Fischer, and T. Brox, "U-net: Convolutional networks for biomedical image segmentation," in *Proc. Int. Conf. Med. Image Comput. Comput.-Assist. Intervent. (MICCAI)*. Cham: Springer International Publishing, 2015, pp. 234–241. [Online]. Available: http://dx.doi.org/10.1007/978-3-319-24574-4_28

[244] Z. Liu, H. Mao, C.-Y. Wu, C. Feichtenhofer, T. Darrell, and S. Xie, "A convnet for the 2020s," in *Proc. IEEE/CVF Conf. Comput. Vis. Pattern Recognit. (CVPR)*. IEEE, jun 2022, pp. 11 976–11 986. [Online]. Available: http://dx.doi.org/10.1109/cvpr52688.2022.01167

[245] T. Cover and P. Hart, "Nearest neighbor pattern classification," *IEEE Trans. Inf. Theory*, vol. 13, no. 1, pp. 21–27, Jan. 1967. [Online]. Available: http://dx.doi.org/10.1109/tit.1967.1053964

[246] L. Gilch, I. Wittmann, M. Nitsche, J. Jakubik, A. Ewald, and T. Brunschwiler, "How to embed matters: Evaluation of eo embedding design choices," in *Proc. IEEE/CVF Conf. Comput. Vis. Pattern Recognit. Workshops (CVPRW)*, Jun. 2026, pp. 7909–7918.

[247] Embed2Scale, "Embed2scale challenge," 2025 CVPR EarthVision Data Challenge, EvalAI, 2025. [Online]. Available: https://eval.ai/web/challenges/challenge-page/2465/overview

[248] D. Kerekes, I. Wittmann, E. Brune, R. Yadav, V. Marsocci, Y. Jia, and A. Nascetti, "Fused foundation model embeddings for earth observation compression: A winning solution to the Embed2Scale challenge," in *EurIPS Workshop Adv. Represent. Learn. Earth Observ.*, 2025. [Online]. Available: https://github.com/REO-workshop/2025-EurIPS-REO-workshop/blob/main/papers/Fused_Kerekes.pdf

[249] Z. Shang, S. Das, and A. Eldawy, "Benchmarking geospatial foundation models for agriculture applications," 2026. [Online]. Available: https://arxiv.org/abs/2606.29664

[250] L. McInnes, J. Healy, N. Saul, and L. Großberger, "Umap: Uniform manifold approximation and projection," *J. Open Source Softw.*, vol. 3, no. 29, p. 861, Sep. 2018. [Online]. Available: http://dx.doi.org/10.21105/joss.00861

[251] S. Kornblith, M. Norouzi, H. Lee, and G. Hinton, "Similarity of neural network representations revisited," in *Proc. Int. Conf. Mach. Learn. (ICML)*, ser. Proceedings of Machine Learning Research, K. Chaudhuri and R. Salakhutdinov, Eds., vol. 97. PMLR, 09–15 Jun 2019, pp. 3519–3529. [Online]. Available: https://proceedings.mlr.press/v97/kornblith19a.html

[252] D. Zanaga, R. Van De Kerchove, D. Daems, W. De Keersmaecker, C. Brockmann, G. Kirches, J. Wevers, O. Cartus, M. Santoro, S. Fritz, M. Lesiv, M. Herold, N.-E. Tsendbazar, P. Xu, F. Ramoino, and O. Arino, "Esa worldcover 10 m 2021 v200," 2022. [Online]. Available: https://zenodo.org/record/7254221

[253] W. Li, S. Liang, K. Chen, Y. Chen, H. Ma, J. Xu, Y. Ma, Y. Zhang, S. Guan, H. Fang, and Z. Shi, "Agrifm: A multi-source temporal remote sensing foundation model for agriculture mapping," *Remote Sens. Environ.*, vol. 334, p. 115234, Mar. 2026. [Online]. Available: http://dx.doi.org/10.1016/j.rse.2026.115234

[254] R. Daroya, E. Cole, O. Mac Aodha, G. Van Horn, and S. Maji, "Wildsat: Learning satellite image representations from wildlife observations," in *Proc. IEEE/CVF Int. Conf. Comput. Vis. (ICCV)*. IEEE, oct 2025, pp. 6143–6154. [Online]. Available: http://dx.doi.org/10.1109/iccv51701.2025.00580

[255] Esri, "Esri releases updated land-cover map with new sets of global data," https://www.esri.com/about/newsroom/announcements/esri-releases-updated-land-cover-map-with-new-sets-of-global-data, 2022, accessed: 2026-07-31.

[256] P. Gong, H. Liu, M. Zhang, C. Li, J. Wang, H. Huang, N. Clinton, J. Ji, W. Li, Y. Bai, B. Chen, B. Xu, Z. Zhu, C. Yuan, H. P. Suen, J. Guo, N. Xu, W. Li, Y. Zhao, J. Yang, C. Yu, X. Wang, H. Fu, L. Yu, I. Dronova, F. Hui, X. Cheng, X. Shi, F. Xiao, Q. Liu, and L. Song, "Stable classification with limited sample: transferring a 30-m resolution sample set collected in 2015 to mapping 10-m resolution global land cover in 2017," *Sci. Bull.*, vol. 64, no. 6, pp. 370–373, mar 2019. [Online]. Available: http://dx.doi.org/10.1016/j.scib.2019.03.002

[257] M. Santoro and O. Cartus, "Esa biomass climate change initiative (biomass_cci): Global datasets of forest above-ground biomass for the years 2010, 2015, 2016, 2017, 2018, 2019, 2020 and 2021, v5.01," 2024. [Online]. Available: https://catalogue.ceda.ac.uk/uuid/bf535053562141c6bb7ad831f5998d77

[258] N. Lang, W. Jetz, K. Schindler, and J. D. Wegner, "A high-resolution canopy height model of the earth," *Nat. Ecol. Evol.*, vol. 7, no. 11, pp. 1778–1789, Sep. 2023. [Online]. Available: http://dx.doi.org/10.1038/s41559-023-02206-6

[259] D. R. Cox, "The regression analysis of binary sequences," *J. R. Stat. Soc. Ser. B Stat. Methodol.*, vol. 20, no. 2, pp. 215–232, Jul. 1958. [Online]. Available: http://dx.doi.org/10.1111/j.2517-6161.1958.tb00292.x

[260] A. E. Hoerl and R. W. Kennard, "Ridge regression: Biased estimation for nonorthogonal problems," *Technometrics*, vol. 12, no. 1, pp. 55–67, Feb. 1970. [Online]. Available: http://dx.doi.org/10.1080/00401706.1970.10488634

[261] J. H. Friedman, "Greedy function approximation: A gradient boosting machine," *Ann. Stat.*, vol. 29, no. 5, pp. 1189–1232, oct 2001. [Online]. Available: http://dx.doi.org/10.1214/aos/1013203451

[262] T. Chen and C. Guestrin, "Xgboost: A scalable tree boosting system," in *Proc. 22nd ACM SIGKDD Int. Conf. Knowl. Discovery Data Mining (KDD)*, ser. KDD '16. ACM, Aug. 2016, pp. 785–794. [Online]. Available: http://dx.doi.org/10.1145/2939672.2939785

[263] G. Ke, Q. Meng, T. Finley, T. Wang, W. Chen, W. Ma, Q. Ye, and T.-Y. Liu, "LightGBM: A highly efficient gradient boosting decision tree," in *Adv. Neural Inf. Process. Syst.*, vol. 30, 2017.

[264] L. Prokhorenkova, G. Gusev, A. Vorobev, A. V. Dorogush, and A. Gulin, "CatBoost: unbiased boosting with categorical features," in *Adv. Neural Inf. Process. Syst.*, vol. 31, 2018.

[265] D. E. Rumelhart, G. E. Hinton, and R. J. Williams, "Learning representations by back-propagating errors," *Nature*, vol. 323, no. 6088, pp. 533–536, Oct. 1986. [Online]. Available: http://dx.doi.org/10.1038/323533a0

[266] Y. LeCun, L. Bottou, Y. Bengio, and P. Haffner, "Gradient-based learning applied to document recognition," *Proc. IEEE*, vol. 86, no. 11, pp. 2278–2324, 1998. [Online]. Available: http://dx.doi.org/10.1109/5.726791

[267] F. Pedregosa, G. Varoquaux, A. Gramfort, V. Michel, B. Thirion, O. Grisel, M. Blondel, P. Prettenhofer, R. Weiss, V. Dubourg, J. Vanderplas, A. Passos, D. Cournapeau, M. Brucher, M. Perrot, and Édouard Duchesnay, "Scikit-learn: Machine learning in python," *J. Mach. Learn. Res.*, vol. 12, no. 85, pp. 2825–2830, 2011. [Online]. Available: http://jmlr.org/papers/v12/pedregosa11a.html

[268] A. Paszke, S. Gross, F. Massa, A. Lerer, J. Bradbury, G. Chanan, T. Killeen, Z. Lin, N. Gimelshein, L. Antiga, A. Desmaison, A. Kopf, E. Yang, Z. DeVito, M. Raison, A. Tejani, S. Chilamkurthy, B. Steiner, L. Fang, J. Bai, and S. Chintala, "PyTorch: An imperative style, high-

performance deep learning library," in *Adv. Neural Inf. Process. Syst.*, vol. 32, 2019.

[269] D. A. Ross, J. Lim, R.-S. Lin, and M.-H. Yang, "Incremental learning for robust visual tracking," *Int. J. Comput. Vis.*, vol. 77, no. 1–3, pp. 125–141, May 2008. [Online]. Available: https://doi.org/10.1007/s11263-007-0075-7

[270] X. Gao, V. Pasquarella, D. Laflower, and J. R. Thompson, "Mapping forest communities, including species composition, structure, and carbon, at 10-m resolution using geospatial embeddings," 2025. [Online]. Available: http://dx.doi.org/10.2139/ssrn.5936862

[271] S. Cerna, S. Si-Moussi, I. Calderón-Sanou, V. Miele, and W. Thuiller, *Limits and promises of earth observation foundation models in predicting multi-trophic soil biodiversity*. Elsevier, 2026, pp. 31–64. [Online]. Available: https://doi.org/10.1016/bs.aecr.2026.02.005

[272] I. Zvonkov, G. Tseng, I. Becker-Reshef, and H. Kerner, "Cropland mapping using geospatial embeddings," in *ML4RS @ ICLR 2026 (Tutorial)*, 2026. [Online]. Available: https://openreview.net/forum?id=tqxUPNhQSI

[273] I. Strelnikov, V. Ostapko, and Y. Ibatulina, "Testing the applicability of foundational satellite data embedding models for remote identification of dominant species in herbaceous communities," 2025. [Online]. Available: https://zenodo.org/doi/10.5281/zenodo.17800714

[274] X. Li and L. Yu, "Mapping complex cropping patterns in china (2018–2021) at 10 m resolution: a data-driven framework based on multi-product integration and google satellite embedding," *Earth Syst. Sci. Data*, vol. 18, no. 7, pp. 5601–5626, 2026. [Online]. Available: https://doi.org/10.5194/essd-18-5601-2026

[275] M. Mura, M. Mura, N. Puletti, and R. Scotti, "Operational deployment of satellite embeddings for forestry: An evaluation," 2026. [Online]. Available: http://dx.doi.org/10.2139/ssrn.6362220

[276] T. Maffei, M. Moretto, and P. Franceschi, "Exploring tessera earth embeddings latent space: a regional unsupervised openstreetmap's landuse classification and topographic characterization," 2026. [Online]. Available: http://dx.doi.org/10.2139/ssrn.6578542

[277] G. Díaz-Ireland, D. Gülçin, A. López-Sánchez, M. García Peces, D. Prieto-Herráez, and J. Velázquez, "Comparative evaluation of alphaearth annual embeddings vs. seasonal remote sensing layers with u-net segmentation for california crop and land-use mapping," 2026. [Online]. Available: http://dx.doi.org/10.2139/ssrn.6667132

[278] A. I. Chowdhury, M. Ahishali, M. Vastaranta, M. J. Uddin, and S. Junttila, "Satellite embeddings as complementary predictors of standing dead-tree volume fraction in boreal forests," 2026. [Online]. Available: http://dx.doi.org/10.2139/ssrn.6922442

[279] C. Jin, X. Jiang, L. Wen, C. Wu, X. Xu, and J. Jiao, "Assessing the utility of satellite embedding features for biomass prediction in subtropical forests with machine learning," *Remote Sens.*, vol. 18, no. 3, p. 436, Jan. 2026. [Online]. Available: http://dx.doi.org/10.3390/rs18030436

[280] J. G. Ball, J. A. Wicklein, Z. Feng, J. Knezevic, S. Jaffer, A. Madhavapeddy, C. Atzberger, M. Dalponte, and D. A. Coomes, "Geospatial foundation models enable data-efficient tree species mapping in temperate mountain forests," *Sci. Remote Sens.*, vol. 14, p. 100466, Dec. 2026. [Online]. Available: http://dx.doi.org/10.1016/j.srs.2026.100466

[281] D. Paluba, V. Marsocci, K. Onačillová, Y. T. Puerta Quintana, and A. Hastie, "Gem-forest: A global satellite embedding–based map of forests and tree crops for 2020," Mar. 2026. [Online]. Available: http://dx.doi.org/10.5194/egusphere-2026-1401-v1

[282] H. Sohrabi, "Integrating satellite embeddings and national forest inventory data to map above-ground biomass of temperate deciduous old-growth forests," *Adv. Space Res.*, vol. 77, no. 12, pp. 11 837–11 850, Jun. 2026. [Online]. Available: http://dx.doi.org/10.1016/j.asr.2026.04.018

[283] A. Heiman, "Characterizing brazilian atlantic forest restoration outcomes with geospatial alphaearth embeddings," 2026. [Online]. Available: https://arxiv.org/abs/2605.05547

[284] M. Narimani, A. Pourreza, and P. Farajpoor, "Mapping tomato cropping systems in california using alphaearth geospatial embeddings and deep learning analysis," 2026. [Online]. Available: https://arxiv.org/abs/2605.21804

[285] J. Esteban Cava, J. A. Navarro, J. L. Tomé Morán, and I. González González, "Aplicaciones de google satellite embeddings en la cartografía de plantaciones forestales en uganda," *Congr. UEx, Actas Congr.*, vol. 2, no. 2, pp. 1–5, jun 2026. [Online]. Available: http://dx.doi.org/10.17398/3101-7177.2.201

[286] M. S. Watt, A. Holdaway, J. S. Marchant, M. Mohan, P. Watt, and M. Baboolall, "National-scale forest aboveground biomass mapping in guyana using stability-based feature selection and geospatial embeddings," *Forests*, vol. 17, no. 6, p. 725, Jun. 2026. [Online]. Available: http://dx.doi.org/10.3390/f17060725

[287] Y. Sun, Z. Xue, H. Wu, and X. Nie, "The first map of planted mangrove forests in china derived from time-series landsat and google satellite embeddings," *Remote Sens. Environ.*, vol. 344, p. 115541, Oct. 2026. [Online]. Available: http://dx.doi.org/10.1016/j.rse.2026.115541

[288] K. Jing, M. Zhang, B. Wu, Y. Xie, M. Li, H. Ma, and Y. Li, "Distilling geospatial foundation model semantics into interpretable sentinel-1/2 proxies for few-shot and cross-year crop type classification," *Big Earth Data*, pp. 1–30, Jul. 2026. [Online]. Available: http://dx.doi.org/10.1080/20964471.2026.2691477

[289] W. Qi, L. Yu, T. Liu, Y. Wang, X. Zhou, Y. Zhang, X. Li, Q. Zhao, H. Wu, S. Zheng, Y. Zeng, and M. Xu, "Integrating hyperspectral data and google satellite embedding features for aquatic fish biodiversity prediction," *J. Remote Sens.*, vol. 6, p. 1069, jan 2026. [Online]. Available: http://dx.doi.org/10.34133/remotesensing.1069

[290] W. Liu, Q. Shu, H. Zhang, B. Zhang, T. He, X. Wen, Y. Wang, R. Wei, X. Rao, and J. Liu, "Satellite embedding features for grassland aboveground biomass estimation in complex mountainous terrain: A case study of the three parallel rivers region, china," *Remote Sens.*, vol. 18, no. 14, p. 2348, Jul. 2026. [Online]. Available: http://dx.doi.org/10.3390/rs18142348

[291] C. Mahlasi, G. S. Baloyi, Z. Gaffoor, L. Klein, A. Jones, E. Vos, M. Muszynski, G. Dawson, and C. Watson, "Ecological mapping with geospatial foundation models," 2026. [Online]. Available: https://arxiv.org/abs/2602.10720

[292] W. Wang, H. Guo, S. He, F. Qi, A. Samat, D. Wang, and J. Li, "Ai-driven precision mapping of tea plantations using alphaearth foundations: A scalable solution for smart agricultural monitoring," *Agriculture*, vol. 16, no. 4, p. 412, Feb. 2026. [Online]. Available: http://dx.doi.org/10.3390/agriculture16040412

[293] Y.-C. Chang, A. J. Stewart, F. Bastani, P. Wolters, S. Kannan, G. R. Huber, J. Wang, and A. Banerjee, "On the generalizability of foundation models for crop type mapping," in *Proc. IEEE Int. Geosci. Remote Sens. Symp. (IGARSS)*. IEEE, Aug. 2025, pp. 948–953. [Online]. Available: http://dx.doi.org/10.1109/igarss55030.2025.11242260

[294] C. Butsko, G. Tseng, K. Van Tricht, G. Milli, D. Rolnick, R. Cartuyvels, I. Becker-Reshef, Z. Szantoi, and H. Kerner, "Deploying geospatial foundation models in the real world: Lessons from worldcereal," in *Proc. TerraBytes ICML Workshop: Towards Global Datasets and Models for Earth Observation*, ser. Proceedings of Machine Learning Research, N. Audebert, H. Azizpour, V. Barrière, J. Castillo Navarro, M. Czerkawski, H. Fang, A. Francis, V. Marsocci, A. Nascetti, and R. Yadav, Eds., vol. 292. PMLR, 19 Jul 2025, pp. 13–31. [Online]. Available: https://proceedings.mlr.press/v292/butsko25a.html

[295] M. K. Pasupuleti, "Ai climate risk in arcgis: Foundation-model remote sensing and spatio-temporal causality," *Int. J. Acad. Ind. Res. Innov. (IJAIRI)*, vol. 03, no. 12, pp. 114–126, Dec. 2023. [Online]. Available: http://dx.doi.org/10.62311/nesx/rp-301223-114-126

[296] C. I. Alvarez, C. A. Ulloa Vaca, and N. A. Echeverria Llumipanta, "Machine learning for urban air quality prediction using google alphaearth foundations satellite embeddings: A case study of quito, ecuador," *Remote Sens.*, vol. 17, no. 20, p. 3472, Oct. 2025. [Online]. Available: http://dx.doi.org/10.3390/rs17203472

[297] J. A. Leonardi, V. Marsocci, V. Yordanov, and M. A. Brovelli, "Integration of geospatial foundation models in unsupervised change detection workflows for landslide identification," *Int. J. Digit. Earth*, vol. 18, no. 1, p. 2547292, aug 2025. [Online]. Available: http://dx.doi.org/10.1080/17538947.2025.2547292

[298] Y. Wei, R. Zhong, and Y. Yang, "Groundwater fluoride prediction for sustainable water management: A comparative evaluation of machine learning approaches enhanced by satellite embeddings," *Sustainability*, vol. 17, no. 18, p. 8505, Sep. 2025. [Online]. Available: http://dx.doi.org/10.3390/su17188505

[299] M. M. T. Alam and A. Simic Milas, "Dimensionality optimized machine learning retrieval of canopy chlorophyll, nitrogen, and phosphorus from google satellite embeddings," *Smart Agric. Technol.*, vol. 12, p. 101601, Dec. 2025. [Online]. Available: http://dx.doi.org/10.1016/j.atech.2025.101601

[300] H. Yang, J. Xia, and J. Zhang, "Deep feature fusion of alphaearth foundations satellite embeddings and sentinel-2 imagery for urban water mapping: A case study of lingang special area," *IEEE Access*, vol. 14, pp. 73 082–73 095, 2026. [Online]. Available: http://dx.doi.org/10.1109/access.2026.3691743

[301] Mingxuan Li, Wenkai Li, Hongliang Liu, and Changshan Liang, "Leveraging geospatial foundation model embeddings for local-scale

landslide susceptibility mapping via positive-unlabeled learning," 2026. [Online]. Available: https://www.researchgate.net/doi/10.13140/RG.2.2.18370.34244

[302] A. Berg and S. Leyk, "Spatial scale effects in foundation model earth embeddings: A case study on predicting the exposure of structures to wildfire in colorado, usa," 2026. [Online]. Available: http://dx.doi.org/10.2139/ssrn.7026253

[303] P. Qu, W. Ouyang, C. Zhang, Y. Chai, S. Xu, L. Ye, Y. Piao, M. Zhang, and H. Lu, "Utilizing earth foundation models to enhance the simulation performance of hydrological models with alphaearth embeddings," 2026. [Online]. Available: https://arxiv.org/abs/2601.01558

[304] Y. Cheng, Q. Zhu, and L. Fan, "From landslide conditioning factors to satellite embeddings: Evaluating the utilisation of google alphaearth for landslide susceptibility mapping using deep learning," 2026. [Online]. Available: https://arxiv.org/abs/2601.07268

[305] Y. Yang, J. Wang, P. Wu, Y. Liu, and X. Zhao, "Combining large language models with satellite embedding to comprehensively evaluate the tibetan plateau's ecological quality," *Remote Sens.*, vol. 18, no. 4, p. 643, Feb. 2026. [Online]. Available: http://dx.doi.org/10.3390/rs18040643

[306] A. Hamoudzadeh, V. Belloni, and R. Ravanelli, "Inferring height from earth embeddings: First insights using google alphaearth," 2026. [Online]. Available: https://arxiv.org/abs/2602.17250

[307] Z. Ou and Y. Zheng, "Foundation-scale satellite embeddings reframe hydrological generalization as a representation problem," *Geophys. Res. Lett.*, vol. 53, no. 7, p. e2025GL121604, apr 2026. [Online]. Available: http://dx.doi.org/10.1029/2025gl121604

[308] V. Khajuria, S. Singh, L. Paro, M. Spagnolo, and A. Ribolini, "Rock glacier detection using satellite embeddings and machine learning on google earth engine," *Earth Syst. Environ.*, pp. 1–23, apr 2026. [Online]. Available: http://dx.doi.org/10.1007/s41748-026-01139-x

[309] U. Nazir, I.-H. Cheng, and S. Khalid, "Alphaearth satellite embeddings for modelling climate sensitive diseases towards global health resilience," 2026. [Online]. Available: https://arxiv.org/abs/2605.10949

[310] H. Lin, P. Lin, F. Zhang, L. Slater, Y. Yang, M. Pan, Q. Qin, and A. Hou, "Fusing satellite embeddings to improve streamflow reconstruction across river networks," Apr. 2026. [Online]. Available: http://dx.doi.org/10.5194/egusphere-2026-1834

[311] W. Liu, S. Li, C. Shi, H. Zhu, C. Huang, and L. Yin, "Landslide mapping and susceptibility assessment in the middle and lower reaches of the nujiang river (2017–2025) using satellite embedding and multidimensional environmental factors," *Remote Sens.*, vol. 18, no. 11, p. 1854, Jun. 2026. [Online]. Available: http://dx.doi.org/10.3390/rs18111854

[312] T. Mahato, S. Sarkar, B. R. Parida, and S. Bar, "Beyond multispectral limits: Satellite embeddings for fire severity estimation across global biomes," Jun. 2026. [Online]. Available: http://dx.doi.org/10.21203/rs.3.rs-9849270/v1

[313] H. B. Vu, "Clay-cnn hybrids: Leveraging geospatial foundation models as auxiliary context for landslide detection," 2026. [Online]. Available: https://arxiv.org/abs/2606.14081

[314] J. Koch, T. Denager, S. Stisen, M. H. Greve, A. B. Møller, and A. M. Beucher, "Modelling carbon and groundwater in peatlands using alphaearth embeddings," Feb. 2026. [Online]. Available: http://dx.doi.org/10.22541/essoar.177135853.32181864/v1

[315] Z. Zhou, M. M. Rahman Siddiquee, N. Tajbakhsh, and J. Liang, "Unet++: A nested u-net architecture for medical image segmentation," in *Proc. Deep Learn. Med. Image Anal. Multimodal Learn. Clin. Decis. Support*. Cham: Springer International Publishing, 2018, pp. 3–11. [Online]. Available: http://dx.doi.org/10.1007/978-3-030-00889-5_1

[316] Y. Zheng, W. Wu, B. Wu, G. Li, M. Czerkawski, and K. Klemmer, "Sentinel-2 image retrieval with global, cross-modal embeddings," in *EGU General Assembly 2026*, 2026. [Online]. Available: https://meetingorganizer.copernicus.org/EGU26/EGU26-11672.html

[317] M. Rahman, "Physically interpretable alphaearth foundation model embeddings enable llm-based land surface intelligence," *Remote Sens. Appl.: Soc. Environ.*, vol. 42, p. 102045, Apr. 2026. [Online]. Available: http://dx.doi.org/10.1016/j.rsase.2026.102045

[318] X. Zhang, Y. Yang, Z. Ye, B. Baiyun, X. Guo, Q. Fang, R. Zhang, X. Zhou, and H. Wang, "Fusar-gpt: A spatiotemporal feature-embedded and two-stage decoupled visual language model for sar imagery," in *Proc. IEEE/CVF Conf. Comput. Vis. Pattern Recognit. (CVPR)*, Jun. 2026, pp. 42 158–42 168.

[319] M. B. Pettersson and A. Daoud, "Leveraging compact satellite embeddings and graph neural networks for large-scale poverty mapping," 2025. [Online]. Available: https://arxiv.org/abs/2511.01408

[320] J. Jiang, W. Zhao, C. Yan, G. Y. Qiu, W. Yan, K. Li, D. Mo, B. Zhu, and Y. Xiong, "Transformer-based mapping of 10 m spatiotemporally seamless daily urban evapotranspiration using geospatial foundation embeddings," 2026. [Online]. Available: http://dx.doi.org/10.2139/ssrn.6539464

[321] X. Yue, Z. Zhao, and K. Hu, "Estimating economic activity from satellite embeddings," *Appl. Sci.*, vol. 16, no. 2, p. 582, Jan. 2026. [Online]. Available: http://dx.doi.org/10.3390/app16020582

[322] W. Gong, U. Srivastava, Y. Wang, Y. Jia, Q. Wu, W. Bai, Y. Yang, X. Huang, and X. Ye, "Earth embeddings reveal diverse urban signals from space," 2026. [Online]. Available: https://arxiv.org/abs/2604.03456

[323] Y. Zhang, Q. Qin, H. Nie, M.-P. Kwan, S. He, and E. Ke, "Cross-city traffic noise modeling and inequality analysis via alphaearth geospatial foundation models," *Transp. Res. Part D Transp. Environ.*, vol. 156, p. 105378, Jul. 2026. [Online]. Available: http://dx.doi.org/10.1016/j.trd.2026.105378

[324] S. Hou, Z. Liu, H. Jiao, L. Xie, Y. Qing, X. Zhang, Q. Xu, Z. Xu, X. Guan, and H. Wu, "Aef-econ: Toward plug-and-play socioeconomic foundation embeddings from alphaearth for urban remote sensing," 2026. [Online]. Available: https://arxiv.org/abs/2606.20697

[325] L. Sherman, J. Proctor, H. Druckenmiller, H. Tapia, and S. Hsiang, "Global high-resolution estimates of the un human development index using satellite imagery and machine learning," *Nat. Commun.*, vol. 17, no. 1, p. 1315, feb 2026. [Online]. Available: http://dx.doi.org/10.1038/s41467-026-68805-6

[326] H. Herzog, F. Bastani, Y. Zhang, G. Tseng, J. Redmon, H. Sablon, R. Park, J. Morrison, A. Buraczynski, K. Farley, J. Hansen, A. Howe, P. A. Johnson, M. Otterlee, T. Schmitt, H. Pitelka, S. Daspit, R. Ratner, C. Wilhelm, S. Wood, M. Jacobi, H. Kerner, E. Shelhamer, A. Farhadi, R. Krishna, and P. Beukema, "Olmoearth: Stable latent image modeling for multimodal earth observation," in *Proc. IEEE/CVF Conf. Comput. Vis. Pattern Recognit. (CVPR)*, Jun. 2026, pp. 34 806–34 817.

[327] L. Di, D. J. Meyer, and E. Yu, "OGC Testbed 19 Analysis Ready Data Engineering Report," Open Geospatial Consortium, OGC Engineering Report OGC 23-043, July 2024. [Online]. Available: https://doi.org/10.62973/23-043

[328] S. Khanna, P. Liu, L. Zhou, C. Meng, R. Rombach, M. Burke, D. Lobell, and S. Ermon, "DiffusionSat: A generative foundation model for satellite imagery," in *Proc. Int. Conf. Learn. Represent. (ICLR)*, 2024. [Online]. Available: https://openreview.net/forum?id=I5webNFDgQ

[329] P. H. Schönemann, "A generalized solution of the orthogonal procrustes problem," *Psychometrika*, vol. 31, no. 1, pp. 1–10, mar 1966. [Online]. Available: http://dx.doi.org/10.1007/bf02289451

[330] Y. Shen, Y. Xiong, W. Xia, and S. Soatto, "Towards backward-compatible representation learning," in *Proc. IEEE/CVF Conf. Comput. Vis. Pattern Recognit. (CVPR)*. IEEE, jun 2020, pp. 6368–6377. [Online]. Available: http://dx.doi.org/10.1109/cvpr42600.2020.00640

[331] I. Higgins, L. Matthey, A. Pal, C. Burgess, X. Glorot, M. Botvinick, S. Mohamed, and A. Lerchner, "beta-VAE: Learning basic visual concepts with a constrained variational framework," in *Proc. Int. Conf. Learn. Represent. (ICLR)*, 2017. [Online]. Available: https://openreview.net/forum?id=Sy2fzU9gl

[332] F. Locatello, S. Bauer, M. Lucic, G. Raetsch, S. Gelly, B. Schölkopf, and O. Bachem, "Challenging common assumptions in the unsupervised learning of disentangled representations," in *Proc. Int. Conf. Mach. Learn. (ICML)*, ser. Proceedings of Machine Learning Research, K. Chaudhuri and R. Salakhutdinov, Eds., vol. 97. PMLR, 09–15 Jun 2019, pp. 4114–4124. [Online]. Available: https://proceedings.mlr.press/v97/locatello19a.html

[333] M. Raissi, P. Perdikaris, and G. Karniadakis, "Physics-informed neural networks: A deep learning framework for solving forward and inverse problems involving nonlinear partial differential equations," *J. Comput. Phys.*, vol. 378, pp. 686–707, Feb. 2019. [Online]. Available: http://dx.doi.org/10.1016/j.jcp.2018.10.045

[334] Y. Sun, Y. Ming, X. Zhu, and Y. Li, "Out-of-distribution detection with deep nearest neighbors," in *Proc. Int. Conf. Mach. Learn. (ICML)*, ser. Proceedings of Machine Learning Research, K. Chaudhuri, S. Jegelka, L. Song, C. Szepesvari, G. Niu, and S. Sabato, Eds., vol. 162. PMLR, 17–23 Jul 2022, pp. 20 827–20 840. [Online]. Available: https://proceedings.mlr.press/v162/sun22d.html

[335] K. Doerksen and H. Kerner, "Earthshift: a benchmark for measuring robustness to real-world distribution shifts in earth observation," 2026. [Online]. Available: https://arxiv.org/abs/2605.29330

[336] A. Kaur, M. Purohit, G. Muhawenayo, E. Rolf, and H. Kerner, "Pretrain where? investigating how pretraining data diversity impacts geospatial

foundation model performance," in *Proc. IEEE/CVF Conf. Comput. Vis. Pattern Recognit. Workshops (CVPRW)*, Jun. 2026, pp. 7949–7959.

[337] L. Gordon, S. Belongie, C. Igel, and N. Lang, "Mmearth-bench: Global model adaptation via multimodal test-time training," in *Proc. Eur. Conf. Comput. Vis. (ECCV)*, 2026. [Online]. Available: https://arxiv.org/abs/2602.06285

[338] E. Rolf, K. Klemmer, C. Robinson, and H. Kerner, "Position: Mission critical—satellite data is a distinct modality in machine learning," in *Proc. Int. Conf. Mach. Learn. (ICML)*, ser. Proceedings of Machine Learning Research, R. Salakhutdinov, Z. Kolter, K. Heller, A. Weller, N. Oliver, J. Scarlett, and F. Berkenkamp, Eds., vol. 235. PMLR, 21–27 July 2024, pp. 42 691–42 706. [Online]. Available: https://proceedings.mlr.press/v235/rolf24a.html